

Investigation of Properties of a New Liquid Ionization Chamber for Radiation Dosimetry

Adam S. Elliott
Department of Medical Physics
McGill University, Montreal
August 2006

A thesis submitted to McGill University in partial fulfilment of the requirements of the
degree of Master of Science in Medical Physics

© Adam S. Elliott 2006



Library and
Archives Canada

Bibliothèque et
Archives Canada

Published Heritage
Branch

Direction du
Patrimoine de l'édition

395 Wellington Street
Ottawa ON K1A 0N4
Canada

395, rue Wellington
Ottawa ON K1A 0N4
Canada

Your file *Votre référence*
ISBN: 978-0-494-32699-2
Our file *Notre référence*
ISBN: 978-0-494-32699-2

NOTICE:

The author has granted a non-exclusive license allowing Library and Archives Canada to reproduce, publish, archive, preserve, conserve, communicate to the public by telecommunication or on the Internet, loan, distribute and sell theses worldwide, for commercial or non-commercial purposes, in microform, paper, electronic and/or any other formats.

The author retains copyright ownership and moral rights in this thesis. Neither the thesis nor substantial extracts from it may be printed or otherwise reproduced without the author's permission.

AVIS:

L'auteur a accordé une licence non exclusive permettant à la Bibliothèque et Archives Canada de reproduire, publier, archiver, sauvegarder, conserver, transmettre au public par télécommunication ou par l'Internet, prêter, distribuer et vendre des thèses partout dans le monde, à des fins commerciales ou autres, sur support microforme, papier, électronique et/ou autres formats.

L'auteur conserve la propriété du droit d'auteur et des droits moraux qui protègent cette thèse. Ni la thèse ni des extraits substantiels de celle-ci ne doivent être imprimés ou autrement reproduits sans son autorisation.

In compliance with the Canadian Privacy Act some supporting forms may have been removed from this thesis.

Conformément à la loi canadienne sur la protection de la vie privée, quelques formulaires secondaires ont été enlevés de cette thèse.

While these forms may be included in the document page count, their removal does not represent any loss of content from the thesis.

Bien que ces formulaires aient inclus dans la pagination, il n'y aura aucun contenu manquant.


Canada

*This thesis is dedicated to my wife and eternal companion, Breian, and to
my two children, Addison and Ian.*

Abstract

Liquid ionization chambers have characteristics that can remedy some of the drawbacks of air-filled ionization chamber dosimetry: large sensitive volumes, fluence perturbations, and energy dependence. However, high ion recombination rates can be a significant problem in liquid chambers. In this work, we have investigated properties of a new liquid chamber, called the GLIC-03 (Guarded Liquid Ionization Chamber), including chamber stability, reproducibility, and establishing recombination corrections. The response varied by less than 1% over 10 hours, and was reproducible within 1.5% of the mean over different liquid fills. Recombination corrections were established, and were small for low dose rates and high voltages. The establishment of these characteristics allowed us to compare measurements of the GLIC-03 in a region of charged particle disequilibrium to those made with a diamond detector. Results show the GLIC-03's suitability as a high resolution detector.

Résumé

Les chambres d'ionisation liquides ont des caractéristiques qui peuvent remédier à certains des inconvénients de dosimétrie de chambre d'ionisation remplies d'air: les grands volumes, la perturbation de la fluence, et la dépendance à l'énergie. Cependant, les hauts taux de recombinaison d'ions peuvent être un problème significatif dans les chambres liquides. Dans cette étude, nous avons examiné certaines propriétés d'une nouvelle chambre liquide: la stabilité de la chambre, la reproductibilité, et la recombinaison. Le signal mesuré variait par moins de 1% sur 10 heures et était reproductible dans les 1.5% de la moyenne. Les corrections de recombinaison ont été établies, et étaient petites pour les faibles débits de dose et les hautes tensions. L'établissement de ces caractéristiques nous a permis de comparer les mesures du GLIC-03 dans une région de déséquilibre de particules chargées à celles faites avec un détecteur à diamant. Les résultats démontrent que cette chambre peut être utilisée comme détecteur à haute résolution.

Acknowledgements

I would first like to thank my supervisor, Dr. Jan Seuntjens, for offering this project and for his constant support and guidance.

This thesis would also not have been possible without the help of Kristin Stewart, who designed the liquid ionization chambers and began the project, and who has a continuing interest in its success. I would also like to thank the following individuals for their contributions: Michael Evans and Dr. Wamied Abdel-Rahman for consultation on various topics; Robin Van Gils for building the liquid chamber and many other important pieces of equipment used in this research; and engineers Pierre Leger, Vlad Bobes, and especially Joe Larkin for electrical engineering help, and consultation concerning the linear accelerator. I also offer many thanks to Dr. Stanislav Vatnitsky for loaning us the diamond detector for comparison measurements.

I must acknowledge my appreciation for the encouragement and friendship I have received from all my fellow graduate students in the Medical Physics Unit, particularly from Kristin Stewart, Edwin Sham, and my fellow M.Sc. students Andrew Alexander, Krum Asiev, Marie-Joelle Bertrand, Luke Fu, Rong Ding Li, Arman Sarfehnia, and Joonyoung Suk. Marie-Joelle also offered corrections to the French translation of the abstract. I would also like to thank the custodians Joseph and Hermy in the MPU for their friendship.

Funding for the research presented in this thesis has been provided through NSERC grant RGPIN #298191.

Of course, this thesis would not have occurred were it not for the excellent medical physics graduate program established under Dr. Ervin B. Podgorsak at McGill University. My understanding and admiration of this profession grew particularly in his classes and in his interviews. His secretary, Margery Knewstubb, has also been invaluable in her willingness to help with anything.

Although this thesis is dedicated to my family, I would like to acknowledge them here as well. My wife, Breian, has offered unconditional support in my education and this research. Breian, along with my two wonderful children, Addison and Ian, have made everything worthwhile.

Table of Contents

Abstract	i
Résumé	ii
Acknowledgements	iii
Table of Contents	iv
List of Tables	vi
List of Figures	vii
Chapter 1	1
Introduction	1
1.1 Treatment of Cancer	1
1.2 Radiation Therapy	1
1.3 Cell Damage and Ionizing Radiation	2
1.4 Dosimetry	3
1.5 Motivation	4
References	5
Chapter 2	7
Radiation Interactions and Dosimetry	7
2.1 Introduction	7
2.2 Interactions of Ionizing Radiation with Matter	7
2.2.1 Photon Radiation and Its Interactions	7
2.2.2 Electron Radiation and Its Interactions	15
2.3 Dosimetric Quantities	20
2.3.1 Particle Fluence	20
2.3.2 Energy Fluence	21
2.3.3 Kerma	22
2.3.4 Exposure	23
2.3.5 Charged Particle Equilibrium	24
2.4 Cavity Theory	25
2.4.1 Bragg-Gray Cavity Theory	26
2.4.2 Spencer-Attix Cavity Theory	27
2.5 Air-kerma-in-air-based Protocols	29
2.6 Absorbed-dose-to-water-based Protocols	31
2.6.1 Beam Quality Conversion Factor	32
2.6.2 Beam Quality Specification	33
2.6.3 Calibration of Photon Beams	36
2.6.4 Calibration of Electron Beams	37
2.7 Complexities of Non-equilibrium Dosimetry	39
2.7.1 Build-up Region	40
References	45
Chapter 3	47
Standard Air Ionization Chambers	47
3.1 Introduction	47
3.2 Correction Factors for Air Chambers	49
3.2.1 Temperature, Pressure, and Humidity Effects	49
3.2.2 Polarity Effects	50
3.2.3 Recombination Effects	51
3.2.4 Chamber Leakage Effects	57
3.3 Limitations of Standard Chambers	57
3.3.1 Low Spatial Resolution	57
3.3.2 Chamber Fluence Perturbation	58
3.3.3 Energy Dependence	59
References	60

Chapter 4	62
Liquid Ionization Chambers and Their History	62
4.1 Advantages of Liquid Ionization Chambers	62
4.1.1 Insulation	62
4.1.2 Free-ion Yield	63
4.1.3 Density and Atomic Number	64
4.1.4 Stopping Power Ratios	65
4.1.5 Ionization Density and Mobility	66
4.2 Modern Research in Liquid Ionization Chambers	67
4.3 Research in Liquid Ionization Chambers at McGill University	69
References	72
Chapter 5	75
The GLIC-03: Construction, Stability, Reproducibility, and Recombination	75
5.1 Construction	75
5.1.1 Sensitive Volume and Plate Separation	76
5.2 Methods and Materials, and Results	82
5.2.1 GLIC-03 Inherent Leakage	83
5.2.2 Stability of Response	84
5.2.3 Reproducibility	88
5.2.4 Minimizing Recombination due to Pulse Overlap	90
5.2.5 Recombination Corrections	91
References	100
Chapter 6	102
Measurements of the Photon Build-up Region	102
6.1 Introduction	102
6.2 Methods and Materials	102
6.3 Results and Discussion	104
References	106
Chapter 7	107
Conclusions and Future Work	107
7.1 Conclusions	107
7.2 Future Work	108
Bibliography	109

List of Tables

Table 1-1.	Guidelines for electron beam calibration for absorbed-dose-to-water-based protocols AAPM TG-51 and IAEA TRS-398	37
Table 4-1.	Mass densities and effective atomic number of air, water, and the two dielectric liquids isooctane and tetramethylsilane (TMS).....	64
Table 4-2.	Mobility of both positive and negative ions produced in air, isooctane and TMS	67
Table 5-1.	Calibration coefficient, nominal volume, and beam quality conversion factors of Exradin A12 air ionization chamber used in this thesis. Calculated calibration coefficients and volume of air-filled GLIC-03	79
Table 5-2.	Summarized table of determined properties of GLIC-03	81

List of Figures

Figure 2-1.	Maximum and mean fractions of incident photon energy transferred to scattered electron in the Compton effect.....	13
Figure 2-2.	Relative predominance of photoelectric effect, Compton effect, and pair production for elements with atomic numbers 1-100 and over a large photon energy range.....	15
Figure 2-3.	Electron-atom interaction, with the impact parameter b and atomic radius a	16
Figure 2-4.	Role of angle of incidence in particle fluence and planar fluence.....	21
Figure 2-5.	Percent depth dose curve for a typical electron beam in water	35
Figure 2-6.	Source-to- surface distance (SSD) and source-to-axis distance (SAD) setups used for photon beam dosimetry	36
Figure 2-7.	Graph of collisional kerma and absorbed dose as a function of depth in a phantom irradiated with a high-energy photon beam, where photon beam is not attenuated or scattered	40
Figure 2-8.	Graph of collisional kerma and absorbed dose as a function of depth in a phantom irradiated with a high-energy photon beam, where photon beam is attenuated and scattered.....	41
Figure 2-9.	Geometric penumbra due to finite size of focal spot.....	43
Figure 2-10.	Lateral charged particle disequilibrium.....	44
Figure 3-1.	Schematic diagram of the inner circuitry for a parallel-plate ionization chamber	48
Figure 3-2.	Schematic diagram of the inner circuitry for a cylindrical ionization chamber	48
Figure 3-3.	Air ionization chamber saturation curve	52
Figure 3-4.	Effects of in-scattering on electron distribution in a chamber cavity	59
Figure 3-5.	Ratio of restricted mass stopping power water-to-air as a function of electron kinetic energy. The ratio is not constant over the clinical range of electron energies, thus air chambers are energy dependent	60
Figure 4-1.	Chemical structure of Isooctane and tetramethylsilane molecules.....	63
Figure 4-2.	Ratio of restricted stopping powers (water-air, water-isooctane, and water-TMS) as a function of electron kinetic energy. ⁵ Note the relative lack of energy dependence for the dielectric liquids ratios compared to the air ratio	66
Figure 4-3.	Beam quality conversion factors for the LIC and for the Exradin A12.....	70
Figure 4-4.	Schematic diagram of the modified Exradin A14P microchamber, called the micro-LIC when filled with isooctane.....	71
Figure 5-1.	Photograph of inner details of the GLIC-03 with cap unscrewed. Visible are the collecting electrode, guard electrode, brass foil, and filling tube ends	75
Figure 5-2.	Schematic diagram of the GLIC-03	76

Figure 5-3.	Charge collected by air-filled GLIC-03 after increments of 50 V up to 400 V for three separate trials (all overlap each other). The capacitance is determined in each trial by the slope of a line fit to the measured points.....	80
Figure 5-4.	Setup for stability, reproducibility, and recombination experiments involving the GLIC-03. The Exradin A12 air chamber sensitive volume is located within the radiation field in order to monitor linac output changes	82
Figure 5-5.	Inherent leakage current of the GLIC-03 over time while a polarizing voltage of 500 V is applied across the sensitive volume. 5 different trials are shown.....	84
Figure 5-6.	GLIC-03 and Solid Water™ phantom setup	85
Figure 5-7.	GLIC-03 response comparing two different fills and two different setup orientations of the same fill.....	86
Figure 5-8.	Changing response of the GLIC-03.....	87
Figure 5-9.	Response of the GLIC-03 over three trials of 5, 7, and 24 hours.....	88
Figure 5-10.	Response of GLIC-03 after each new fill.....	89
Figure 5-11.	Response of GLIC-03 normalized to dose setting as a function of dose rate setting, for two different electron beam energies	91
Figure 5-12.	Typical liquid ionization chamber ionization curve	93
Figure 5-13.	GLIC-03 ionization curve for various dose per pulse values	91
Figure 5-14.	Extrapolation of one ionization curve of GLIC-03	91
Figure 5-15.	Theoretical general collection efficiency of the GLIC-03 for various doses per pulse, as a function of electric field strength	91
Figure 5-16.	GLIC-03 response in an 18 MV beam as a function of dose per pulse in the phantom, for various voltages across the chamber sensitive volume	100
Figure 6-1.	Schematic diagram of the entire diamond detector and the detecting unit.....	104
Figure 6-2.	Build-up region measurements of GLIC-03 (air- and liquid-filled) and diamond detector	105
Figure 6-3.	Comparison of PDI curve of the liquid-filled GLIC-03 with those of the diamond detector and the air-filled GLIC-03.....	106

Chapter 1

Introduction

1.1 Treatment of Cancer

This year, approximately 153,100 new cases of cancer will be diagnosed in Canada, and 70,400 deaths due to cancer will occur. These numbers increase yearly due to an increasing and aging population. Over their lifetime, 38% of women and 44% of men will develop a form of cancer, and approximately one quarter of Canadians will die of cancer.¹ Because of this, much effort and research has been put forth in diagnosis and treatment of this disease. Three major methods of treatment of cancer are the exclusive use of – or a combination of – chemotherapy, surgery, or radiation therapy.

Radiation therapy is the branch of medicine that uses radiation in the treatment of disease, and it began soon after the discoveries of characteristic radiation by Wilhelm Conrad Röntgen in 1895² and natural radioactivity by Henri Becquerel in 1896.³ In radiation therapy, disease is treated by delivering a dose of energy through radiation, which can cure the disease or relieve pain of a patient. Despite this, damage may also be done to healthy tissue that surrounds the volume that contains the disease, as it is also responsive to radiation dose. Research in modern radiation therapy thus endeavours to maximize the dose delivered to the disease (killing cancerous cells) while sparing the healthy tissue that surrounds it.

1.2 Radiation Therapy

Radiation therapy is delivered by two general techniques; teletherapy and brachytherapy. In the latter, short range radiation originates from encapsulated radionuclide sources, which are placed inside or near the target volume in the patient. The source can deliver a dose to the target volume for a specified period (after which the source is removed), or deliver dose over the lifetime of the source (which is permanently implanted). In cases where tumours are relatively small and well localized,

brachytherapy is widely used because of its distinct advantage of improved localized dose delivery to a volume of interest. In other cases, however, teletherapy is necessary.

Teletherapy, or external beam radiotherapy, refers to therapy by radiation that originates outside of the patient. The radiation beams used most widely are photon and electron beams, but the number of clinics providing proton and neutron beam therapy is also increasing. Photon radiation beams can be produced by emissions from radioisotopes. They can also be produced by x-ray tubes or linear accelerators (also called *linacs*), where accelerated electrons strike a target, producing photon beams. As mentioned earlier, soon after the discovery of x-rays in 1895, photon beams began to be used for external beam therapy. For many years low energy photon beams produced by X-ray tubes were being used for therapy, but they were not very effective for anything other than superficial lesions because most of the dose was delivered at the skin surface. Since that time, much research and study has gone into producing higher energies of photon and electron beams for use in therapy. The greatest advancements in these fields took place with the invention of the cobalt teletherapy unit and the modern linear accelerator. The cobalt unit was invented by Dr. Harold Johns at the University of Saskatchewan in Saskatoon in the early 1950s.⁴ Its radiation beam is produced by cobalt-60, a gamma ray emitter, and its relatively simple design and average beam energy of 1.25 MeV made it the leader in external beam therapy until linear accelerators were easier to produce and market. Linacs accelerate pulses of electrons which can be used to produce a large range of high energy electron and photon beams. The large range of energies, along with the ability to use electron beams for shallower tumours and photon beams for deeper tumours, has made linacs the most widely used machines for external beam therapy.

1.3 Cell Damage and Ionizing Radiation

Radiation deposits dose in a medium in two different ways: direct ionization or indirect ionization. Direct ionization occurs when charged particles interact with atomic-bound electrons of the medium through Coulomb interactions. This can either excite the atom or release the electron, ionizing the atom. Indirect ionization occurs when neutral particles release charged particles inside of the medium, and these newly-produced

charged particles interact with electrons orbiting atoms in the medium through Coulomb interactions, depositing their energy.

Cell damage due to ionizing radiation occurs through either direct or indirect action. Direct action refers to interaction of ionizing radiation with the critical targets of cells (DNA molecules). These molecules may be excited or ionized, eventually leading to biological damage.⁵ Indirect action refers to interaction between ionizing radiation and other molecules in the cell. Cells are mainly water, and interactions with water produce free radicals that diffuse through the cell and damage DNA molecules by breaking chemical bonds, eventually resulting in biological damage.

1.4 Dosimetry

In the development of radiation therapy, it was important to have a clear understanding of how much radiation was delivered and what dose was given to a patient. A quantifier was needed in order to determine results of therapy and reproducibility of treatment. In determining the dose to a patient, it was clear that a relation had to be made to the physical effects of radiation in a volume of material, and not to the output of the radiation field itself.

No matter the type of radiation being produced, a certain dose will be given to the material being irradiated, be it a patient or a water-equivalent plastic. This dose is expressed as the amount of energy that is absorbed by a mass of the medium being irradiated. The unit of dose is called the gray ($1 \text{ Gy} = 1 \text{ J/kg}$ in S.I. units).⁶

In order to measure the dose given to a patient, an instrument called a dosimeter must be used. The part of the dosimeter that is sensitive to radiation is called the detector. The part of the dosimeter that converts the signal obtained by the detector into an electrical signal is called the reading device. There are many types of detectors. A *calorimeter* is a detector in which absorbed dose is apparent as a change in temperature in an absorber. In a *chemical dosimeter* such as a Fricke dosimeter, absorbed dose is related to chemical effects in a certain solution. In ionization chambers, absorbed dose is related to the ionization charge produced in a sensitive volume upon irradiation. *Solid-state*

detectors such as diode detectors and thermoluminescent dosimeters relate absorbed dose to solid-state effects. *Radiographic detectors* use change in film optical density to determine the absorbed dose. By far, air-filled ionization chambers are the most common detectors used in patient-treatment clinics around the world.⁷

Absorbed dose to a patient is difficult to determine directly with dosimeters. Thus a patient-similar phantom is generally used in which to measure the effects of a radiation beam. Although it is not exactly the case, the human body is considered water equivalent for purposes of radiation dosimetry. This assumption is sufficient for these purposes for two reasons. First, soft tissues in the body are very similar to water in terms of atomic composition and density because they are composed mostly of water.⁸ Corrections that could be made between these two materials are small compared to the accuracy of determination of absorbed dose, and so are neglected. The second reason is that there are a large number of different tissues in the body with a large range in structure and size. A complex determination of these parameters would possibly compromise the safety that comes from the assumption of homogeneity. Water, being easily available with well-defined characteristics, is appropriate for use. Other solid materials that simulate liquid water can also be used in dosimetry for simplification in setup, provided that corrections for any differences are applied. These materials are synthetically produced, and they exhibit a similar response to radiation as water.

1.5 Motivation

Presently, calibrations of clinical linear accelerators (linacs) are most often performed using air ionization dosimetry as outlined in the AAPM TG-51⁹ and the IAEA TRS-398¹⁰ protocols. In these protocols, air-filled ionization chambers with absorbed dose to water calibration coefficients traceable to a national standards laboratory are used. Three main problems currently exist with these chambers. First, sensitive volumes must be large enough (on the order of 0.1 to 1 cm³) to generate a high signal, which leads to low spatial resolution. Thus complex fields and areas with high dose gradients cannot be adequately studied. Second, a low density gas (such as air) causes fluence perturbations in the surrounding high density medium (such as water). Thus perturbation corrections, which are position dependent, must be applied. Third, the beam quality conversion factor

k_Q used in the protocols is dependent on the ratio of restricted stopping powers water-to-air. This ratio is energy dependent and thus k_Q changes with beam quality. Liquid ionization chambers (LICs) have features that potentially remedy these problems. Due to an ionization density 300x larger in liquid than in air, the sensitive volume of an LIC can be of the order of 1 mm^3 while maintaining a signal similar to air-filled chambers. This high spatial resolution is ideal for complex fields and areas of high dose gradient. In addition, liquids used have a density similar to water, reducing fluence perturbation. Also, for practical liquids, the ratio of restricted stopping powers liquid-to-water does not vary greatly with energy and an LIC is thus less energy dependent over a large range of beam qualities. While these attributes make the LIC attractive as an alternative to air-filled chambers, there are significant challenges with liquid chambers. The same high ionization density that allows for smaller sensitive volumes, combined with an ion mobility that is 3000 to 6000 times smaller than in air, leads to high ion recombination rates. In this thesis, properties of a new liquid ionization chamber have been investigated. This includes chamber stability over time, chamber reproducibility, and establishing recombination corrections. In addition, energy measurements by the chamber in a complex region of a radiation field have been compared to other established chambers.

References

- ¹ Canada, National Cancer Institute of, "Canadian Cancer Statistics 2006," Toronto, 2006).
- ² Curry, T. S., Christensen, E. E., Murry, R. C. *et al.*, *Christensen's physics of diagnostic radiology*, 4th ed. (Lea & Febiger, Philadelphia, 1990).
- ³ Podgorsak, E. B., *Radiation Oncology Physics: A Handbook for Teachers and Students*. (International Atomic Energy Agency, Vienna, 2005).
- ⁴ Podgorsak, E.B., *Radiation Physics for Medical Physicists*. (Springer-Verlag, Berlin Heidelberg, 2006).
- ⁵ Johns, H. E. and Cunningham, J. R., *The Physics of Radiology*, 4th ed. (Thomas, Springfield, Ill., 1983).
- ⁶ Measurements, International Commission on Radiation Units and, "Radiation quantities and units," Report No. 33, International Commission on Radiation Units and Measurements (Bethesda, Maryland, 1980).

- ⁷ Kase, K. R., Bjärngard, B. E., and Attix, F. H., *The Dosimetry of ionizing radiation*. (Academic Press, San Diego, 1985).
- ⁸ Measurements, International Commission on Radiation Units and, "Tissue substitutes in radiation dosimetry and measurement," Report No. 44, International Commission on Radiation Units and Measurements (Bethesda, Maryland, 1989).
- ⁹ Almond, P. R., Biggs, P. J., Coursey, B. M. *et al.*, "AAPM's TG-51 protocol for clinical reference dosimetry of high-energy photon and electron beams," *Med. Phys.* **26** (9), 1847-1870 (1999).
- ¹⁰ IAEA, "Absorbed Dose Determination in External Beam Radiotherapy: An International Code of Practice for Dosimetry Based on Standards of Absorbed Dose to Water," Report No. 398, International Atomic Energy Agency (Vienna, 2000).

Chapter 2

Radiation Interactions and Dosimetry

2.1 Introduction

2.2 Interactions of Ionizing Radiation with Matter

As mentioned earlier, radiation can either be ionizing or non-ionizing. To ionize an atom means to remove valence electrons from the neutral atomic structure. These electrons are held to the atomic structure with a specific binding energy. Ionizing radiation must provide enough energy to overcome the binding energy in order to release the electron. Valence electrons have a binding energy between 4 and about 25 eV, depending on the type of atom. Ionizing radiation can further be classified as direct or indirect. Photon and neutron radiation are considered indirectly ionizing radiation because they have neutral charge, and indirectly ionize atoms by first transferring energy to charged particles, which then ionize. Electrons, positrons, and protons have charge and directly interact with atoms. Radiation beams consisting of these particles are thus considered directly ionizing radiation. The most common types of indirectly ionizing and directly ionizing radiation used in medical physics are photon and electron radiation, respectively, and they will be the subject of discussion here.

2.2.1 Photon Radiation and Its Interactions

2.2.1.1 Types of Photon Radiation

There are four main types of photon radiation. The first is called *bremsstrahlung*, photons produced when charged particles interact in the field of an atomic nucleus. Kinetic energy from the charged particles is lost as they decelerate, and this energy is emitted in the form of bremsstrahlung, which are x-rays with a continuous spectrum. Modern linear accelerators use bremsstrahlung radiation to produce photon beams for radiation therapy.

The second type is called *characteristic x-rays*, produced after a lower-level atomic-bound electron is removed from an atom. A less tightly bound electron can then drop from a higher level shell, and the difference in shell binding energy is emitted in the form of x-rays. The energy of the x-rays is discrete because of the characteristic shell level binding energies.

The third type is *gamma rays*, photons produced from the nucleus of an atom that returns to a ground state from an excited state. A common use of gamma rays in radiation therapy is ^{60}Co radiation. Here, ^{60}Co nuclei emit beta particles and become ^{60}Ni nuclei. The ^{60}Ni nuclei are in an excited state, and they return to ground state by emitting two gamma ray photons of energies 1.17 MeV and 1.33 MeV. Cobalt radiation is commonly used for therapy and reference dosimetry.

The fourth type is *annihilation radiation*, whose photons are produced from positron-electron annihilation. Positrons have the same mass as electrons, and have equal but opposite charge. As they travel through a medium they will lose energy through Coulomb interactions and slow down. At some point on their path they will combine with a free electron and the two will annihilate. Two annihilation photons are then produced, each splitting the total amount of rest energy of the electron and positron plus the remaining kinetic energy of the positron (if any). Each photon will thus have energy of at least 0.511 MeV, and they travel in approximately opposite directions to conserve momentum.

2.2.1.2 Photon Radiation Interactions

Photons that are produced by any of the means previously mentioned can interact with three components of atoms in matter: orbital electrons, nuclei, or the entire atom. Interactions with orbital electrons are the photoelectric effect, Thompson and Compton scattering, and triplet production. Interaction processes involving the nucleus of an atom are pair production and photonuclear reactions. Rayleigh scattering is an effect that deals with interaction with the entire atom.

The photoelectric effect, Compton scattering, and pair and triplet production will be discussed because they are the main processes of energy transfer to media which occur in clinical radiation therapy energy ranges. In Thomson scattering (which occurs when a photon interacts with a free electron) and Rayleigh scattering (which occurs when a photon is elastically scattered by the entire atom), the photon energy does not change but its direction changes. There is little or no transfer of energy, and therefore, no absorbed dose. Thus these processes will not be discussed. Also left out will be photonuclear reactions (where nuclei absorb high energy photons and consequently emit nucleons), because the threshold for such reactions is high (~ 10 MeV) and probability of occurrence is much lower than the main interactions.

Photoelectric Effect

The photoelectric effect is most likely to occur when the binding energy E_b of a bound electron is slightly less than the energy $h\nu$ of the incident photon. The electron absorbs the photon and overcomes the binding energy, and is ejected from the shell with the following kinetic energy:

$$E_K = h\nu - |E_b|. \quad (2.1)$$

Recoil from the entire atom is negligible due to its large mass compared to the electron.

Compton Scattering

In Compton scattering, a photon interacts with a stationary electron. The electron may be bound to an atom, but it is considered free if its binding energy E_b is much less than the energy $h\nu$ of the incident photon. Some of the photon energy E_K will be transferred to the electron, leaving the photon with energy $h\nu' = h\nu - E_K$. The photon is scattered at an angle θ and the electron at an angle ϕ from the incident photon path. If conservation of momentum and energy before and after the collision are applied, expressions for scattered photon energy (equation 2.2) and the electron kinetic energy (equation 2.3) can be determined as a function of incident photon energy and photon scattering angle:

$$h\nu' = \frac{h\nu}{1 + \varepsilon(1 - \cos\theta)}; \quad (2.2)$$

$$E_K = h\nu \frac{\varepsilon(1 - \cos\theta)}{1 + \varepsilon(1 - \cos\theta)}, \quad (2.3)$$

where $\varepsilon = h\nu / m_0c^2$ is the incident photon energy normalized to $m_0c^2 = 0.511$ MeV, the rest mass energy of the electron. The scattered electron angle can also be related to the scattered photon angle and the initial photon energy:

$$\cot\phi = (1 + \varepsilon) \tan(\theta/2). \quad (2.4)$$

Pair Production and Triplet Production

In pair production, a photon in the Coulomb field of the nucleus disappears and produces an electron-positron pair. The photon energy is converted into mass of the particles, so it must be at least the threshold of $h\nu = 2m_0c^2 = 1.022$ MeV, where again m_0c^2 is the rest mass energy of the electron and of the positron. As with the photo effect, recoil of the nucleus is negligible due to its large mass. If the photon has energy $h\nu > 1.022$ MeV, the excess energy is given to the positron and electron as kinetic energies $E_{K_{e^+}}$ and $E_{K_{e^-}}$, respectively, such that the total kinetic energy is:

$$E_{K_{e^+}} + E_{K_{e^-}} = h\nu - 2m_0c^2. \quad (2.5)$$

Triplet production is similar to pair production, except that the electron-positron pair is produced when the photon interacts with the Coulomb field of an orbital electron, which is ejected from the atom in the process. The “triplet” refers to the two electrons and one positron that are produced. The photon must have enough energy to create the electron-positron pair as well as to overcome the orbital electron binding energy. Consequently, the threshold limit is larger than for pair production, and is $h\nu = 4m_0c^2$. Any excess photon energy is given to the three particles as kinetic energy.

2.2.1.3 Excited Atomic Effects

The previous section described photon interactions that result in atomic shell vacancies. When a vacancy is produced, an orbital electron in a higher atomic shell (with lower binding energy) falls into the vacancy in order to attempt to return the atom to its ground state. The difference in binding energy between the two shells is then released through characteristic x-rays, as described in section 2.2.1.1, or through the Auger effect.

Fluorescent Yield

The fluorescent yield ω is the relative probability that the energy released by a shell transition will be in the form of characteristic radiation. The yield is different for different shells, and is usually expressed as the number of photons emitted per vacancy in a shell. Fluorescent yield is dependent on the absorber atomic number. For $Z < 10$, the K-shell yield ω_K is zero, and for high Z materials, ω_K approaches 1.

Auger Effect

The process that competes with the fluorescent yield is called the Auger effect. In this process, the available energy is transferred to an orbital electron in a higher shell (then called an Auger electron), which is then ejected from the atom. The Auger electron has kinetic energy $E_K = |E_1| - |E_2| - |E_3|$, where E_1 is the binding energy of the shell with the vacancy, E_2 is the binding energy of the shell with the electron that drops to fill the vacancy, and E_3 is the binding energy of the shell containing the Auger electron. Because fluorescent yield and the Auger effect are the two competing processes, the probability for the Auger effect is $(1 - \omega)$. For absorbers with $Z < 10$, only the Auger effect is possible.

2.2.1.4 Photon Beam Attenuation and Energy Coefficients

A photon beam's intensity is attenuated in a material because the photons undergo the interactions described in section 2.2.1.2. The photon fluence at the surface ϕ_0 reduces to a photon fluence of ϕ_z at depth z (cm) according to the exponential function:

$$\phi_z = \phi_0 e^{-\mu z}, \quad (2.6)$$

where μ (units cm^{-1}) is the linear attenuation coefficient, dependent on the type attenuator material and beam energy. Often used is the mass attenuation coefficient, $\frac{\mu}{\rho}$ (cm^2/g), which is also separated into components representing the coefficients of individual interactions:

$$\frac{\mu}{\rho} = \frac{\tau}{\rho} + \frac{\sigma_R}{\rho} + \frac{\sigma_C}{\rho} + \frac{\kappa}{\rho}. \quad (2.7)$$

In this equation, τ , σ_R , σ_C , and σ_κ represent the coefficients of attenuation due to, respectively, the photoelectric effect, Rayleigh scattering, Compton scattering, and pair production.

Each mass attenuation coefficient can further be written as a function of energy transfer $\frac{\mu_{tr}}{\rho}$ and energy absorption $\frac{\mu_{en}}{\rho}$ coefficients. These describe the fraction of energy that is transferred to charged particles, and the fraction of transferred energy that is absorbed by the medium, respectively. These are related by the bremsstrahlung fraction \bar{g} , which is the fraction of transferred energy lost through radiative interactions:

$$\frac{\mu_{en}}{\rho} = \frac{\mu_{tr}}{\rho} (1 - \bar{g}). \quad (2.8)$$

The amount of energy that is transferred to charged particles is different for different interactions. Thus the energy transfer coefficient is separated by interactions:

$$\frac{\mu_{tr}}{\rho} = \frac{\mu}{\rho} \frac{\bar{E}_{tr}}{h\nu} = \frac{\tau_{tr}}{\rho} + \frac{\sigma_{tr}}{\rho} + \frac{\kappa_{tr}}{\rho} = \frac{1}{\rho} \left[\tau \frac{(\bar{E}_{tr})_\tau}{h\nu} + \sigma \frac{(\bar{E}_{tr})_\sigma}{h\nu} + \kappa \frac{(\bar{E}_{tr})_\kappa}{h\nu} \right], \quad (2.9)$$

where (\bar{E}_{tr}) is the average energy that is transferred to charged particles as a result of each interaction. Note that Rayleigh scattering is not included because it does not result

in any transfer of energy to charged particles (see section 2.2.1.2). Compton scattering is thus represented with no subscript, for simplicity.

As seen in section 2.2.1.2, energy transferred in the photoelectric effect is given by equation 2.1. We must take into account the probability P_K that the interaction will take place in the first (or K) shell, the fluorescent yield ω_K , and the mean energy of transitions to the K-shell, $\overline{h\nu_K}$. $\overline{h\nu_K}$ is approximately 86% of the K-shell binding energy of an absorber. Thus the energy transferred is:

$$(\overline{E}_{tr})_p = h\nu - P_K \omega_K \overline{h\nu_K}. \quad (2.10)$$

For Compton scattering, the mean energy transferred to charged particles depends on the initial photon energy. Maximum and average values for $(\overline{E}_{tr})_\sigma$ are determined using tables or graphs such as the one shown in Fig. 2-1.

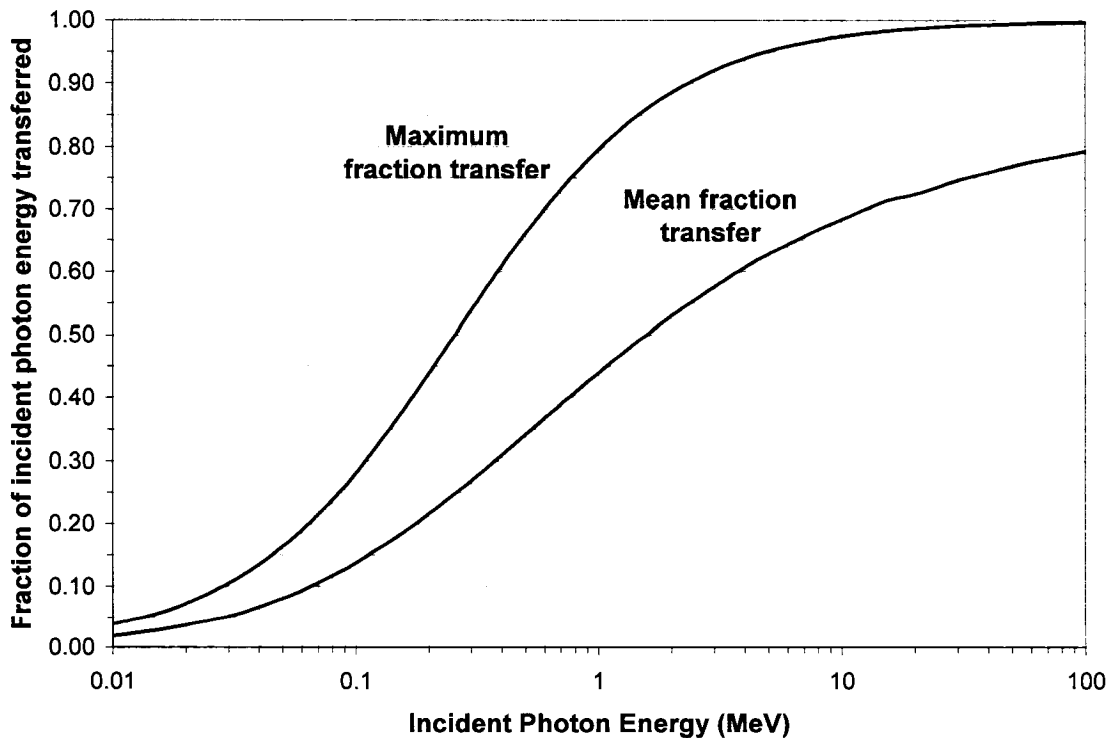


Figure 2-1. Maximum and mean fractions of incident photon energy transferred to scattered electron in the Compton effect.¹

For pair production, the mean energy transferred to charged particles is:

$$\left(\bar{E}_{tr}\right)_\kappa = h\nu - 2m_e c^2, \quad (2.11)$$

as described in section 2.2.1.2.

Thus the total mass energy transfer coefficient is:

$$\frac{\mu_{tr}}{\rho} = \frac{1}{\rho} \left[\tau \frac{h\nu - P_\kappa \omega_\kappa \overline{h\nu_\kappa}}{h\nu} + \sigma \frac{\left(\bar{E}_{tr}\right)_\sigma}{h\nu} + \kappa \frac{h\nu - 2m_e c^2}{h\nu} \right]. \quad (2.12)$$

A photon interaction may show predominance over the other interactions, depending on the photon energy and the atomic number of the absorber. As seen in Fig. 2-2, the photoelectric effect is dominant at lower energies, the Compton effect at intermediate energies, and pair production at higher energies. In radiation therapy, most photon beam energies range between 1 and 10 MeV, and water has an effective atomic number of about 7, thus the predominant photon interaction that occurs in radiation therapy is the Compton effect.

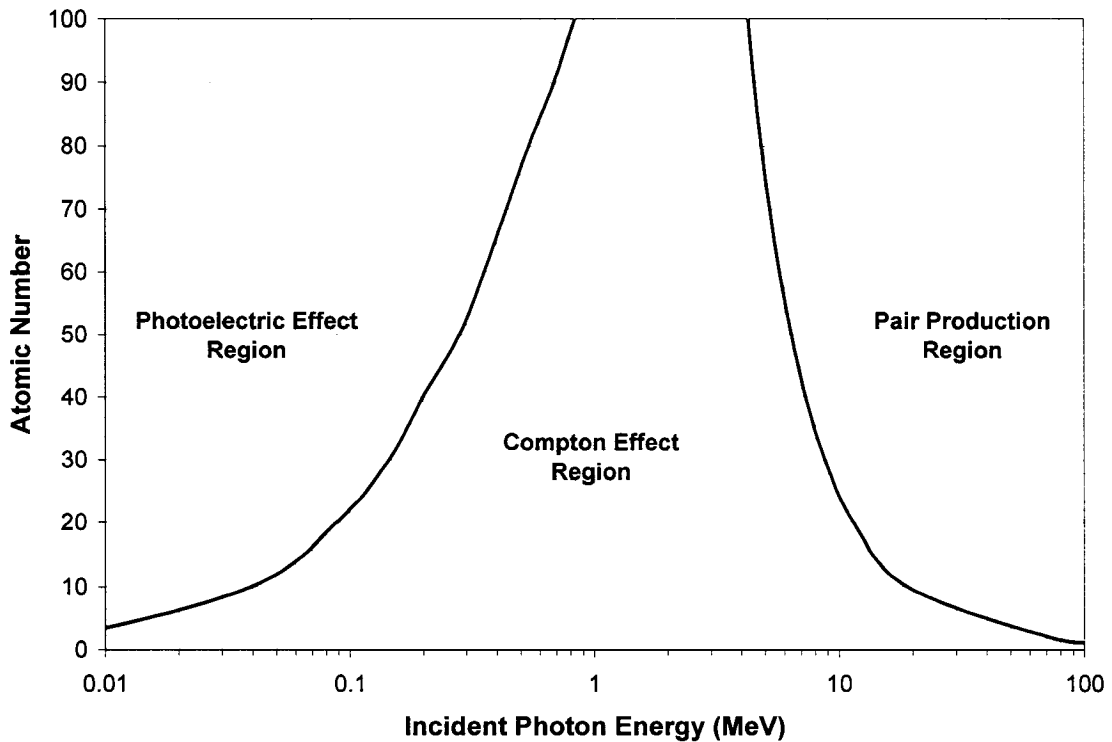


Figure 2-2. Relative predominance of photoelectric effect, Compton effect, and pair production for elements with atomic numbers 1-100 and over a large photon energy range. The left curve corresponds to points where the atomic photoelectric effect and atomic Compton effect coefficients are equal, and the right curve corresponds to points where the atomic Compton effect and atomic pair production coefficients are equal.²

2.2.2 Electron Radiation and Its Interactions

2.2.2.1 Interactions with Matter

Because electrons are charged particles, they will interact with the Coulomb fields of orbital electrons and nuclei of atoms. A high energy electron will interact thousands of times as it travels through a material, and statistical theory is used to describe their behaviour.

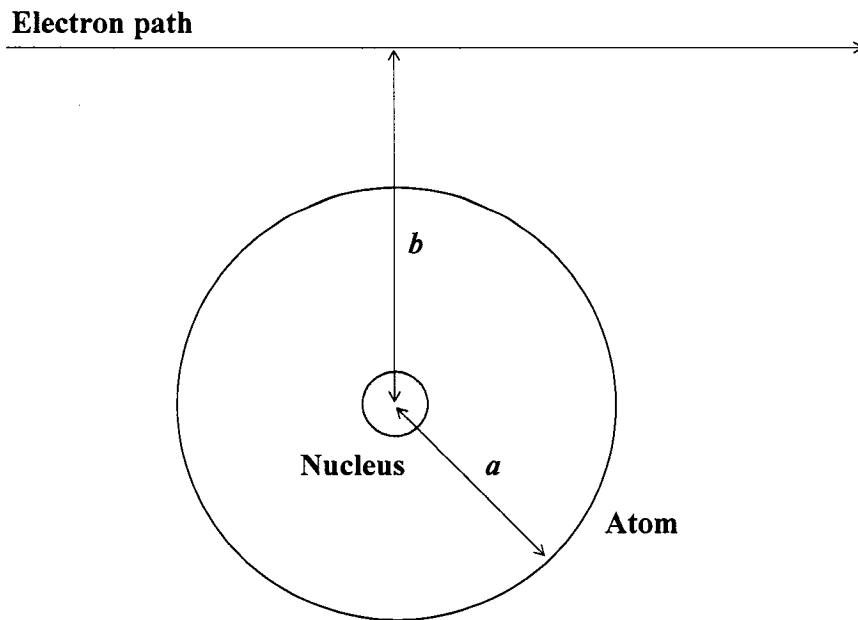


Figure 2-3. Electron-atom interaction, with the impact parameter b and atomic radius a . Soft collisions occur where $b \gg a$, hard collisions occur where $b \approx a$, and nuclear interactions occur where $b \ll a$.

These interactions take place in the form of collisions. These collisions can be elastic, where the electron is scattered yet no energy loss occurs, or inelastic, where scatter as well as energy loss occurs. In the case where energy loss occurs, the transfer of energy depends on the impact parameter b and the atomic radius a , which are shown in Fig. 2-3.

Three types of energy transfer can occur:

1. Soft collisions ($b \gg a$). In this case, the electron interacts with the whole atom and transfers a small amount of energy to orbital electrons, either exciting or ionizing the atom. This is the most common type of interaction, but because little energy is transferred the electron will lose about half its energy through soft collisions.
2. Hard collisions ($b \approx a$). In this case, the incoming electron interacts with and can transfer up to half of its kinetic energy to a single orbital electron. These electrons can be ejected from the atom and have gained sufficient energy in the collision to ionize other atoms. The electron with the higher

amount of kinetic energy after the collision is considered to be the incident electron. Thus, the maximum energy transfer is half the kinetic energy because the particles are indistinguishable. An incoming positron, on the other hand, is distinguishable from an orbital electron and so its maximum energy loss is its total kinetic energy. Hard collisions are not as common as soft collisions, but the energy transferred is much larger, so this process accounts for about half of the energy loss of the incoming electron.

3. Nuclear interactions ($b \ll a$). This process is the least likely of the three, due to the small impact parameter. In this process, the electron interacts with the coulomb field of the nucleus and is scattered. 98% of these interactions are elastic, where the electron is scattered with no loss of kinetic energy. 2% are inelastic, and the electron is scattered and loses energy in its deceleration. This energy is lost in the form of bremsstrahlung photons, and the power lost to these photons is determined from the Larmor relationship:

$$P = \frac{q^2 a^2}{6\pi\epsilon_0 c}, \quad (2.13)$$

where q is the charge of the incoming particle, a is its acceleration, ϵ_0 is the permittivity of free space, and c is the speed of light. It is interesting to note that the power emitted is proportional to a . The acceleration, from Newton's second law, is in turn inversely proportional to the mass of the particle. Thus bremsstrahlung production is inversely proportional to $\frac{1}{m^2}$.

This means that bremsstrahlung production is only significant for light charged particles such as electrons and positrons.

2.2.2.2 Stopping Power

As an electron travels through a medium, it loses kinetic energy through the mechanisms defined in the last section. The amount of kinetic energy dE_k lost by an

electron in a thickness dx of a medium is called the linear stopping power of that medium:

$$S = \frac{dE_K}{dx}. \quad (2.14)$$

A conventional form of stopping power used is the mass stopping power, which takes into account the density ρ (with units g/cm^3) of the medium:

$$\frac{S}{\rho} = \frac{dE_K}{\rho dx}. \quad (2.15)$$

The units of stopping power and mass stopping power are usually expressed as MeV/cm and $\text{MeV} \cdot \text{cm}^2/\text{g}$, respectively.

There are two components of stopping power:

1. collisional stopping power, where energy is lost due to atomic excitations and ionizations resulting from hard and soft collisions, and
2. radiative stopping power, where energy is lost to bremsstrahlung radiation.

Thus mass stopping power can be divided into these two components:

$$\left(\frac{S}{\rho}\right)_{\text{total}} = \left(\frac{S}{\rho}\right)_{\text{coll}} + \left(\frac{S}{\rho}\right)_{\text{rad}}. \quad (2.16)$$

The components are distinctive because collisional stopping power is used to determine the absorbed dose in the medium, while radiative stopping power carries energy away from the area, and thus does not contribute to the absorbed dose.

Mass Radiative Stopping Power

The equation for mass radiative stopping power is:³

$$\left(\frac{S}{\rho}\right)_{\text{rad}} = \bar{B}_r \frac{N_A}{A} Z^2 \alpha r_e^2 (E_K + m_e c^2), \quad (2.17)$$

where N_A is Avogadro's number, $\alpha \approx \frac{1}{137}$ is the fine structure constant, r_e is the classical electron radius, A is the atomic mass number, Z is the atomic number, E_K is the electron kinetic energy, $m_e c^2$ is the electron rest mass energy, and \bar{B}_r is a function of Z and the total electron energy that slowly varies from $\frac{16}{3}$ (for energies less than 0.5 MeV) to 15 (for 100 MeV). For all elements except hydrogen, the ratio $\frac{Z}{A}$ is approximately 0.5. This means that the mass radiative stopping power is approximately proportional to Z , the atomic number of the absorber.

Mass Collisional Stopping Power

The equation for mass collisional stopping power for light charged particles is:⁴

$$\left(\frac{S}{\rho}\right)_{\text{coll}} = 2\pi r_e^2 \frac{ZN_A}{A} \frac{m_e c^2}{\beta^2} \left[\ln\left(\frac{E_K}{I}\right)^2 + \ln\left(1 + \frac{\tau}{2}\right) + F^\pm(\tau) - \delta \right], \quad (2.18)$$

where, for electrons,

$$F^-(\tau) = (1 - \beta^2) \left[1 + \frac{\tau^2}{8} - (2\tau + 1) \ln 2 \right], \quad (2.19)$$

and for positrons,

$$F^+(\tau) = 2 \ln 2 - \left(\frac{\beta^2}{12}\right) \left[23 + \frac{14}{\tau + 2} + \frac{10}{(\tau + 2)^2} + \frac{4}{(\tau + 2)^3} \right]. \quad (2.20)$$

In these equations, I is the mean excitation energy $\beta = v/c$ (the particle velocity v normalized by the speed of light c) and $\tau = E_K / m_e c^2$ (the particle kinetic energy E_K

normalized by the rest mass energy of an electron $m_e c^2$), and δ is the density effect, which is explained below.

The mean excitation energy is the average energy needed in an atom in order to excite any orbital electron, and it is only dependent on the type of atom (stopping medium). Values are given in ICRU Report 37,⁴ but it is roughly approximated by $(11.5 \text{ eV})Z$.³

The density effect takes into account the fact that Coulomb fields of distant particles are screened by polarization due to passing charged particles. This screening limits the amount of energy that could be transferred, decreasing the stopping power. The density effect differs with type of material, but it is not important in gases, which have a low density of atoms compared to liquids and solids.

2.3 Dosimetric Quantities

2.3.1 Particle Fluence

A fundamental quantity in radiation dosimetry, upon which many other quantities are based, is called particle fluence. Particle fluence Φ (units m^{-2}) is defined as the number of particles dN that are incident on a sphere of cross-sectional area dA :

$$\Phi = \frac{dN}{dA}. \quad (2.21)$$

The incident particles are counted over the entire sphere (shown in Fig. 2-4), so there will always be an area dA perpendicular to each particle. Thus the particle fluence is independent of incident angle. A similar quantity is called planar particle fluence, which is the number of particles crossing a plane per unit area. Planar fluence is thus dependent on the particle angle of incidence.

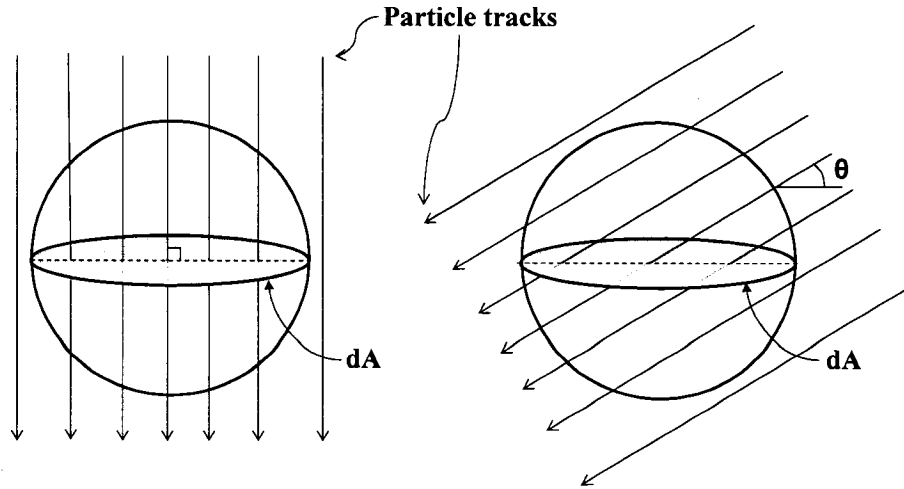


Figure 2-4. Role of angle of incidence in particle fluence and planar fluence. Particle fluence is independent of angle, while planar fluence is dependent on angle.

2.3.2 Energy Fluence

Energy fluence Ψ (units J/m^2) is similar to particle fluence, but it also takes into account the energy of the particles that are incident on the sphere of cross-sectional area dA :

$$\Psi = \frac{dN}{dA} E = \Phi E. \quad (2.22)$$

This is the case for monoenergetic particles. When a particle beam is polyenergetic, as is usually the case, the spectrum of energies must be taken into account. $\Phi_E(E)$ is the particle fluence spectrum:

$$\Phi_E(E) = \frac{dN(E)}{dA}, \quad (2.23)$$

where $dN(E)$ is the number of particles with energy E . $\Psi_E(E)$ is the energy fluence spectrum, which is determined from the particle fluence spectrum:

$$\Psi_E(E) = \Phi_E(E) \cdot E \quad (2.24)$$

The total energy fluence is:

$$\Psi = \int_0^{E_{\max}} \Phi_E(E) \cdot E dE \quad (2.25)$$

where the particle fluence spectrum is integrated over the range of energies.

2.3.3 Kerma

Kerma stands for **K**inetic **E**nergy **R**elaxed per unit **M**Ass. It is a quantity used in indirectly ionizing radiation, where energy from neutral particles such as photons and neutrons is transferred to charged particles in matter. Kerma does not take into account what happens to the energy after it is transferred. It is defined as the mean energy transferred $d\bar{E}_{tr}$ per unit mass dm of the medium:

$$K = \frac{d\bar{E}_{tr}}{dm} \quad (2.26)$$

By this definition, the units of kerma are the same as absorbed dose, and the unit gray also applies here (1 Gy = 1 J/Kg). Kerma can also be related to the energy fluence

Ψ through $\left(\frac{\bar{\mu}_{tr}}{\rho}\right)_{med}$, the average mass energy transfer coefficient in the medium:

$$K = \Psi \left(\frac{\bar{\mu}_{tr}}{\rho}\right)_{med} \quad (2.27)$$

This relationship is helpful in relating kerma in two different materials if the fluence in two media is the same. This is done by taking the ratio of equation (2.27) for the materials composing the two media med_1 and med_2 :

$$K_{med_1} = \left(\frac{\bar{\mu}_{tr}}{\rho}\right)_{med_1} K_{med_2} \quad (2.28)$$

The energy transferred from indirectly ionizing radiation to charged particles in the medium can be divided into two categories:

1. energy expended through soft and hard collisions, and
2. energy expended through radiative interactions such as bremsstrahlung and in-flight annihilation.

In the first case, energy is transferred directly to the medium. In the second case, energy leaves the volume of interest in the form of photons. These differences are divided into two components of kerma:

$$K = K_{coll} + K_{rad} , \quad (2.29)$$

where K_{coll} is the collisional component and K_{rad} is the radiative component. The fraction of energy lost through radiative interactions is called \bar{g} , so the fraction expended through collisions is $(1 - \bar{g})$. Thus collisional kerma can also be written as:

$$K_{coll} = K(1 - \bar{g}) , \quad (2.30)$$

and radiative kerma can be written as:

$$K_{rad} = K(\bar{g}) . \quad (2.31)$$

2.3.4 Exposure

When a volume of air is irradiated by ionizing radiation, charge is produced in the volume. Exposure X describes this amount of charge. Its formal definition is the amount of charge dQ of ions of one sign produced in a volume of dry air of mass dm when all the charged particles produced by photons are completely stopped in air:

$$X = \frac{dQ}{dm} . \quad (2.32)$$

By this definition, the units of exposure in S.I notation are C/kg. The historical unit of exposure is the roentgen, and its value is $1 \text{ R} = 2.58 \times 10^{-4} \text{ C/kg}$. Exposure does not include energy losses to the produced charged particles by radiative processes. Exposure can thus be considered to be the ionization equivalent of collisional kerma, and the two can be related. This is done by introducing the amount of energy that is required to produce an ion pair in dry air. This ratio is expressed as $\left(\frac{\bar{W}}{e}\right)_{\text{air}}$ and its currently accepted value is:³

$$\left(\frac{\bar{W}}{e}\right)_{\text{air}} = 33.97 \text{ J/C}. \quad (2.33)$$

The amount of energy required to produce an ion pair $\left(\frac{\bar{W}}{e}\right)_{\text{air}}$, multiplied by the amount of charge produced per unit mass of a medium $\left(\frac{dQ}{dm}\right)$, will thus give the amount of energy deposited in a mass of air $\left(\frac{d\bar{E}_{tr}}{dm}\right)$. Therefore, exposure is related to collisional kerma by:

$$X = K_{coll} \left(\frac{e}{\bar{W}_{air}}\right). \quad (2.34)$$

Exposure can then be related to total kerma by using equation (2.30):

$$X = K(1 - \bar{g}) \left(\frac{e}{\bar{W}_{air}}\right). \quad (2.35)$$

2.3.5 Charged Particle Equilibrium

The goal in radiation dosimetry is to determine absorbed dose. Although a beam of photons transfers energy to charged particles (kinetic energy released to matter, or kerma), that energy is not deposited at the position where the transfer occurs. Due to the

range of charged particles, energy is deposited at a different location. The absorbed dose can efficiently be determined from kerma but only under conditions of charged particle equilibrium (CPE). If CPE does not exist, relating kerma to absorbed dose can be complex. CPE exists when a charged particle that is exiting a volume is replaced by an identical charged particle (i.e. same particle type and energy) entering the volume. Thus the number of like charged particles within the volume remains the same, so the absorbed dose is the same as the kerma. In the volume, the ratio of absorbed dose, D , to collisional kerma, K_{col} , is given by:

$$\beta = D/K_{\text{col}} \quad (2.36)$$

This ratio depends on the beam energy and the material in which energy transfer takes place.

A common example illustrating CPE (and lack thereof) is given in section 2.6.1. Section 2.6 explains the complexities of non-equilibrium radiation dosimetry.

2.4 Cavity Theory

Dosimeters are necessary in order to measure the absorbed dose in a medium. However, the dosimeter only produces a signal that is related to the absorbed dose in the medium of its own sensitive volume, rather than the absorbed dose to the medium in which the dosimeter is inserted. These media are not necessarily the same, thus resulting in a cavity in the surrounding medium. In clinical ionization dosimetry, the cavity is commonly air and the surrounding medium is water. In order to determine the absorbed dose to the surrounding medium from the dose to the cavity, *cavity theory* is used.

In cavity theory, the relative size of the cavity is determined by the range of secondary charged particles that are produced by the photon beam. A small cavity, therefore, is determined by secondary charged particles whose range is large compared to the size of the cavity. This small cavity is the basis for two cavity theories called the Bragg-Gray and the Spencer-Attix theories.

2.4.1 Bragg-Gray Cavity Theory

The Bragg-Gray cavity theory was developed in order to relate the absorbed dose in a detector medium to the absorbed dose of the medium in which the detector is placed.

There are two conditions that must apply in order for Bragg-Gray cavity theory to apply:³

1. The cavity must be small, compared to the range of secondary charged particles incident on it, so that the fluence of charged particles is not perturbed by the cavity.
2. The absorbed dose in the cavity is only due to interactions of charged particles crossing it, rather than interactions of photons.

In a volume of interest in a medium, the absorbed dose D_{med} is related to the electron fluence Φ_{med} by the following relationship:

$$D_{med} = \Phi_{med} \left(\frac{\bar{S}_{coll}}{\rho} \right)_{med}, \quad (2.37)$$

where $\left(\frac{\bar{S}_{coll}}{\rho} \right)_{med}$ is the unrestricted mass collisional stopping power of the medium, averaged over the electron energy spectrum. This relationship assumes that radiative photons escape the volume of interest and that secondary charged particles are absorbed on the spot when they are produced. In reality, charged particles travel some finite distance before being absorbed, and may leave the volume. However, in regions of CPE these charged particles that leave the volume are replaced by others that enter, and the assumption holds. The absorbed doses to two different media where CPE exists, then, can be related as the following ratio:

$$\frac{D_{med_1}}{D_{med_2}} = \frac{\Phi_{med_1} \left(\frac{\bar{S}_{coll}}{\rho} \right)_{med_1}}{\Phi_{med_2} \left(\frac{\bar{S}_{coll}}{\rho} \right)_{med_2}} = \Phi_{med_2}^{med_1} \left(\frac{\bar{S}_{coll}}{\rho} \right)_{med_2}^{med_1}, \quad (2.38)$$

where $\Phi_{med_2}^{med_1}$ is the ratio of electron fluences in the different media and $\left(\frac{\bar{S}_{coll}}{\rho} \right)_{med_2}^{med_1}$ is the ratio of averaged unrestricted mass collisional stopping powers in the different media. If we apply condition 1 of Bragg-Gray cavity theory, the charged particle fluence is the same for both media and $\Phi_{med_2}^{med_1} = 1$. Condition 2 implies that no secondary charged particles are produced inside the cavity, and those produced outside completely cross the cavity. Assuming these two conditions, and applying the Bragg-Gray cavity theory conditions, equation 2.38 can be written as:

$$\frac{D_{med}}{D_{cav}} = \left(\frac{\bar{S}_{coll}}{\rho} \right)_{cav}^{med}, \quad (2.39)$$

where *cav* refers to the cavity medium and *med* refers to the medium surrounding the cavity. In order for this relationship to exist, CPE must be present. Due to the conditions, Bragg-Gray cavity theory is dependent on the size of the cavity, the electron range, and cavity medium. For example, a cavity that is small enough to qualify as a Bragg-Gray cavity in a high-energy photon beam may not qualify in a lower-energy x-ray beam because its size is too large compared to the range of secondary charged particles crossing it.

2.4.2 Spencer-Attix Cavity Theory

The Spencer-Attix cavity theory⁵ was developed with the purpose of extending the Bragg-Gray Cavity theory to include the creation of secondary charged particles produced in the slowing down process of the primary electrons crossing the cavity. This theory is closer to reality in that it takes into account the production of secondary electrons that may have sufficient energy to generate further ionizations or excitations, or to even

escape from the cavity. In Spencer-Attix cavity theory, Bragg-Gray conditions still must be met not only by the primary charged particles, but also by the secondary charged particles.

Electrons in the spectrum of secondary charged particles (delta electrons) have a maximum kinetic energy E_{K_0} , which is the initial energy of the primary electrons. Delta electrons that cannot make it out of the cavity, and deposit all their energy inside the cavity, are considered “slow” electrons. These slow electrons have a kinetic energy E_K that is less than the energy Δ . Δ is defined as the energy of an electron with a range that is equal to the mean chord length across the cavity, and is thus related to the cavity size. Some of the delta electrons can escape the cavity and are considered “fast” electrons, in that they contribute to energy transfer in the cavity in the slowing down process but are not absorbed themselves. Thus fast electrons have energy in the range of Δ to E_{K_0} , and energy lost by these electrons in the cavity is included in the dose calculation. If a fast electron has energy E_K in the range $\Delta \leq E_K < 2\Delta$, the maximum energy transferred is $\frac{E_{K_0}}{2} < \Delta$. If a fast electron has energy E_K in the range $2\Delta \leq E_K < E_{K_0}$, the maximum energy transferred is Δ . Thus the stopping power must be restricted to the threshold Δ , and is called the mean restricted mass collisional stopping power $\frac{L_{\Delta}(E_K)}{\rho}$. According to Spencer-Attix theory, the absorbed dose to the medium is related to the absorbed dose to the cavity:

$$\frac{D_{med}}{D_{cav}} = \left(\frac{\bar{L}_{\Delta}}{\rho} \right)_{cav}^{med} \quad (2.40)$$

The ratio of mean restricted mass collisional stopping powers is fully expressed as:⁶

$$\left(\frac{\bar{L}_{\Delta}}{\rho} \right)_{cav}^{med} = \frac{\int_{\Delta}^{E_{K_0}} \Phi_{E_K}^{med,\delta}(E_K)(L_{\Delta,med}/\rho)dE_K + TE_{med}}{\int_{\Delta}^{E_{K_0}} \Phi_{E_K}^{med,\delta}(E_K)(L_{\Delta,cav}/\rho)dE_K + TE_{cav}}, \quad (2.41)$$

where $\Phi_{E_K}^{med,\delta}$ is the fluence of fast electrons, and TE_{med} and TE_{cav} are called the *track-end* terms. These terms take into account electrons with energies in the range $\Delta \leq E_K < 2\Delta$, that have energy losses in the cavity which bring their energies below Δ . These electrons are thus removed from the fast electron spectrum, and the track-end terms are approximated as:

$$TE_{med} = \Phi_{E_K}^{med,\delta}(\Delta) \frac{S_{med}(\Delta)}{p} \Delta \quad (2.42)$$

and

$$TE_{cav} = \Phi_{E_K}^{med,\delta}(\Delta) \frac{S_{cav}(\Delta)}{p} \Delta. \quad (2.43)$$

Ionization chambers used in radiation therapy typically have a cut-off energy on the order of about 10 keV in order to restrict secondary electrons that might deposit energy outside of the volume which can be less than a cubic centimetre.

2.5 Air-kerma-in-air-based Protocols

Protocols exist in order to determine the absorbed dose to water based on a signal obtained by a detector. They supply the method and other data needed for this conversion. Air-kerma-based protocols such as AAPM TG-21⁷ use the air-kerma-in-air calibration coefficient $N_{K,Co}$ to relate a chamber signal corrected for influence quantities M_Q to the air-kerma-in-air $(K_{air})_{air}$:

$$N_{K,Co} = \frac{(K_{air})_{air}}{M_Q}. \quad (2.44)$$

In these protocols, $(K_{air})_{air}$ is known in a calibration beam such as ^{60}Co , and a value for $N_{K,Co}$ is determined. The dose-to-air in the cavity in the calibration beam is related to $(K_{air})_{air}$ by:

$$D_{\text{air}} = (K_{\text{air}})_{\text{air}} (1 - \bar{g}) k_{\text{m}} k_{\text{att}} k_{\text{cel}}, \quad (2.45)$$

where \bar{g} is the fraction of photon energy that is radiated away as a result of electrons slowing down in air, k_{m} corrects for the difference in material between air and the cavity wall and build-up cap, k_{att} corrects for photon attenuation and scatter in the chamber wall, and k_{cel} corrects for the difference between the chamber central electrode material and air. The dose-to-air calibration coefficient relates the relate a chamber signal corrected for influence quantities M_Q to the dose-to-air D_{air} :

$$N_{\text{D,air}} = \frac{D_{\text{air}}}{M_Q}. \quad (2.46)$$

This coefficient would not have to be determined in a standards laboratory if the sensitive volume of the chamber were known, because the dose to the air is given by:

$$D_{\text{air}} = \frac{Q_{\text{air}}}{m_{\text{air}}} \left(\frac{\bar{W}}{e} \right)_{\text{air}}, \quad (2.47)$$

where Q_{air} is the charged produced in the chamber, m_{air} is the mass of the air, and $\left(\frac{\bar{W}}{e} \right)_{\text{air}}$ is the amount of energy that is required to produce an ion pair in air. The mass of the air is the product of the air density and the sensitive volume. The volume, however, is generally not accurately known, and thus the dose-to-air calibration coefficient must be determined in the standards laboratory where chambers of known volume are used.

Isolating $(K_{\text{air}})_{\text{air}}$ in equation 2.44 and substituting into equation 2.45, the dose-to-air is related to the dose-to-air calibration coefficient:

$$D_{\text{air}} = N_{\text{K,Co}} M_Q (1 - g) k_{\text{m}} k_{\text{att}} k_{\text{cel}}, \quad (2.48)$$

which can be substituted into equation 2.46 to express the dose-to-air calibration coefficient in terms of the air-kerma-in-air calibration coefficient:

$$N_{D,\text{air}} = N_{K,\text{Co}} (1-g) k_m k_{\text{att}} k_{\text{cel}}. \quad (2.49)$$

In the user's beam, then, the absorbed-dose-to-medium (such as water), can be determined from the Bragg-Gray relation in equation 2.39:

$$\frac{D_{\text{med}}}{D_{\text{air}}} = \left(\frac{\bar{S}_{\text{coll}}}{\rho} \right)_{\text{air}}^{\text{med}}. \quad (2.50)$$

A measurement M_Q is taken in the user beam. The dose to air D_{air} is simply $N_{D,\text{air}} M_Q$ (from equation 2.46). This, along with the expression for $N_{D,\text{air}}$ in equation 2.50, is substituted into the Bragg-Gray relationship to give an expression for the absorbed-dose-to-medium in terms of the air-kerma-in-air calibration coefficient that was determined in the calibration beam:

$$D_{\text{med}} = M_Q N_{K,\text{Co}} \left(\frac{\bar{S}_{\text{coll}}}{\rho} \right)_{\text{air}}^{\text{med}} (1-g) k_m k_{\text{att}} k_{\text{cel}} P_Q, \quad (2.51)$$

where P_Q is a perturbation correction factor, accounting for the replacement of the medium with air, for the non-water equivalence of the chamber wall and central electrode, and charged particle in-scattering (explained in section 3.3.2).

2.6 Absorbed-dose-to-water-based Protocols

The goal in radiation dosimetry is to determine the absorbed dose to water and we have seen that the goal of air-kerma-based protocols is to accomplish this. Other protocols, however, attempt to determine the absorbed dose to water directly, without going through an air-kerma calibration free-in-air. The most commonly-used absorbed-dose-to-water-based protocols are the IAEA TRS-398⁸ and the AAPM TG-51⁹ protocols. In these protocols, calibrations of ion chambers are made in water based on reference conditions in a reference radiation beam, usually ^{60}Co , where a chamber-specific calibration coefficient is assigned. This coefficient, $N_{D,w}^{Q_0}$, relates the absorbed dose to water, $D_w^{Q_0}$, at a reference depth in the reference beam, Q_0 , to the corrected chamber reading, M_{Q_0} , as given in equation 2.52.

$$D_w^{Q_0} = M^{Q_0} N_{D,w}^{Q_0}. \quad (2.52)$$

The reading M^{Q_0} corrects the raw chamber reading M for properties that can change the signal such as physical properties of air, chamber polarity effects, ion recombination effects, and stem effects. These influence quantities are further defined later in section 3.2. The relationship in equation 2.52 exists for any beam with quality Q :

$$D_w^Q = M^Q N_{D,w}^Q. \quad (2.53)$$

2.6.1 Beam Quality Conversion Factor

The calibration coefficient, $N_{D,w}^Q$, that relates the corrected reading to the absorbed dose in the user's beam, however, must also be related to the coefficient defined in the reference beam. The ratio of these two is called the beam quality conversion factor:

$$k_Q = \frac{N_{D,w}^Q}{N_{D,w}^{Q_0}}. \quad (2.54)$$

Solving equation 2.54 for $N_{D,w}^Q$ and substituting into equation 2.53 will give the absorbed dose to water in the user's beam:

$$D_w^Q = M^Q k_Q N_{D,w}^{Q_0}. \quad (2.55)$$

If the chamber is not inherently waterproof, a sleeve may have to be used while being irradiated in a water phantom by the reference beam. In this case, the same or a similar sleeve must be used while calibrating in the user's beam. The reference calibration coefficient is chamber dependent, so the beam quality conversion factor is as well. The protocols provide different values of k_Q for many commercial chambers, so that the user need only acquire $N_{D,w}^{Q_0}$ from the standards laboratory in order to determine D_w^Q .

2.6.2 Beam Quality Specification

In order to determine the absorbed dose to water, the ionization chamber reading must be multiplied by influence quantities and other physical quantities. These quantities depend on the properties of the chamber, but some also depend on the radiation beam that is used. For this reason, beam qualities must be specified. Practical approaches have been developed in order to specify the beam quality of kilovoltage x-ray beams, megavoltage photon beams, and megavoltage electron beams. Here we will discuss the latter two, as megavoltage beams were used in this research.

2.6.2.1 Megavoltage Photon Beams

One simple way would be to assign photon beam nominal energies as beam quality specifiers (i.e. 6 MV, 18 MV) but these beams are not monoenergetic due to the large photon spectrum that is produced by the electron beam interacting with the target. While older protocols did use nominal accelerating potential as a specifier, modern protocols use specifiers that distinguish the uniqueness of each beam. The IAEA protocol⁸ uses the tissue phantom ratio TPR_{10}^{20} which is defined as the ratio of doses at 20 cm and 10 cm in water along the central axis of a beam with a field size of $10 \times 10 \text{ cm}^2$ at the detector depth, with a constant source to detector distance of 100 cm. The AAPM TG-51 protocol⁹ uses the percent depth dose $\%dd(10)_x$ which is defined as the percentage of dose at 10 cm depth compared to the dose at depth of maximum dose for a beam with field size of $10 \times 10 \text{ cm}^2$ at the phantom surface, which must be held constant at 100 cm SSD, with the unknown amount of electron contamination having been removed. This is accomplished by placing a 1 mm-thick lead foil in the path of the beam, 50 cm from the phantom surface. The foil minimizes the beam electron contamination and adds a known level of electron contamination which can be subtracted in order to determine $\%dd(10)_x$. In clinical beams, both TPR_{10}^{20} and $\%dd(10)_x$ produce the same absorbed dose to water, and thus either are adequate for calibration of chambers in

clinical beams. TPR_{10}^{20} , however, is not appropriate for use in some beams at standards laboratories.

2.6.2.2 Megavoltage Electron Beams

The megavoltage electron beam produced by a linear accelerator is basically monoenergetic, but interactions with components of the linac and with air produce an energy spectrum by the time it reaches the surface of the phantom. Thus the nominal monoenergetic energy is not a sufficient beam quality specifier. For many years the average energy of the electron beam at the surface of the phantom \bar{E}_0 was used as a specifier by almost all dosimetry protocols. This quantity was determined using R_{50} , the depth at which the dose due to the beam is 50% of the maximum dose in a water phantom. The AAPM TG-21 protocol⁷ accomplishes this by multiplying R_{50} by a constant C which equals 2.33 MeV/cm. For the specification of stopping power ratios, one needs the specifiers \bar{E}_0 and the practical range R_p .

Another useful quantity, though not a beam quality specifier, is the average energy of the beam at a depth in the phantom (\bar{E}_z) where z is the depth in cm. TG-21 uses the Harder relationship to determine \bar{E}_z from the depth and R_p :

$$\bar{E}_z = \bar{E}_0 \left[1 - \frac{z}{R_p} \right]. \quad (2.56)$$

The practical range of the electron beam is defined as the depth at which an extrapolation of the tangent at the steepest point on the dose falloff curve meets a backward extrapolation of the bremsstrahlung tail. A typical electron beam depth dose curve, normalized to 100% at d_{\max} (depth of maximum dose) is shown in Fig. 2.5 and illustrates the quantities d_{\max} , R_{50} and R_p .

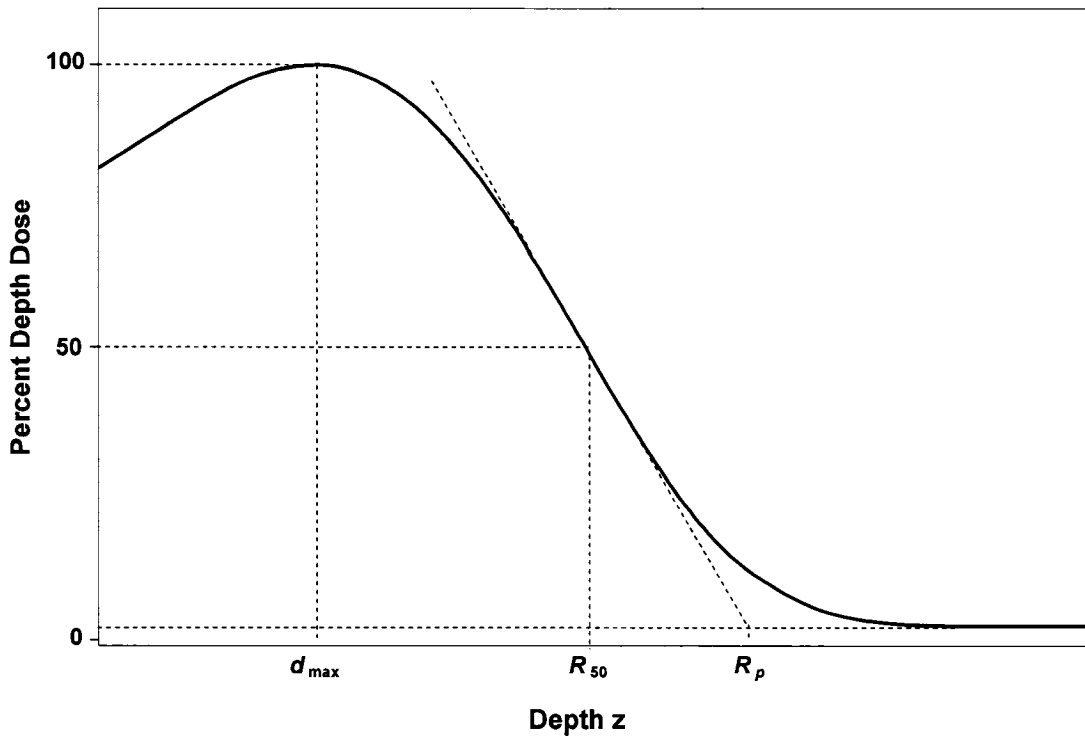


Figure 2-5. Percent depth dose curve for a typical electron beam in water. Shown are the depth of 50% dose R_{50} , the practical range R_p , and depth of dose maximum d_{max} .

AAPM TG-51 uses R_{50} as a beam quality specifier for electron beams. The protocol also supplies an equation based on Monte Carlo simulations that converts I_{50} , the depth on the gradient-corrected ionization curve where the ionization is 50% of the maximum, to R_{50} :

$$R_{50} = \begin{cases} 1.029I_{50} - 0.06 \text{ (cm)} & \text{(for } 2 \leq I_{50} \leq 10 \text{ cm)} \\ 1.059I_{50} - 0.37 \text{ (cm)} & \text{(for } I_{50} > 10 \text{ cm)} \end{cases} \quad (2.57)$$

In order to specify a beam based on a depth dose distribution, measurements of the curve along the central axis of the beam must be taken. This can be challenging, and it is usually performed in a water phantom with a diode detector or an ionization chamber, which of course needs to be water-proof. A diode detector is convenient for such a measurement as the mass collision stopping power ratio of diode material (e.g. silicon) to water is close to unity over the different depths in the phantom. This means that the

detector can be considered energy independent, and the percent ionization curve measured with the diode detector need not be corrected in order to convert to a percent dose distribution curve. Ionization chambers, however, do show energy dependence due to the variability of mass collisional stopping power ratios water-to-air over a range of electron beam energies. In order to obtain the percent dose distribution curve, the percent ionization curve must thus be corrected for this variability in stopping power ratio.

2.6.3 Calibration of Photon Beams

In order to perform clinical reference dosimetry for photon beams, a cylindrical chamber must be used that has been calibrated in a reference beam at a national standards laboratory, with a calibration coefficient assigned. The beam must be open and the point of measurement in the chamber must be positioned at a depth of 10 cm in a water phantom on the beam central axis, with a field size of $10 \times 10 \text{ cm}^2$ at the surface (for a SSD setup) or at the detector depth (for a SAD setup), as shown in Fig. 2-6.

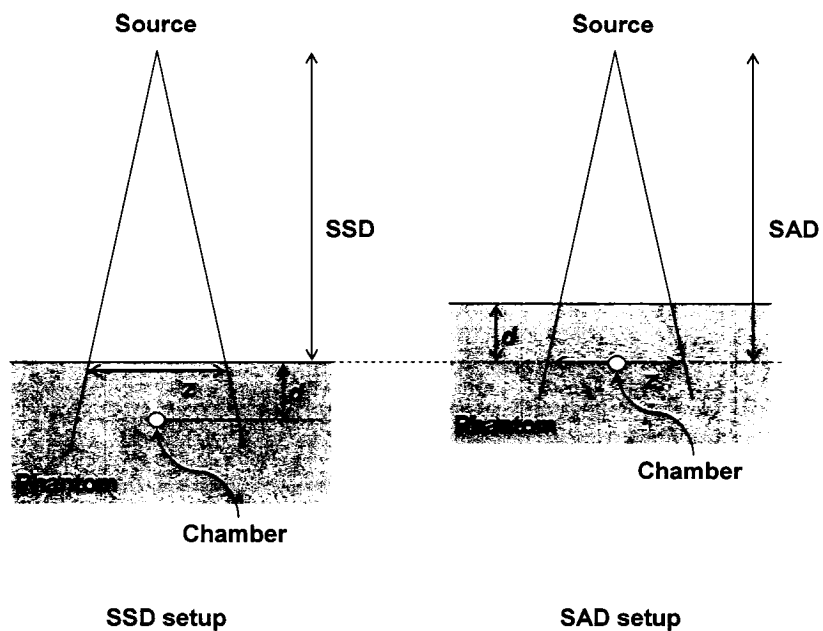


Figure 2-6. Source-to-surface distance (SSD) and source-to-axis distance (SAD) setups used for photon beam dosimetry. The chamber is at a depth d and the field size is z . Measurements in cm.

Cobalt beams may also be calibrated at the traditional reference depth of 5 cm in water. SSD and SAD are the distances normally used clinically, generally 100 cm. k_Q is determined from the protocols as a function of beam quality specification and chamber type. Thus the beam quality must first be determined by $\%dd(10)_x$ (if using TG-51) or TPR_{10}^{20} (if using TRS-398). A charge is measured and fully corrected for influence quantities. The corrected charge, beam quality conversion factor, and calibration coefficient may then be used in equation (2.46) to give the absorbed dose to water.

2.6.4 Calibration of Electron Beams

In order to perform clinical reference dosimetry for electron beams, a protocol must be chosen and its guidelines must be followed. The two most common protocols are shown in table 2-1. Determination of the absorbed dose to water in IAEA TRS-398 is given by equation (2.55), and values for k_Q are listed in the protocol as a function of beam quality R_{50} and common chambers.

QUANTITY	IAEA TRS-398 GUIDELINES	AAPM TG-51 GUIDELINES
Chamber	$R_{50} < 4$ cm : parallel-plate (PP) $R_{50} \geq 4$ cm : cylindrical or PP	$R_{50} \leq 2.6$ cm : PP $R_{50} \leq 4.3$ cm : PP preferred $R_{50} > 4$ cm : cylindrical or PP
Phantom Material	$R_{50} < 4$ cm : water or equivalent plastic $R_{50} \geq 4$ cm : water	Water
Depth of measurement [cm]	$d_{ref} = 0.6 R_{50} - 0.1$ cm	$d_{ref} = 0.6 R_{50} - 0.1$ cm
Position of chamber reference point	PP: inner surface of front window at d_{ref} Cylindrical: center of cavity at $d_{ref} + 0.5r_{cav}$	PP: inner surface of front window at d_{ref} Cylindrical: center of cavity at d_{ref}
SSD (cm)	100	90-110
Field size at surface [cm ²]	10×10, or the size used for normalization of output factors, whichever is larger	$R_{50} \leq 8.5$ cm : $z \geq 10 \times 10$ $R_{50} > 8.5$ cm : $z \geq 20 \times 20$

Table 1-1. Guidelines for electron beam calibration for absorbed-dose-to-water-based protocols AAPM TG-51⁹ and IAEA TRS-398.⁸

AAPM TG-51, however, separates the beam quality conversion factor into two components for electron beams:

$$k_Q = P_{gr}^Q k_{R_{50}}. \quad (2.58)$$

P_{gr}^Q is called the gradient correction factor and it corrects for a shift in point of measurement. The shift is produced by the fact that the chamber cavity, which is filled with air, is inserted into a lower density phantom. The electron fluence is different in air than in the surrounding medium, where the point of measurement is at a different depth than the centre of the ionization chamber (P_{gr}^Q is necessary only for cylindrical chambers; it is unity for parallel-plate chambers). This correction is dependent on the radius of the cavity, r_{cav} , and must be measured by the user. It is done by taking the ratio of readings with the central axis of the chamber at both d_{ref} and $d_{ref} + 0.5r_{cav}$:

$$P_{gr}^Q = \frac{M_{raw}(d_{ref} + 0.5r_{cav})}{M_{raw}(d_{ref})}. \quad (2.59)$$

$k_{R_{50}}$ accounts for differences in beam quality that are not related to gradient effects. This factor is also separated into two components:

$$k_{R_{50}} = k'_{R_{50}} k_{ecal}. \quad (2.60)$$

The component k_{ecal} is the photon-electron beam quality conversion factor that accounts for differences between the reference beam (usually ^{60}Co) and an electron beam of quality Q_{ecal} , converting $N_{D,w}^{Q_0}$ to $N_{D,w}^{Q_{ecal}}$. The electron beam quality conversion factor $k'_{R_{50}}$ further takes into account differences between Q_{ecal} and the electron beam quality of interest, Q , converting $N_{D,w}^{Q_{ecal}}$ to $N_{D,w}^Q$. k_{ecal} is chamber dependent, and values for it are

provided in TG-51 for various chambers. TG-51 also arbitrarily assigns Q_{ecal} to be an electron beam with a beam quality specification of $R_{50} = 7.5$ cm. $k'_{R_{50}}$ depends on the electron beam quality of interest, and its value may be determined using equations and graphs given in TG-51.⁹ The absorbed dose to water is thus

$$D_w^Q = M^Q P_{gr}^Q k'_{R_{50}} k_{ecal} N_{D,w}^{Q_0}. \quad (2.61)$$

According to the protocols, parallel-plate chambers may be used for calibration of lower energy electron beams, provided that the chambers have been calibrated in a ^{60}Co beam. However, calibration coefficients for most parallel-plate chambers are not well established due to inconsistencies in certain correction factors. For this reason, it is recommended that all parallel-plate chambers should be cross-calibrated against a cylindrical chamber in a high-energy electron beam, thereby eliminating the need to explicitly obtain a reference beam absorbed-dose calibration coefficient for the parallel-plate chamber. This is done similarly in TG-51 and TRS-398. To illustrate, however, it is performed in TG-51 by first determining the electron beam quality and the reference depth. Then measurements are made with both chambers, their respective points of measurement at the reference depth. The product of $k_{ecal} N_{D,w}^{Q_0}$ for the parallel-plate chamber is then determined to be:

$$\begin{aligned} (k_{ecal} N_{D,w}^{Q_0})^{pp} &= \frac{(D_w)^{cyl}}{(Mk'_{R_{50}})^{pp}} \\ &= \frac{(MP_{gr}^Q k'_{R_{50}} k_{ecal} N_{D,w}^{Q_0})^{cyl}}{(Mk'_{R_{50}})^{pp}}, \end{aligned} \quad (2.62)$$

where “cyl” and “pp” denote quantities related to the cylindrical and parallel-plate chambers, respectively. The product is then used in equation (2.61) to determine the absorbed dose to water.

2.7 Complexities of Non-equilibrium Dosimetry

The following sections illustrate common areas of radiation dosimetry where charged particle equilibrium does not fully exist: the build-up region of depth dose

curves, penumbra or field edges, and in regions where fields overlap (common in intensity modulated radiation therapy).

2.7.1 Build-up Region

A common example of CPE is shown in the following figures. Collisional kerma and absorbed dose are shown in Figs. 2-7 and 2-8 as a function of depth in a phantom that is irradiated with a beam of photons. Figure 2-7 is hypothetical, in that it does not take into account the effects of attenuation or scattering of the photon.

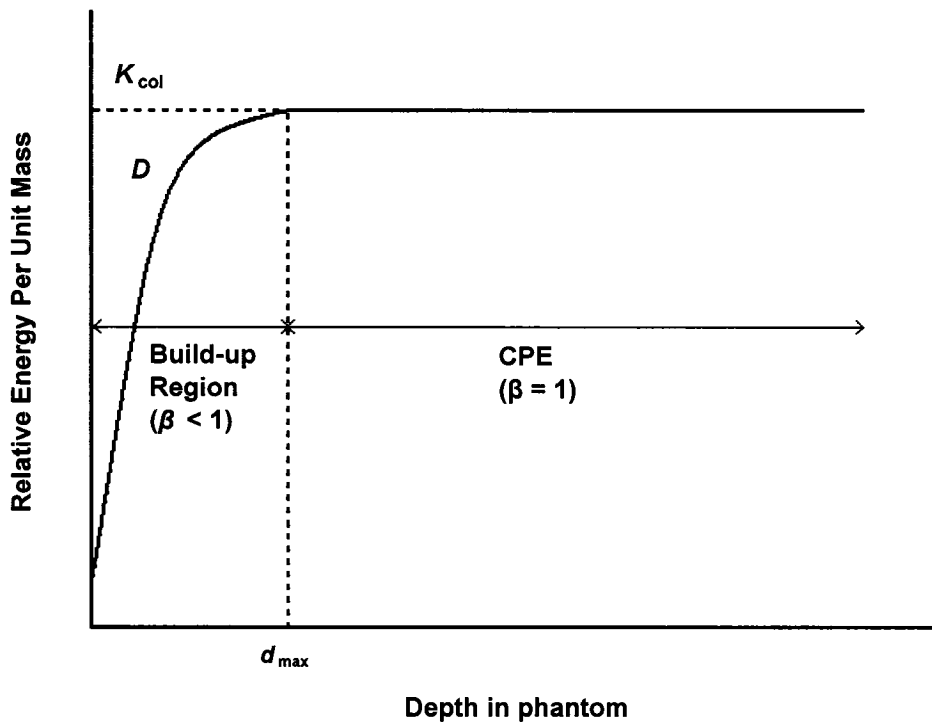


Figure 2-7. Graph of collisional kerma and absorbed dose as a function of depth in a phantom irradiated with a high-energy photon beam, where photon beam is not attenuated or scattered.

This lack of attenuation means that a photon may interact with the matter and produce a secondary charged particle, yet the photon experiences no loss and may continue to produce similar charge particles at further depths. Thus the kerma at each depth is the same. The secondary charged particles, however, travel a certain distance downstream and deposit their energy at a different depth. The build-up region is present because there

are fewer charged particles present before the phantom surface that can add to the absorbed dose. As the depth increases, more charged particles produced in the phantom are available to deposit energy and contribute to the absorbed dose.

Eventually, the range of these secondary charged particles is reached, and the amount of absorbed dose reaches a maximum. CPE exists from this point on, and kerma and absorbed dose are the same. This is because the number of charge particles leaving a volume is always replaced with the same amount entering from upstream.

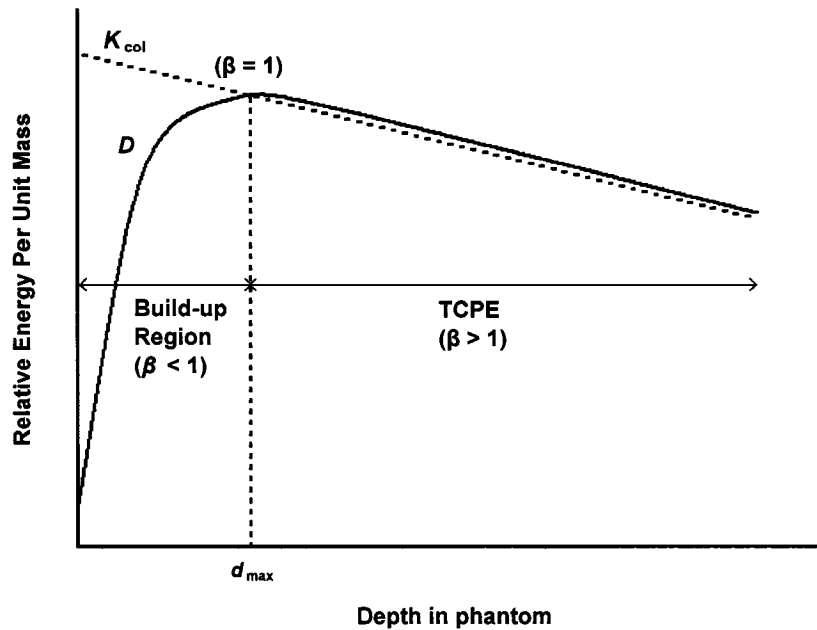


Figure 2-8. Graph of collisional kerma and absorbed dose as a function of depth in a phantom irradiated with a high-energy photon beam, where photon beam is attenuated and scattered.

Figure 2-8 restores the effects of attenuation and scattering of the photon beam, which decreases the photon fluence as it travels through the phantom. Due to this, the collisional kerma begins at a maximum and decreases with depth. A build-up region is again present in the absorbed dose curve for the same reasons as before, and $\beta < 1$. As a reminder, β is defined as the ratio of absorbed dose, D , to collisional kerma, K_{col} . However, CPE only exists at the depth of maximum dose and $\beta = 1$, beyond which the

absorbed dose curve is shifted slightly downstream. This shift is due to fact that the charged particles that are produced in the slowing down process carry their energy a small distance downstream before depositing their energy. However, the absorbed dose decreases with depth after d_{\max} at the same rate as the kerma. In this region, transient charged particle equilibrium (TCPE) exists because the relationship between kerma and absorbed dose is constant ($\beta > 1$).

2.7.2 Penumbra

The size of a radiation field is expressed with specific dimensions, such as $10 \times 10 \text{ cm}^2$, but the dose distribution at different depths in a phantom can be quite complex. Usually, the geometric field size is defined as the width of the profile at the 50% dose level point. Past this width (and apparently outside the geometrically-defined light field), the dose profile is not zero. The dose measured in this region (called the penumbra) is due to three components. The first is *geometric penumbra*,¹ and is shown in Fig. 2-9. The radiation beam focal spot is of finite size due to an electron beam of non-zero width that strikes the target in the linac head. Due to this finite source size, the side regions (regions 2 and 3 in the figure) of each depth in the phantom are exposed to only part of the source, and that part gets smaller as the distance from the central axis is increased. The dose due to geometric penumbra thus decreases with increasing distance from the central axis.

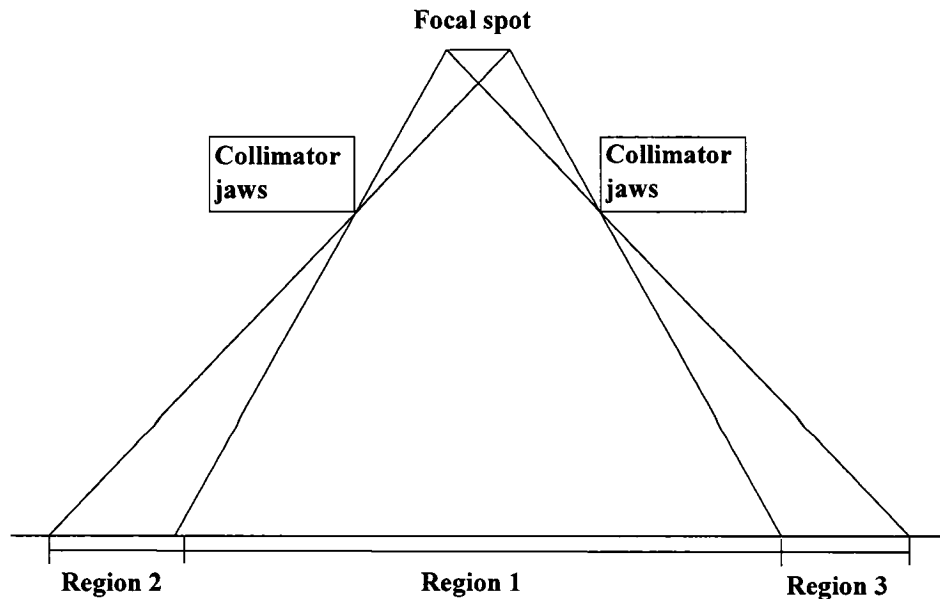


Figure 2-9. Geometric penumbra due to finite size of focal spot. Points in region 1 see the entire focal spot, while points in regions 2 and 3 see only a portion of the focal spot.

The second component is *transmission penumbra*.³ In this component, the linac collimator jaws define the radiation field size but photons can still pass through a portion of the jaws and contribute to the dose outside of the field. The third component is called *scatter penumbra*.³ Photons may scatter from inside the field and create charged particles that deposit dose outside. Also, secondary charged particles from inside the field may travel the length of their range outside of the field, contributing to the dose. Past the penumbra, beam profiles show a low amount of absorbed dose. This region is called the umbra and the dose is due to the low amounts of radiation that do escape through the collimator and linac head shielding.

The lack of CPE in the penumbral region (i.e. lateral charged particle disequilibrium) can be more easily understood if the assumption is made that the focal spot is considered to be a point source, i.e. that it has no finite size. In this case, there is no geometric penumbra and the edges of the photon beam field are sharp. The resulting kerma distribution is constant anywhere within the field and zero outside, as shown in

Fig. 2-10. Secondary charged particles, however, are produced by the photons interacting with phantom material, and although they generally travel in a downstream direction, some scatter sideways and deposit their energy outside of the photon beam field. A scatter penumbra on the absorbed dose curve (also shown in Fig. 2-10) is the result, since at the field edge there are no secondary particles from outside the field that could be scattered. Kerma and absorbed dose are not the same, and CPE is thus not present.

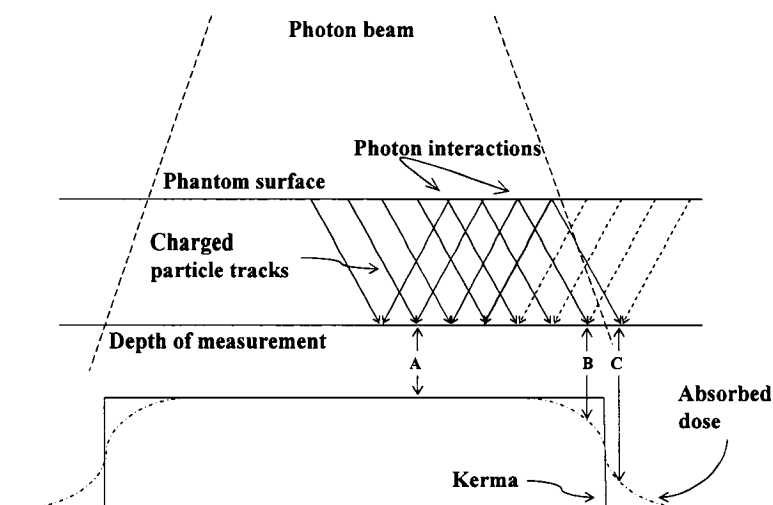


Figure 2-10. Lateral charged particle disequilibrium. Scatter from both sides contributes to maximum absorbed dose at point A, and CPE is present. Inside the beam but close to the edge, point B receives fewer charged particle tracks than point A, and thus has a lower absorbed dose. Outside the beam, point C receives dose due to charged particles scattered from inside the field only. The kerma distribution is sharp due to a photon beam with an infinitesimal source, thus no CPE is present at the field edge and in the penumbra.

2.7.3 IMRT and Overlapping Fields

Multileaf collimators are often used in linear accelerators to produce irregular-shaped radiation fields. These collimators are comprised of 20 to 60 pairs of leaves that can be formed to create a wide variety of field shapes, helping to better conform the dose distribution. These fields have uniform intensity. In order to conform even closer, a number of these irregular sub-fields can be used in what is called intensity modulated radiation therapy (IMRT).³ *Intensity modulation* in this case refers to the beam intensity

that changes with each field used. Two difficulties concerning charged particle equilibrium arise with IMRT. The first is that IMRT subfields may be quite small, and these fields' output factors are not defined due to lack of lateral charged particle equilibrium. A second problem arises due to the fact that sub-fields overlap each other. In principle, this should actually help in overcoming lateral charged particle equilibrium. To understand this, it is clear that one sub-field will have a penumbra due to lack of charged particles contributing from outside the radiation field, as shown in Fig. 2-10. If more fields overlap one another, these charged particles are now present to contribute to the dose at the field edge, and thus the penumbra disappears and the dose does not fall off within the region of treatment. In reality, however, IMRT fields still exhibit lack of CPE at overlap despite these compensating fields due to imperfect field shaping and MLC "tongue and groove" effects (where underdosage occurs because either a leaf tongue or groove, or both, always covers the region between two leaves).¹⁰

References

- ¹ Johns, H. E. and Cunningham, J. R., *The Physics of Radiology*, 4th ed. (Thomas, Springfield, Ill., 1983).
- ² Berger, M. J., Hubbell, J. H., Seltzer, S.M. *et al.* (2005), *XCOM: Photon Cross Sections Database*, [Online] Available: <http://physics.nist.gov/Xcom> [May 1, 2006].
- ³ Podgorsak, E. B., *Radiation Oncology Physics: A Handbook for Teachers and Students*. (International Atomic Energy Agency, Vienna, 2005).
- ⁴ ICRU, "Stopping powers for electrons and positrons," Report No. 37, International Commission on Radiation Units and Measurements (Bethesda, Md., U.S.A., 1984).
- ⁵ Spencer, L. V. and Attix, F. H., "A theory of cavity ionization," *Radiat. Res.* **3** (3), 239-254 (1955).
- ⁶ Nahum, A. E., "Water/air mass stopping power ratios for megavoltage photon and electron beams," *Phys. Med. Biol.* **23** (1), 24-38 (1978).
- ⁷ AAPM, TG-21, "A protocol for the determination of absorbed dose from high-energy photon and electron beams," *Med. Phys.* **10** (6), 741-771 (1983).

- ⁸ IAEA, "Absorbed Dose Determination in External Beam Radiotherapy : An International Code of Practice for Dosimetry Based on Standards of Absorbed Dose to Water," Report No. 398, International Atomic Energy Agency (Vienna, 2000).
- ⁹ Almond, P. R., Biggs, P. J., Coursey, B. M. *et al.*, "AAPM's TG-51 protocol for clinical reference dosimetry of high-energy photon and electron beams," *Med. Phys.* **26** (9), 1847-1870 (1999).
- ¹⁰ Deng, J., Pawlicki, T., Chen, Y. *et al.*, "The MLC tongue-and-groove effect on IMRT dose distributions," *Phys. Med. Biol.* **46**, 1039-1060 (2001).

Chapter 3

Standard Air Ionization Chambers

3.1 Introduction

Air ionization chambers are most often used for measuring absorbed dose. The most common types are parallel-plate and cylindrical (or “thimble”) chambers. They are both designed with three types of electrodes necessary for defining the sensitive volume where the number of ions that are produced will be measured. The polarizing electrode is connected to the power supply and is parallel to the collecting electrode. An electric field is produced across the gap between the polarizing and collecting electrode. The collecting electrode is also connected to an electrometer, which can measure the charge that is produced in the sensitive volume and then deposited on it. The guard electrode is at the same potential as the collecting electrode and is necessary so that the edges of the sensitive volume are well defined and so that unwanted chamber leakage currents are excluded from the measurement.

A typical parallel-plate ionization chamber is shown in Fig. 3-1, so called because the polarizing and collecting electrodes are parallel on opposing sides of the sensitive volume. These chambers are most often used for calibration of superficial photon beams, lower-energy electron beams and for measuring surface dose and build up-regions in high-energy photon beams. They are used for the latter because the flat design and point of measurement allow for positioning close to the surface in a water phantom. A typical cylindrical chamber is shown in Fig 3-2. These are more common, and are used to calibrate electron beams above 10 MeV, orthovoltage x-ray beams and high energy photon beams.

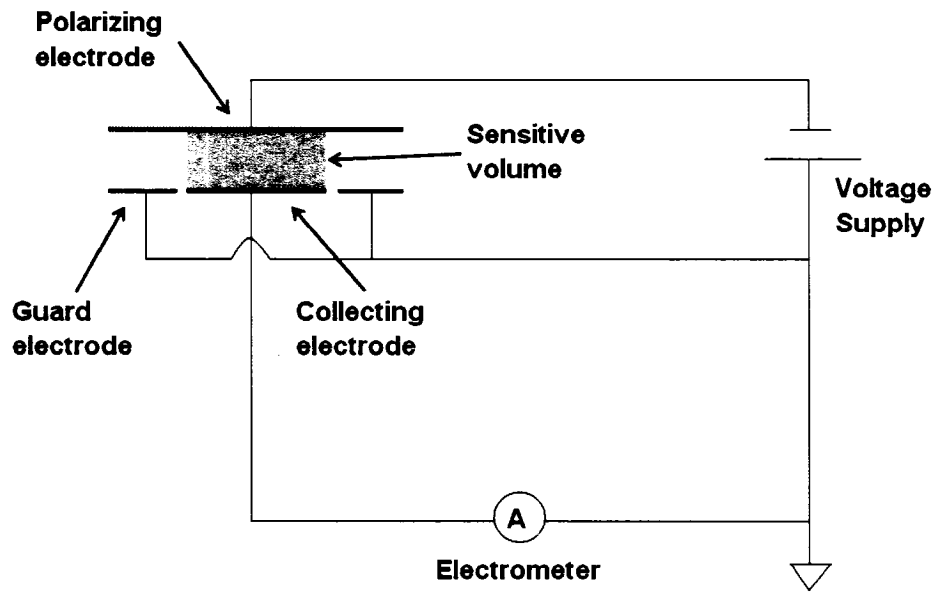


Figure 3-1. Schematic diagram of the inner circuitry for a parallel-plate ionization chamber.

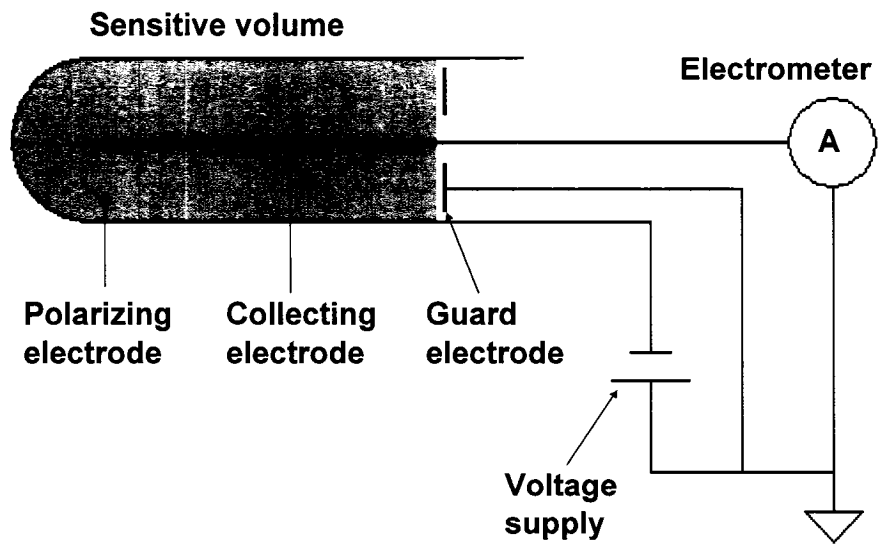


Figure 3-2. Schematic diagram of the inner circuitry for a cylindrical ionization chamber.

3.2 Correction Factors for Air Chambers

An air ionization chamber produces a signal that is converted to dose through calibration coefficients. Additional factors must be taken into account as well in order to correct for influence quantities such as the physical properties of air, chamber polarity effects, ion recombination effects, leakage effects, and stem effects. During measurement, these properties can be different than when reference measurements were made, and thus must be corrected.

3.2.1 Temperature, Pressure, and Humidity Effects

Air ionization chambers use air as the medium in the sensitive volume, but the air is not generally sealed inside. The air is open to the atmosphere and thus its physical properties such as temperature, pressure, and humidity are affected by outside conditions. A low density gas such as air can be characterized by the ideal gas law,¹ which includes many of the gas' properties:

$$PV = nRT . \tag{3.1}$$

In this equation, P is the gas pressure, V is the volume, n is the number of moles of gas, R is a constant, and T is the temperature. Isolating the number of moles, we have:

$$n = \frac{PV}{RT} , \tag{3.2}$$

and we see that when the volume remains constant, the number of moles is proportional to the gas pressure and inversely proportional to the gas temperature. The chamber reading depends on the number of molecules of air in the chamber, so we see that a higher air pressure will increase the chamber signal and a higher air temperature will decrease the chamber signal.

Calibrations of air chambers in standards laboratories are related to defined reference conditions, and clinical measurements are then corrected to these references.

Reference conditions (denoted by a subscript $_0$) are $T_0 = 22^\circ\text{C}$ (only in North America; Europe uses 20°C) and $P_0 = 101.325 \text{ kPa}$. Thus the factor used to correct the effects of atmospheric pressure P and temperature T on air is:²

$$P_{T,P} = \frac{P_0}{P} \frac{T}{T_0} = \frac{101.33}{P} \frac{(273.2 + T)}{295.2}, \quad (3.3)$$

where the temperature is expressed in degrees Celsius.

Relative humidity effects are negligible between 10% and 70% so this correction factor is generally not included.³

3.2.2 Polarity Effects

A reading of an ionization chamber may be affected differently for opposite polarizations under the same irradiation conditions. This polarity effect can be corrected for by taking readings at positive and negative chamber polarities, M_+ and M_- , respectively. These readings are used to determine the correction factor, which, when multiplied by the reading taken at the polarity M that is normally used for measurements (either M_+ or M_-), will give the mean of the absolute values of the readings:²

$$P_{\text{pol}} = \left| \frac{M_+ - M_-}{2M} \right|. \quad (3.4)$$

The polarity effect is almost negligible for depths greater than the depth of maximum dose in a phantom irradiated with megavoltage photon beams. For electron beams and in the build up region of photon beams, however, this effect can be considerable. It has been shown that this effect is dependent on the dimensions of the electrodes and orientation in the beam.⁴

3.2.3 Recombination Effects

When an ion chamber is irradiated, ions are produced in the sensitive volume. The charge from these ions is measured by the collecting electrode, and the absorbed dose is determined based on this reading. Because the electrodes on opposite ends of the sensitive volume are oppositely polarized, each attracts ions of opposite charge. During collection, positive and negative ions may recombine with each other and not be collected. This means the reading does not adequately describe how many ions were produced and corrections for ion recombination must be made. There are two main mechanisms of recombination: initial recombination, where ions produced along the same electron track recombine, and general recombination, where ions produced along different electron tracks recombine once the initial track structure has been destroyed.⁵ A third mechanism is also included in the recombination correction, called ionic diffusion, where ions of a specific sign diffuse against the electric field and are collected by the wrong electrode. Diffusion is included in this correction because it plays a part in the loss of correct ion collection as do the mechanisms of recombination.

Recombination is dependent on the applied electric field. As the electric field increases, fewer ions are allowed to recombine. The relationship between applied voltage and ionization current is shown in Fig. 3-3 and is called a saturation curve. The current increases with increasing voltage and eventually the voltage is high enough to allow very little recombination to occur, and saturation occurs. As the voltage continues to increase, more energy is being given to the produced electrons, which are then able to ionize other atoms. Charge multiplication then takes place and the signal obtained is no longer related to the dose delivered to the point.

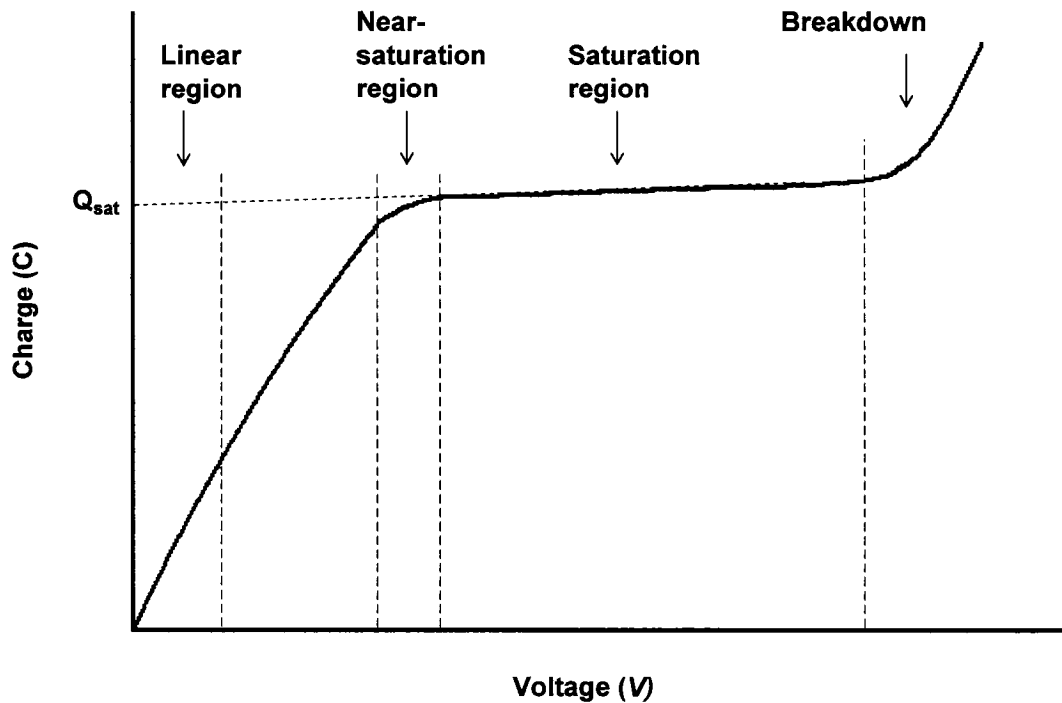


Figure 3-3. Air ionization chamber saturation curve. As low applied potential increases, fewer ions recombine and the signal increases. Eventually most produced ions are collected and the saturation region is reached.

There are three categories of radiation beams into which effects of recombination can be placed. These are: continuous radiation beams such as isotope beams and orthovoltage x-ray beams, pulsed radiation beams such as linear accelerator photon and electron beams, and scanned pulsed beams such as scanned linear accelerator beams. These categories exist because recombination is accounted for differently in each.

3.2.3.1 Initial Recombination

Because initial recombination occurs between ions produced along the same electron track, it is independent of the number of tracks produced in the sensitive volume. Thus it is independent of the dose rate. It does, however, depend upon the density of atoms that lie in the path of the electron as well as the field strength. In Fig. 3-3 we see

the effects of initial recombination in the linear region at low electric fields. As the electric field increases, fewer positive and negative ions are allowed to recombine and the current increases. Response from gas-filled ionization chambers exhibits little initial recombination due to the low density, and this effect is generally negligible at electric fields used in clinical ion chambers. It does become important, however, when discussing recombination effects in liquid-filled ionization chambers, due to the high ionization density.⁶ In this case, as we shall see in a later section on recombination in liquids, saturation is never actually achieved due to initial recombination.

3.2.3.2 General Recombination

In air chambers, general recombination is the largest contributor to the difference between measured charge and produced charge. Because it occurs between ions of opposite signs produced along different electron tracks, general recombination is dependent on dose rate, i.e. the number of ionizing particle tracks per unit time in the volume. It has been well described in both continuous and pulsed radiation beams.

Continuous Radiation Beams

General recombination in continuous radiation beams, such as those produced by radioactive isotopes, has been described in terms of the collection efficiency of an ionization chamber. Collection efficiency (f) is defined as the ratio of the charge collected (Q') to the charged produced (Q) in the sensitive volume during irradiation. The charge produced is, of course, not initially known, but the efficiency can also be written as:

$$f = \frac{1}{1 + \xi^2}, \quad (3.5)$$

where ξ is determined for parallel-plate chambers in continuous beams to be:

$$\xi^2 = \left(\frac{\alpha}{6ek_1k_2} \right) \left(\frac{d^4q}{U^2} \right) = \frac{1}{m^2} \left(\frac{d^4q}{U^2} \right) \quad (3.6)$$

where:

$$m = \sqrt{\frac{6ek_1k_2}{\alpha}} \quad (3.7)$$

In these equations, α [$\text{m}^3 \cdot \text{s}^{-1}$] is the recombination rate constant, k_1 and k_2 [$\text{m} \cdot \text{V}^{-1} \cdot \text{s}^{-1}$] are the positive and negative ion mobilities, respectively, $e = 1.602 \times 10^{-19}$ C is the charge of an electron, d [cm] is the plate separation, U [V] is the applied potential, and $m = 1.219 \times 10^{-7} (\text{m} \cdot \text{C})^{1/2} \cdot \text{V}^{-1} \cdot \text{s}^{-1/2}$ is a gas constant for air. $q = \frac{Q}{Vt}$ is the charge Q [C] liberated in the volume V [m^3] per unit time t [s].

J. W. Boag presented a formerly-used empirical procedure that described a relationship between the reciprocal of the measured ionization current i and the field strength X between the plates, where general recombination was dominant:⁵

$$\frac{1}{i} = \frac{1}{i_0} + \frac{\text{constant}}{X^2} \quad (3.8)$$

To obtain this relationship, we can combine equations 3.5, 3.6 and 3.7, and rewrite them as

$$f = \frac{Q'}{Q} = \frac{m^2 U^2}{m^2 U^2 + d^4 q} \quad (3.9)$$

We can change this into the form of equation 3.8 by isolating $\frac{1}{Q'}$:

$$\begin{aligned} \frac{1}{Q'} &= \frac{m^2 U^2 + d^4 q}{m^2 U^2} \frac{1}{Q} \\ &= \frac{1}{Q} + \left(\frac{d^4 q}{m^2 U^2} \right) \frac{1}{Q} \\ &= \frac{1}{Q} + \frac{a}{U^2} \end{aligned} \quad (3.10)$$

where

$$a = \frac{d^4}{m^2 V t}. \quad (3.11)$$

The linear relationship between $\frac{1}{Q'}$ and $\frac{1}{V^2}$ allows for a determination of collection efficiency (and thus a recombination correction) using what is called the *two-voltage technique*. According to AAPM TG-51 protocol,² a raw reading M_{raw}^H is taken at the normal operating voltage V_H . A second reading, M_{raw}^L , is taken at a lower voltage, V_L , under the same conditions of irradiation. The correction for ion recombination is then

$$P_{\text{ion}}(V_H) = \frac{1}{f} = \frac{M_{\text{sat}}}{M_{\text{raw}}^H} = \frac{1 - (V_H/V_L)^2}{M_{\text{raw}}^H / M_{\text{raw}}^L - (V_H/V_L)^2} \quad (3.12)$$

where M_{sat} is the saturation signal reached as V approaches infinity (i.e. the total charge produced in the sensitive volume). IAEA TRS-398 protocol⁷ uses different notation but the procedure is the same.

Pulsed Radiation Beams

The collection efficiency of a chamber irradiated with a pulsed radiation beam is expressed as:

$$f = \frac{1}{u} \ln(1 + u), \quad (3.13)$$

where

$$u = \mu \frac{r}{U} d^2 \quad (3.14)$$

and

$$\mu = \frac{\alpha}{e(k_1 + k_2)}. \quad (3.15)$$

In these equations, r is the amount of charge per unit volume and radiation pulse liberated by radiation and escaping initial recombination, and the other quantities were defined earlier. A linear relationship exists between $\frac{1}{Q'}$ and $\frac{1}{V}$ (rather than $\frac{1}{V^2}$) in the near saturation region for pulsed beams. Thus the two-voltage technique helps us to determine a recombination correction that is similar to the one determined for a continuous beam:

$$P_{\text{ion}}^{\text{pulse}}(V_H) = \frac{1}{f} = \frac{M_{\text{sat}}}{M_{\text{raw}}^H} = \frac{1 - (V_H/V_L)}{M_{\text{raw}}^H / M_{\text{raw}}^L - (V_H/V_L)}. \quad (3.16)$$

This method is used by AAPM TG-51 protocol.

The IAEA TRS-398 protocol also recommends using the two-voltage technique assuming a linear dependence of $\frac{1}{Q'}$ on $\frac{1}{V}$, and also recommends that M_N (equivalent to M^H) and M_L should each be corrected for polarity effects, which change with voltage. However, in this protocol a quadratic polynomial is used to determine the recombination correction factor:

$$k_{\text{sat}}(V_N) = a_0 + a_1 \frac{M_N}{M_L} + a_2 \left\{ \frac{M_N}{M_L} \right\}^2, \quad (3.17)$$

where M_N refers to the reading at normal voltage V_N . a_0 , a_1 , and a_2 are constants that depend on the ratio of voltages used, which is given in a table in the protocol for both pulsed and pulsed-scanned beams. The protocol recommends using a V_N/V_L ratio of at least 3, and to not make V_N too large so that charge multiplication will not add to the signal. After the voltage has been changed, the chamber should be allowed to establish charge equilibrium by pre-irradiating it before measuring.

3.2.3.3 Ionic Diffusion

Under some conditions, ions of one sign that are produced close to the collection electrode with a voltage of the same sign may diffuse to that plate and distribute their charge there. This would contribute to a difference between the charge produced and the charge measured. However, this effect is only significant at low voltages and may be neglected for voltages generally used in radiation dosimetry.⁵

3.2.4 Chamber Leakage Effects

When the chamber is not being irradiated, yet a voltage is applied across the electrodes, a current intrinsic to the chamber will still be measured due to imperfect insulation of the electrodes. In well-built air chambers this signal should be small – more than two orders of magnitude lower than the measured current during irradiation – and thus considered negligible. If it is larger, the leakage charge should be measured for a time equal to the length of irradiation and then subtracted from the irradiation reading.

3.3 Limitations of Standard Chambers

3.3.1 Low Spatial Resolution

Air chambers measure the ionization charge that is produced in the sensitive volume. Molecules in a low density gas are relatively sparse, and so a large sensitive volume is needed in order to generate a large enough signal. Typical cylindrical chambers have a sensitive volume in the range of 0.1 cm³ to 1 cm³. Parallel-plate chambers⁸ typically have a plate separation of 0.1 cm and a sensitive volume of 0.05 to 0.2 cm³. The most common clinically-used cylindrical chambers⁷ have a sensitive volume of 0.6 cm³. The resolution of these large-volume chambers is not sufficient for high gradient regions such as field edges and narrow beam profiles. Air chambers with smaller sensitive volumes are available, such as the PTW PinPoint® chamber (15 mm³) and the Exradin A16 Micropoint cylindrical chamber (7 mm³). The smallest commercially available air ionization chamber is the Exradin A14P parallel-plate microchamber, which has a plate separation of 1 mm and a sensitive volume of about

1.8 mm³. Such a small sensitive volume is ideal for use in measurements of high dose gradients, but the measured ionization signal is also very small.

3.3.2 Chamber Fluence Perturbation

A chamber filled with a gas such as air displaces an amount of the higher density medium, such as water, in which it is placed. Because of the presence of a lower-density gas, there is an electron fluence perturbation which will result in the determination of a dose at the point of measurement that would be different in the medium in the absence of the chamber. This is generally not a problem for photon beams, because where charged particle equilibrium exists, the secondary electron fluence distribution does not change significantly with position. In regions that lack CPE, such as the build-up region or in field edges, effects of perturbation are present.

Perturbation effects can be significant in electron beams, due to lack of electron scatter in the low-density chamber cavity. Thus the effects of *in-scattering* from outside the cavity increase the electron fluence inside, compared to the fluence in that region in the absence of the cavity. This is shown in Fig. 3-4, where the solid lines represent electron tracks and the dashed lines represent missing electron tracks. This effect can be somewhat reduced in parallel-plate chambers by guard rings that are sufficiently large so as not to allow the in-scattered electrons to contribute to the signal.

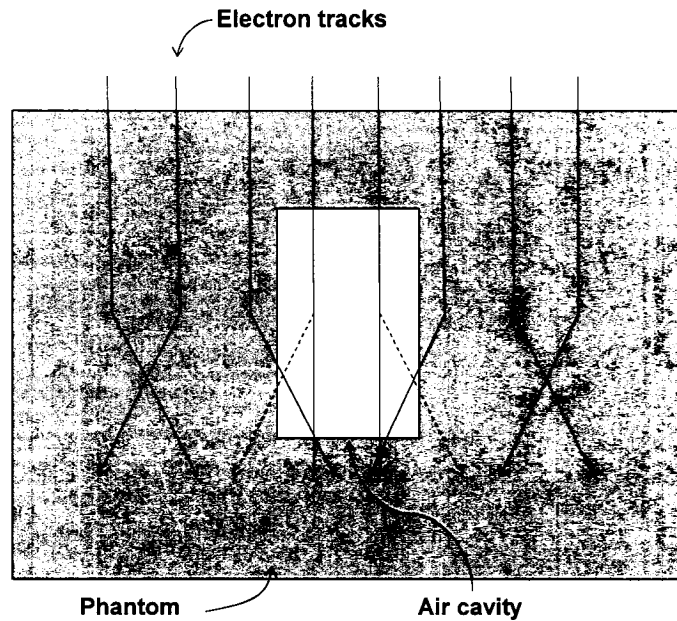


Figure 3-4. Effects of in-scattering on electron distribution in a chamber cavity.

3.3.3 Energy Dependence

As discussed in section 2.4.2, the Spencer-Attix cavity theory relates the absorbed dose in the cavity (e.g. air) to the absorbed dose in the medium (e.g. water) using the ratio of restricted stopping power water-to-air. This ratio depends on the energy of electrons. Fig. 3-5 shows this ratio, which is not constant, over a wide range of electron energies. Because the ratio is not constant, air chamber response is energy dependent. This can cause problems for regions of dose distribution that have a high energy gradient, such as field edges. The ratio is also included in the beam quality conversion factor, k_Q , so response to beam qualities compared to a reference beam can greatly vary. Thus air chambers have large energy dependence (and therefore various k_Q factors) over the range of clinical beam energies.

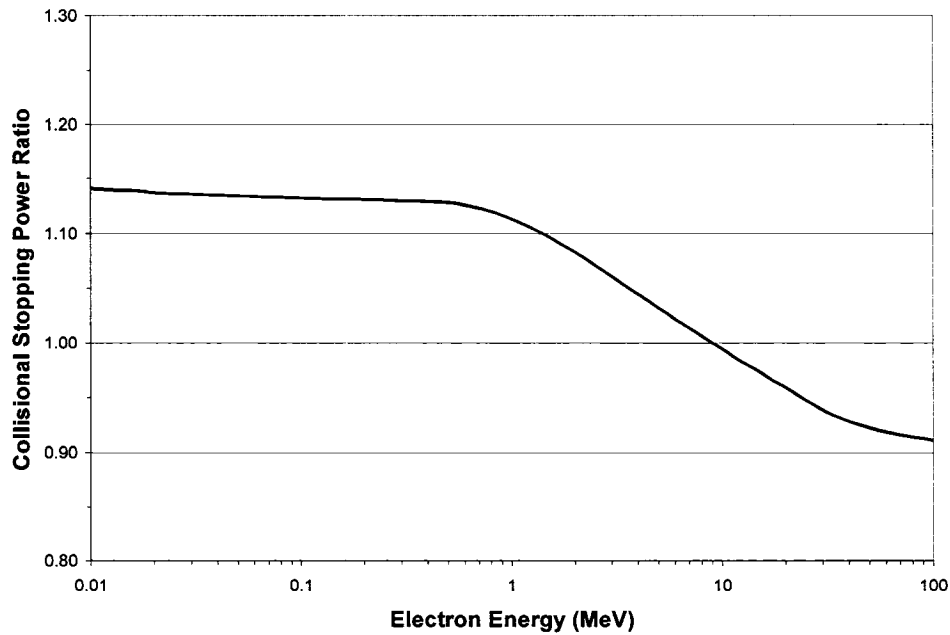


Figure 3-5. Ratio of restricted mass stopping power water-to-air as a function of electron kinetic energy. The ratio is not constant over the clinical range of electron energies, thus air chambers are energy dependent.⁹

References

- ¹ Schroeder, D. V., *An introduction to thermal physics*. (Addison Wesley, San Francisco, CA, 1999).
- ² Almond, P. R., Biggs, P. J., Coursey, B. M. *et al.*, "AAPM's TG-51 protocol for clinical reference dosimetry of high-energy photon and electron beams," *Med. Phys.* **26** (9), 1847-1870 (1999).
- ³ Rogers, D. W. and Ross, C. K., "The role of humidity and other correction factors in the AAPM TG-21 dosimetry protocol," *Med. Phys.* **15** (1), 40-48 (1988).
- ⁴ Gerbi, B. J. and Khan, F. M., "The polarity effect for commercially available plane-parallel ionization chambers," *Med. Phys.* **14** (2), 210-215 (1987).
- ⁵ Boag, J. W., "Ionization Chambers" in *The Dosimetry of Ionizing Radiation*, Vol. II, edited by K. R. Kase, B. E. Bjärngard, and F. H. Attix (Academic Press, San Diego, 1987), pp. 169-233.
- ⁶ Attix, F. H., *Introduction to radiological physics and radiation dosimetry*. (Wiley, New York, 1986).

- ⁷ IAEA, "Absorbed Dose Determination in External Beam Radiotherapy : An International Code of Practice for Dosimetry Based on Standards of Absorbed Dose to Water," Report No. 398, International Atomic Energy Agency (Vienna, 2000).
- ⁸ Podgorsak, E. B., *Radiation Oncology Physics: A Handbook for Teachers and Students*. (International Atomic Energy Agency, Vienna, 2005).
- ⁹ Berger, M.J., Coursey, J.S., Zucker, M.A. *et al.* (2005), *Stopping-Power and Range Tables for Electrons, Protons, and Helium Ions*, [Online] Available: <http://physics.nist.gov/Star> [May 1, 2006].

Chapter 4

Liquid Ionization Chambers and Their History

4.1 Advantages of Liquid Ionization Chambers

The issues discussed in section 3.3 concerned the limitations of air ionization chambers in radiation dosimetry. Section 2.6.1 discussed the complexities of non-equilibrium dosimetry. The use of a dielectric liquid as the sensitive material inside an ionization chamber has been investigated as a potential remedy for these problems. Two liquids commonly used in liquid ionization chambers (LICs) are isooctane (also called 2,2,4-Trimethylpentane, or TMP) and tetramethylsilane (TMS). There are number of properties that make these two liquids suitable for such use: insulation, ion yield, density, atomic number, stopping power, and ion mobility. In addition, the radiation response of such liquids should be stable and reproducible.

4.1.1 Insulation

Both isooctane and tetramethylsilane are insulating nonpolar hydrocarbons. Their chemical structure is shown in Fig. 4-1. Their inherent insulation is important because they exhibit a low inherent leakage current when used at the sensitive media in liquid ionization chambers.

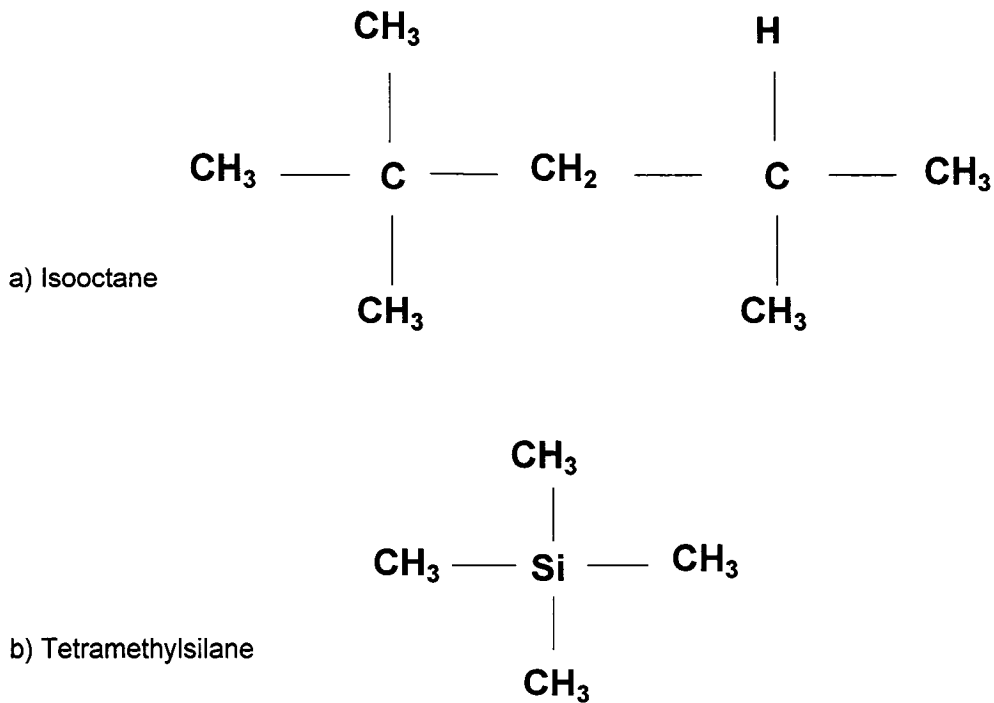


Figure 4-1. Chemical structure of Isooctane and tetramethylsilane molecules.

4.1.2 Free-ion Yield

When a material is irradiated, energy is expended in the production of ions. In section 2.3.4, it was explained that the average amount of energy required in order to produce an ion pair in dry air was expressed as $\left(\frac{\bar{W}_{air}}{e}\right)$. An analogous expression used here is called the G-value, or the free-ion yield G_{fi} . This is defined as the number of electron-ion pairs created and escaping initial recombination in the liquid (or another ionizing medium) per 100 eV of absorbed energy.¹ However, where $\left(\frac{\bar{W}_{air}}{e}\right)$ is constant, G_{fi} is dependent on temperature, radiation type, and electric field strength. For both isooctane and tetramethylsilane, Wickman showed that G_{fi} varies by only a few percent over high energy photon and electron beam qualities, and that G_{fi} varies by 0.18% per °C for isooctane.² The G_{fi} value is, however, quite dependent on the applied electric field.

In order to determine the property G_{fi}^0 , which is the free-ion yield in the absence of applied electric field, the linear relationship between G_{fi} and high field strength may be extrapolated to zero. G_{fi}^0 varies between 0.1 and 1 for different dielectric liquids. Values of G_{fi}^0 for our liquids of interest are 0.33 for isooctane and 0.74 for tetramethylsilane.³ In order to compare to air, the inversion of equation 2.33 shows that the free ion yield in air is 2.94 ion pairs per 100 eV, which is larger than for the dielectric liquids. Taking into account that isooctane and tetramethylsilane are respectively 535 and 504 times denser than air, the ionization in the liquids is much greater than what is produced in an air cavity of the same size.

4.1.3 Density and Atomic Number

The densities of air, water, TMS, and isooctane are shown in Table 4-1. The densities of these liquids are much more similar to water than air, whose density is three orders of magnitude smaller. For this reason, the cavity perturbation effects explained in section 3.3.2 are greatly reduced, as the amount of scatter is similar inside and outside of the cavity.

	Air	Water	Isooctane	TMS
Density (g/cm³)	1.29×10 ⁻³	1.00 (at 0°C)	0.69	0.65
\bar{Z}	7.78	7.51	5.36	8.85

Table 4-1. Mass densities and effective atomic number, \bar{Z} , of air, water, and two dielectric liquids commonly used in liquid ionization chambers: isooctane and tetramethylsilane (TMS).

In addition to having a density similar to water, we can also see on the table that the effective atomic numbers of isooctane and tetramethylsilane are low, and similar to water. The effective atomic number is calculated according to the equation:⁴

$$\bar{Z} = \sqrt[3.5]{a_1 Z_1^{3.5} + a_2 Z_2^{3.5} + \dots + a_n Z_n^{3.5}}, \quad (4.1)$$

where a_i is the fractional number of electrons per gram belonging to a material with atomic number Z_i . This similarity is an important property attesting to the water equivalence of these liquids, and contributes to their water-similar stopping powers. The significance of these stopping powers is explained in the next section.

4.1.4 Stopping Power Ratios

In section 3.3.3, it was explained that the stopping power ratio water-to-air exhibits significant energy dependence over the range of clinical beam energies, and thus beam quality conversion (or k_Q) factors for air chambers have a large energy dependence. One advantage of using LICs is that the liquid stopping powers and their variance are very similar to those of water. As a result, the ratio of restricted collisional stopping powers liquid-to-air (and thus k_Q) is close to unity over a large range of beam energies, including those used clinically. These ratios are shown in Fig. 4-2, and are compared to the water-to-air ratio as well. This feature of LICs is not only useful for clinical beam quality conversion and reference, but also for large changes in energy exhibited in high dose gradients of complex fields.

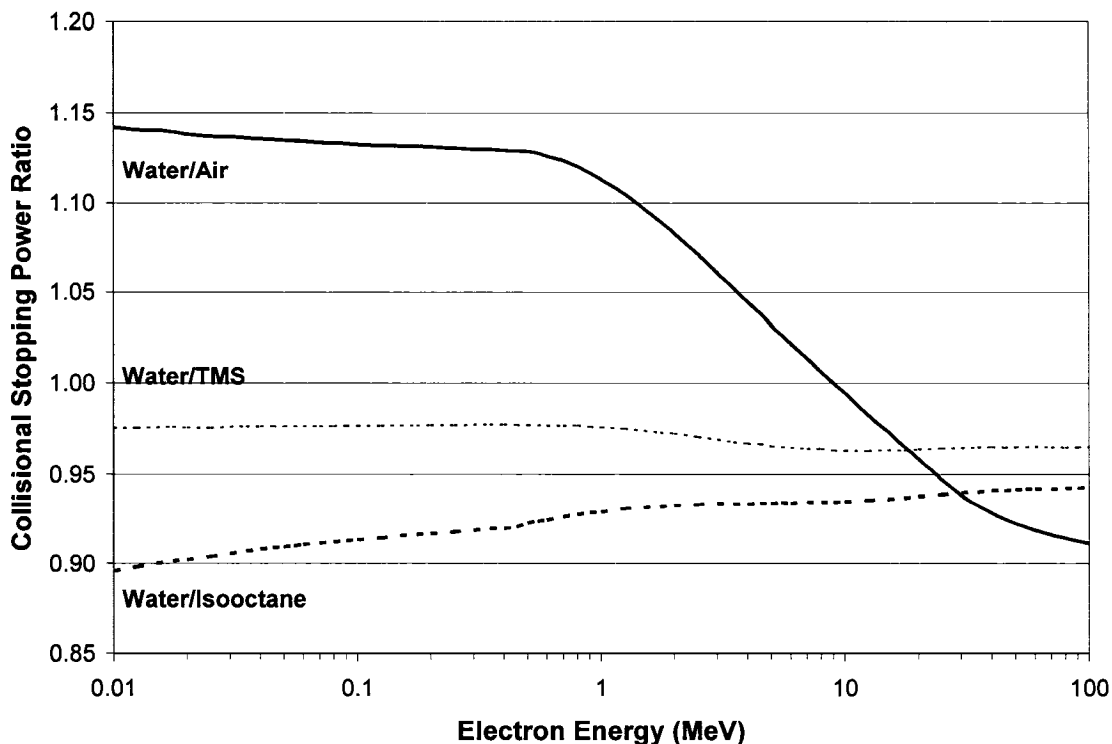


Figure 4-2. Ratio of restricted stopping powers (water-air, water-isooctane, and water-TMS) as a function of electron kinetic energy.⁵ Note the relative lack of energy dependence for the dielectric liquids ratios compared to the air ratio.

4.1.5 Ionization Density and Mobility

As mentioned previously, a main purpose in investigating liquid ionization chambers is the advantage of high spatial resolution. Small sensitive volumes are made possible by the high ionization density of the liquids that are used. The ionization density of these dielectric liquids is about 300 times larger than that of air.² Due to the high density of the liquids compared to air, there is a larger opportunity for ions to recombine with each other before being collected. Because of this, the liquids used must have a high mobility in order to minimize recombination as much as possible. The mobilities of both positive and negative ions produced in isooctane and tetramethylsilane are given in Table 4-2.

	Air	Isooctane	TMS
k_+ ($\text{m}^2\text{s}^{-1}\text{V}^{-1}$)	1.8×10^{-4}	2.9×10^{-8}	5.3×10^{-8}
k_- ($\text{m}^2\text{s}^{-1}\text{V}^{-1}$)	1.8×10^{-4}	2.9×10^{-8}	9.0×10^{-8}

Table 4-2. Mobility of both positive and negative ions (k_+ and k_- , respectively) produced in air, isooctane and tetramethylsilane (TMS).⁶

Despite the high mobilities of ions in these liquids compared to other dielectric liquids, they are still between 2000 and 6000 times smaller than in air. We shall thus see in the following sections that these mobilities are not high enough to overcome the high ionization density present. Consequently, calculations of ion recombination must be determined and correction factors must be applied.

4.2 Modern Research in Liquid Ionization Chambers

Molecules in dielectric liquids were first shown to be ionized upon irradiation by J.J. Thomson in 1896.⁷ Since Thomson's discovery, further investigations of the use of liquid ionization chambers (LICs) were intermittent, such as research by Stahel (1929), Blanc (1963), and Mathieu (1968).⁸ These projects showed that such chambers could be suitable for dosimetry, and would help overcome the problems that came with air-filled chambers. Present interest in liquid ionization chambers was mostly progressed by work that has been done on the subject by G. Wickman et al. in Umeå, Sweden since 1973, when he built and investigated a liquid ionization chamber for possible use in radiation dosimetry.⁹ His goal was to construct a chamber that could be used to determine absorbed dose and dose distributions due to radiation fields as easily as an air ionization system, while also showing some distinct advantages. He tested a variety of designs in order to find a proper combination of materials for the liquid, the insulators, the body, and electrode that would allow acceptable stability, reproducibility, dose sensitivity, and low levels of fluence perturbations and leakage current. Wickman's group has continued to design new models of the LIC, test them in common radiation beams, and publish research they have performed that deal with LIC stability, reproducibility, polarity effects, ion recombination corrections, and response to different dose rates.^{2,6,8-16}

As mentioned in section 3.3.1, air ionization chambers have large volumes (i.e. low spatial resolution) in order to obtain large enough signals. Some manufacturers produce air chambers with small sensitive volumes in order to obtain high spatial resolution. The price for this, of course, is a low signal requiring measurement using high-resolution electrometers. The magnitude of the obtained signal may also be similar to that of the inherent leakage current or radiation-induced cable currents, and be difficult to distinguish. Some work has recently been done in modifying small air chambers and filling them with a dielectric liquid in order to obtain larger signals while utilizing the high spatial resolution. In Italy in 1998, Francescon *et al.*¹⁷ investigated new dosimeters for use in small field radiation beams, where high dose gradient and lack of charged particle equilibrium exist. The detectors included a modified Exradin T14 parallel-plate microchamber. The sensitive volume of this chamber was about 2 mm³, and the group performed output factor measurements using the chamber filled with both air and TMS. They found some advantages of the liquid-filled over the air-filled chamber: the signal from the liquid-filled chamber was enhanced (also making currents due to cable irradiation negligible), and the perturbation effect was decreased. The air-filled chamber produced reliable values of the output factor, but results were better when the chamber was filled with tetramethylsilane. Another group in St. Louis, Missouri¹⁸ filled a modified Exradin A2 air chamber for use as a water-equivalent radiation dosimeter that was independent of beam type and quality. They determined a mixture of ideal concentrations of dielectric liquids, which showed a 2% deviation of response of the dosimeter to dose to water over a beam energy range from 10 keV to 20 MeV.

Other interest had been recently been shown in using liquid-filled chambers for the purpose of monitoring the dose of fields with high gradients. Studies shown in papers published by Eberle *et al.*¹⁹ and Berghofer *et al.*²⁰ demonstrated the use of prototype liquid ionization chambers as a monitor for IMRT. A thin monitor chamber was required in order to absorb a minimum amount of radiation, yet a large enough signal was needed in order to minimize the effects of currents inherent to the system. An air-filled chamber would not be thin enough, so a liquid chamber was used instead. In the dynamic IMRT system, the high leaf speed required a fast readout frequency of the monitor, so a liquid with a high charge yield and high carrier mobility was needed. TMS was used, as it

fulfilled these requirements. The chamber was able to actually monitor instantaneous radiation measurements and changing beam shape due to moving leaves. One disadvantage, however, was the dose rate dependence of the liquids, for which a correction factor had to be applied.

4.3 Research in Liquid Ionization Chambers at McGill University

Investigations of a liquid chamber developed by Wickman, a liquid-filled modified air chamber, and liquid chambers of original design have been performed in the Medical Physics Unit of McGill University prior to the work presented in this thesis.²¹

A liquid chamber developed by Wickman, the LIC 9902-mix, used as a sensitive volume material a mixture of 60% isooctane and 40% tetramethylsilane by weight. The sensitive volume of this parallel-plate chamber was approximately 1.7 mm³. Recombination corrections were determined based on theoretical and experimental collection efficiencies of the chamber.

Energy response was studied by determining beam quality conversion factors, which are shown in Fig. 4-3. This was done by cross-calibrating the LIC in a ⁶⁰Co beam against an air chamber with an established absorbed dose to water calibration coefficient, then by calibrating the LIC in various beam qualities of two different linacs. Corrections for recombination were applied. The figure shows a comparison of k_Q values for the liquid chamber at different beam qualities. A fit is applied to these values, and a comparison to k_Q values of an air chamber (taken from AAPM TG-51) over a similar range is given. The conversion factors for the liquid chamber are close to unity over the entire range, whereas the air chamber shows significant energy dependence.

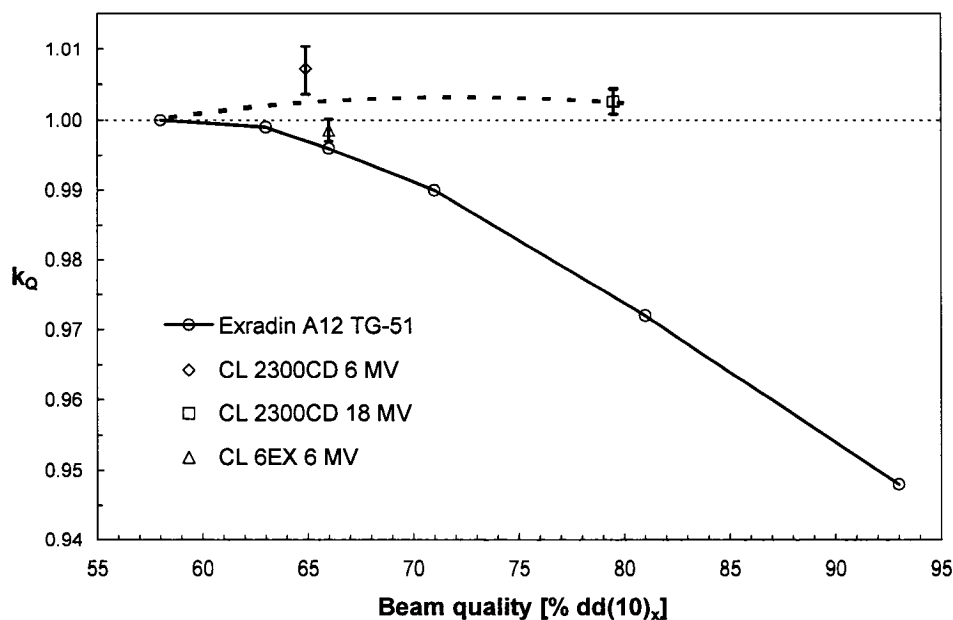


Figure 4-3. Beam quality conversion factors for the LIC (fitted dashed line) and for the Exradin A12 (solid line).²¹ Applied fits: 2nd degree polynomial (LIC data) and straight line (Exradin data).

Further studies of the LIC 9902-mix became impossible because of a chamber malfunction that could not easily be repaired. The next stage of investigation utilized a modified Exradin A14P air microchamber, which had a sensitive volume of about 1.12 mm³.

The chamber, referred to as the micro-LIC, was filled with isooctane and sealed. Tests of the behaviour and properties of the micro-LIC were performed, including chamber stability, response compared to the chamber unfilled, response to changing polarity, and linac beam pulse repetition frequency. Results showed first that under the same experimental setup including voltage across the chamber volume, the liquid-filled chamber response (4×10^{-4} nC/cGy) was 100 times greater than the signal acquired from the air-filled chamber (4×10^{-2} nC/cGy).

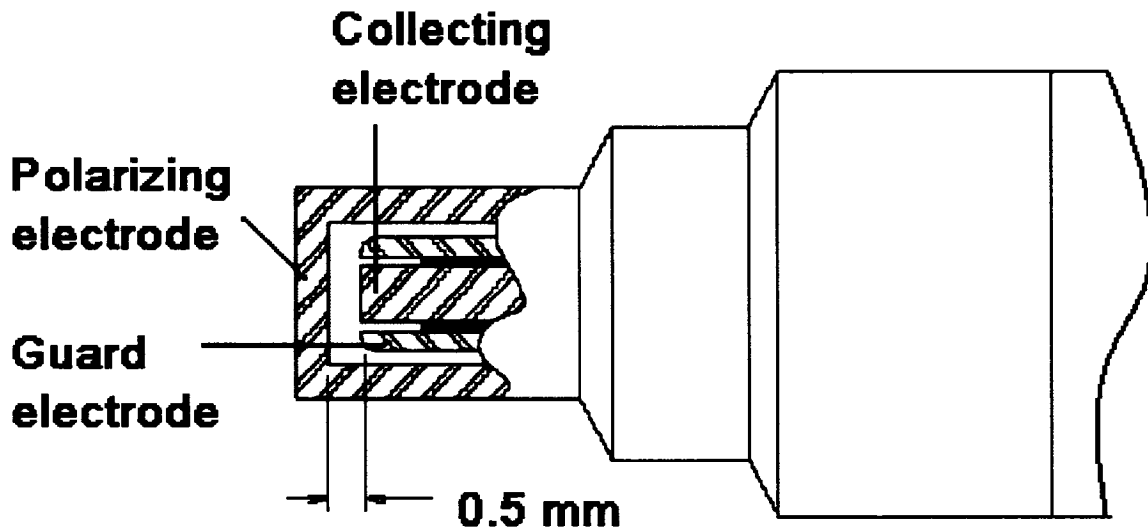


Figure 4-4. Schematic diagram of the modified Exradin A14P microchamber, called the micro-LIC when filled with isooctane. Image from Standard Imaging, Inc. (online: <http://www.standardimaging.com>), modified to show electrodes and plate separation.

The polarity correction was also much smaller when filled with liquid: 2% compared with 20% for the air-filled correction. There was a large variation of response with both changing voltage and changing pulse repetition rate. These variations are largely due to the mechanisms of ion recombination and will be explained in further detail in following sections. Problems that arose with this micro-LIC were unstable response over time, poor reproducibility, and erratic leakage current. The most significant problem, however, was post-irradiation residual current, which most likely resulted from ions produced in the zero-field region between the collecting and guard electrodes. Due to the problems that arose with the existing LIC 9902-mix and the modified air chamber, plans were developed for constructing a liquid ionization chamber of original design.

The first original chamber built was called the GLIC, which is an acronym for Guarded Liquid Ionization Chamber, referring to the guard electrode that surrounds the collecting plate in order to inhibit leakage currents and to define the sensitive volume. This chamber had construction problems, but the experience learned in its design was used in constructing a second version, the GLIC-02. This chamber was first used to determine its air-filled properties, which were compared to properties of the Exradin

A14P air microchamber. The recombination properties of both chambers were small and similar, but the GLIC-02 had about a 17% lower polarity correction than the Exradin A14P. Also significant was the fact that results obtained by the GLIC-02 chamber on separate days were reproducible within 0.2%. Thus any reproducibility problems that would later have been perceptible in the liquid-filled GLIC-02 would be limited to issues surrounding the liquid itself and not the chamber construction. When filled with isooctane, however, the stability and reproducibility of this chamber was very poor, even over relatively short intervals (hours). A hypothesis was that this could be due to chemical incompatibility or impurities introduced from the C552 conductive plastic electrodes. A third design using graphite electrodes was proposed. This third chamber was built and is called the GLIC-03, and investigation of the properties of this chamber is the focus of the research presented in this thesis.

References

- ¹ Pardo, J., Franco, L., Gomez, F. *et al.*, "Free ion yield observed in liquid isooctane irradiated by gamma rays. Comparison with the Onsager theory," *Phys. Med. Biol.* **49** (10), 1905-1914 (2004).
- ² Wickman, G. and Nyström, H., "The use of liquids in ionization chambers for high precision radiotherapy dosimetry," *Phys. Med. Biol.* **37** (9), 1789-1812 (1992).
- ³ Schmidt, W. F. and Allen, A. O., "Free-ion yields in sundry inadiated liquids," *J. Phys. C.; Solid State Phys.* **52**, 2345-2351 (1970).
- ⁴ Johns, H. E. and Cunningham, J. R., *The Physics of Radiology*, 4th ed. (Thomas, Springfield, Ill., 1983).
- ⁵ Berger, M.J., Coursey, J.S., Zucker, M.A. *et al.* (2005), *Stopping-Power and Range Tables for Electrons, Protons, and Helium Ions*, [Online] Available: <http://physics.nist.gov/Star> [May 1, 2006].
- ⁶ Johansson, B. and Wickman, G., "General collection efficiency for liquid isooctane and tetramethylsilane used as sensitive media in a parallel-plate ionization chamber," *Phys. Med. Biol.* **42** (1), 133-145 (1997).
- ⁷ Thomson, J. J., "The Röntgen Rays," *Nature (London)* **53**, 391-392 (1896).

- 8 Wickman, G., "Liquid Ionization Chambers: On their design, physical properties and practical applications," Report No. 314, Umeå, Sweden, 1991).
- 9 Wickman, G., "A liquid ionization chamber with high spatial resolution," *Phys. Med. Biol.* **19** (1), 66-72 (1974).
- 10 Mattsson, O., Svensson, H., Wickman, G. *et al.*, "Absorbed dose in water. Comparison of several methods using a liquid ionization chamber," *Acta Oncologica* **29** (2), 235-240 (1990).
- 11 Wickman, G. and Holmström, T., "Polarity effect in plane-parallel ionization chambers using air or a dielectric liquid as ionization medium," *Med. Phys.* **19** (3), 637-640 (1992).
- 12 Johansson, B., Wickman, G., and Holmström, T., "Properties of liquid ionization chambers at LDR brachytherapy dose rates," *Phys. Med. Biol.* **40** (4), 575-587 (1995).
- 13 Dasu, A., Löfroth, P. O., and Wickman, G., "Liquid ionization chamber measurements of dose distributions in small 6 MV photon beams," *Phys. Med. Biol.* **43** (1), 21-36 (1998).
- 14 Wickman, G., Johansson, B., Bahar-Gogani, J. *et al.*, "Liquid ionization chambers for absorbed dose measurements in water at low dose rates and intermediate photon energies," *Med. Phys.* **25** (6), 900-907 (1998).
- 15 Bahar-Gogani, J., Wickman, G., Johansson, L. *et al.*, "Assessment of the relative dose distribution around an ¹⁹²Ir line source using a liquid ionization chamber," *Med. Phys.* **26** (9), 1932-1942 (1999).
- 16 Bahar-Gogani, J., Grindborg, J. E., Johansson, B. E. *et al.*, "Long-term stability of liquid ionization chambers with regard to their qualification as local reference dosimeters for low dose-rate absorbed dose measurements in water," *Phys. Med. Biol.* **46** (3), 729-740 (2001).
- 17 Francescon, P., Cora, S., Cavedon, C. *et al.*, "Use of a new type of radiochromic film, a new parallel-plate micro-chamber, MOSFETs, and TLD 800 microcubes in the dosimetry of small beams," *Med. Phys.* **25** (4), 503-511 (1998).
- 18 Dempsey, J., Mutic, S., Low, D. *et al.*, "An Ideal Water-equivalent Cavity Theory Liquid Ionization Chamber," 2001 AAPM Annual Meeting, Salt Lake City, Utah, 2001 *Med. Phys.*
- 19 Eberle, K., Engler, J., Hartmann, G. *et al.*, "First tests of a liquid ionization chamber to monitor intensity modulated radiation beams," *Phys. Med. Biol.* **48** (21), 3555-3564 (2003).

- ²⁰ Berghofer, T., Engler, J. , Milke, J. M. *et al.*, "A Liquid Ionization Chamber As Monitor In Radiotherapy," Proceedings of the 9th Conference on Astroparticle, Particle, Space Physics, Detectors and Medical Physics Applications, Como, Italy, 2005 World Scientific.
- ²¹ Stewart, K.J., *Accurate Radiation Dosimetry Using Liquid- or Air-filled Plane-parallel Ionization Chambers*, M.Sc. Thesis, (McGill University, Montreal, 2001).

Chapter 5

The GLIC-03: Construction, Stability, Reproducibility, and Recombination

5.1 Construction

The new chamber is called the GLIC-03, where **GLIC** is an acronym for **Guarded Liquid Ionization Chamber**. A photograph of the chamber with its cap unscrewed is shown in Fig. 5-1, and a schematic diagram is shown in Fig. 5-2.

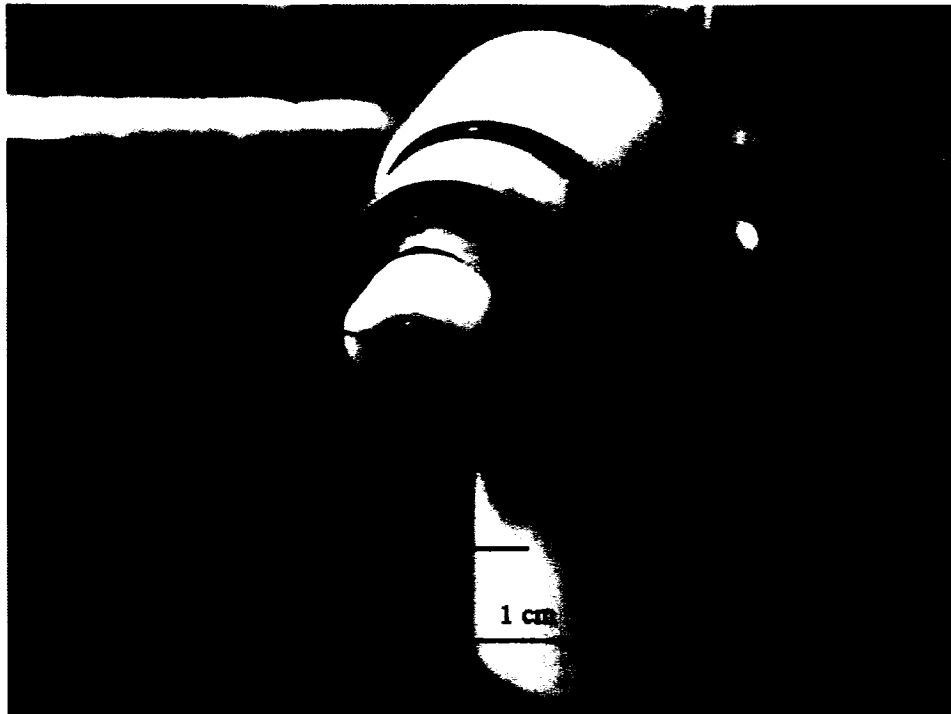


Figure 5-1. Photograph of inner details of the GLIC-03 with cap unscrewed. Visible are the collecting electrode, guard electrode, brass foil, and filling tube ends.

The GLIC-03 chamber body is made of Delrin and the electrodes are made of graphite. Teflon is used as an insulator between electrodes. The polarizing electrode is part of a cap that screws onto the main body. Connections from the main body (C-552 conductive plastic) to the graphite polarizing electrode are made through a stainless steel and brass

foil interface. Two stainless steel tubes are used to fill the inner volume. An O-ring is placed above the threads in order to seal the liquid inside when the cap is screwed on.

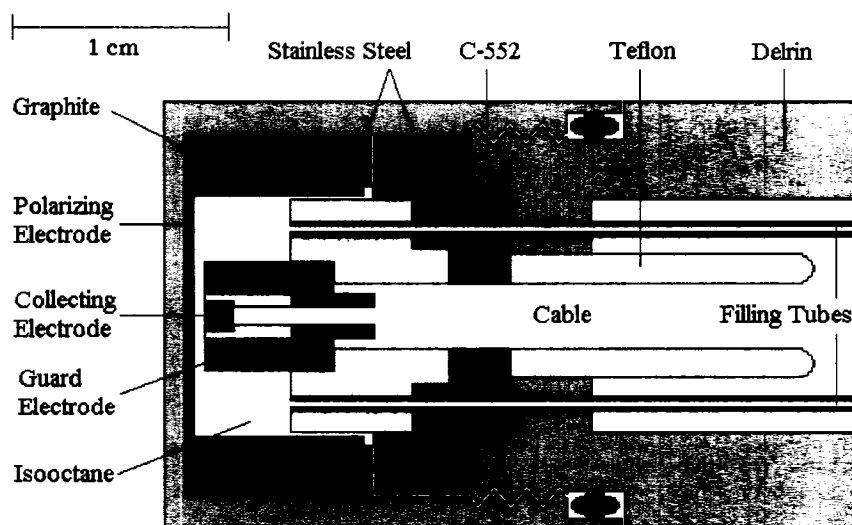


Figure 5-2. Schematic diagram of the GLIC-03.

Tetramethylsilane has a number of advantages over isooctane when it comes to choosing a liquid for use as the sensitive medium. TMS has a free-ion yield that is twice as large as that of isooctane. The ion mobility is also larger. Its effective atomic number is closer to water than isooctane. Also, the stopping power ratio water-to-liquid is slightly closer to unity for TMS than isooctane. Despite all of this, we chose to use isooctane (Aldrich, 99.8%), with no additional purification, as the sensitive volume material of the GLIC-03 for two important reasons. The first is that the boiling point of TMS is 26.6°C, while the boiling point of isooctane is 99.3°C.¹ Thus TMS will easily boil at room temperatures, in contrast to isooctane. Both liquids, however, will easily evaporate in air, so a sealed chamber was important. The second reason is that TMS costs about 30 times more than isooctane. Although TMS was superior in a few ways, the properties of isooctane were sufficient for our purposes, allowed for lower costs, and reduced the chance of evaporation.

5.1.1 Sensitive Volume and Plate Separation

The sensitive volume of the GLIC-03 is a cylinder with a cross-sectional area defined by the size of the collecting electrode and with a length defined by the separation

distance between collecting and polarizing plates. The cap of the chamber is screwed on until tight, thus the plate separation and sensitive volume size are not rigorously defined by chamber construction. For this reason, an air calibration and a capacitance test were performed in order to determine the sensitive volume and plate separation, respectively.

In order to determine the volume, the air-filled GLIC-03 was calibrated against an Exradin A12 air chamber with an established absorbed-dose-to-water calibration coefficient, $N_{D,w}^{Co}$, obtained from a standards laboratory. This calibration was conducted in 18 MV and 6 MV linac photon beams, in a Solid Water™ phantom at a depth of 10 cm. The field size was 10×10 cm² at a SSD of 100 cm. A Keithley 6517A electrometer was used for measurements and providing bias voltage. Measurements were taken with the GLIC-03 at +300 V using a dose setting of 600 MU at a dose rate setting of 600 MU/min. Such a high dose was used in order to obtain a large enough signal from the small sensitive volume. Measurements were taken with the Exradin chamber at +300 V using a dose setting of 100 MU at a dose rate setting of 400 MU/min, which provided a sufficient signal due to the large sensitive volume. Measurements for both chambers were also taken at +150 V in order to correct for general recombination (as described in section 3.2.3 for pulsed radiation beams) and at -300 V in order to correct for polarity effects (as described in section 3.2.2). Any leakage current was also measured and subtracted from the readings. Equation 2.53 expressed the absorbed dose calibration coefficient of an ionization chamber as the ratio of the absorbed dose at the point of measurement to the corrected measured signal. In this calibration, the absorbed dose to the medium surrounding the chambers is the same, so the absorbed-dose-to-water calibration coefficient for the air-filled liquid chamber in beam quality Q can be expressed as the relationship:

$$\left[N_{D,w}^Q \right]_{GLIC} = \left[N_{D,w}^{Co} k_Q \right]_{Exradin} \frac{M_{Exradin}}{M_{GLIC}}, \quad (5.1)$$

where k_Q is the beam quality conversion factor for the Exradin chamber at nominal beam quality Q , $M_{Exradin}$ and M_{GLIC} are the Exradin chamber and air-filled GLIC-03 signals, respectively, fully corrected for recombination and polarity effects and for leakage

currents. $N_{D,w}^{Co} k_Q$ is the absorbed-dose-to-water calibration coefficient for the Exradin chamber in a beam of quality Q .

The dose to water is related to the dose to air by the ratio of restricted stopping powers, as discussed in section 2.4.2 (Spencer-Attix cavity theory) and shown in equation 2.40. A different configuration of equation 2.47 gives the dose to air in terms of the mass of air in the sensitive volume:

$$N_{D,air} = \frac{D_{air}}{Q_{air}} = \frac{1}{m_{air}} \left(\frac{\overline{W}}{e} \right)_{air}. \quad (5.2)$$

Because the mass and volume of air are proportional by density (which is normalized for both chambers using temperature and pressure correction factors), we can determine the size of the GLIC-03 sensitive volume v_{GLIC} by using the ratio of absorbed-dose-to-water-calibration coefficients of the air-filled GLIC-03 and the Exradin air chamber and comparing to the nominal volume of the Exradin, $v_{Exradin}$, which is accurate within a few percent:

$$v_{GLIC} = v_{Exradin} \frac{[N_{D,w}^{Co} k_Q]_{Exradin}}{[N_{D,w}^Q]_{GLIC}}. \quad (5.3)$$

The Exradin has a calibration coefficient determined by a standards laboratory, as shown in Table 5-1. Also shown in the table are the nominal volume of the Exradin, beam quality conversion factors for the Exradin in the two photon beams, the calculated absorbed-dose-to-water calibration factors for the air-filled GLIC-03 for the two beams, and the sensitive volume size and error of the GLIC-03. Due to the close overlap of errors in volume determined by the two different energies, we consider the volume to be the average of the two.

Quantity	Units	$Q = 18 \text{ MV}$	$Q = 6 \text{ MV}$
$[N_{D,w}^{\text{Co}}]_{\text{Exradin}}$	cGy/nC	4.882	4.882
v_{Exradin}	cm^3	0.65	0.65
$[k_Q]_{\text{Exradin}}$	–	.9691	.9956
$[N_{D,w}^Q]_{\text{GLIC}}$	(cGy/nC)	1377	1409
v_{GLIC}	mm^3	2.233 ± 0.019	2.242 ± 0.016
v_{GLIC} (average)	mm^3	2.238 ± 0.025	

Table 5-1. Calibration coefficient, nominal volume, and beam quality conversion factors of Exradin A12 air ionization chamber used in this thesis. Calculated calibration coefficients and volume of air-filled GLIC-03.

For the capacitance test, the air-filled chamber was connected to a Keithley electrometer and the voltage across the plates was incremented by steps of 50 V up to a maximum voltage of 400 V. The charge (in Coulombs) was measured after each increment. Three separate measurements were performed and the resulting data is shown in Fig. 5-3.

The slope of each line was determined from a linear fit applied to each measurement, and the average slope is $6.26 \times 10^{-14} \text{ C/V}$. The slope corresponds to a change in collected charge over a change in applied voltage. This ratio is the definition of capacitance:

$$C = \frac{Q}{V}. \quad (5.4)$$

Because the plates are relatively closely spaced and the volume edges are well defined (due to the guard ring), the electric field across the separation is essentially uniform. Thus we can say that the applied voltage difference is simply the product of the plate separation d and the field strength E :

$$V = Ed. \quad (5.5)$$

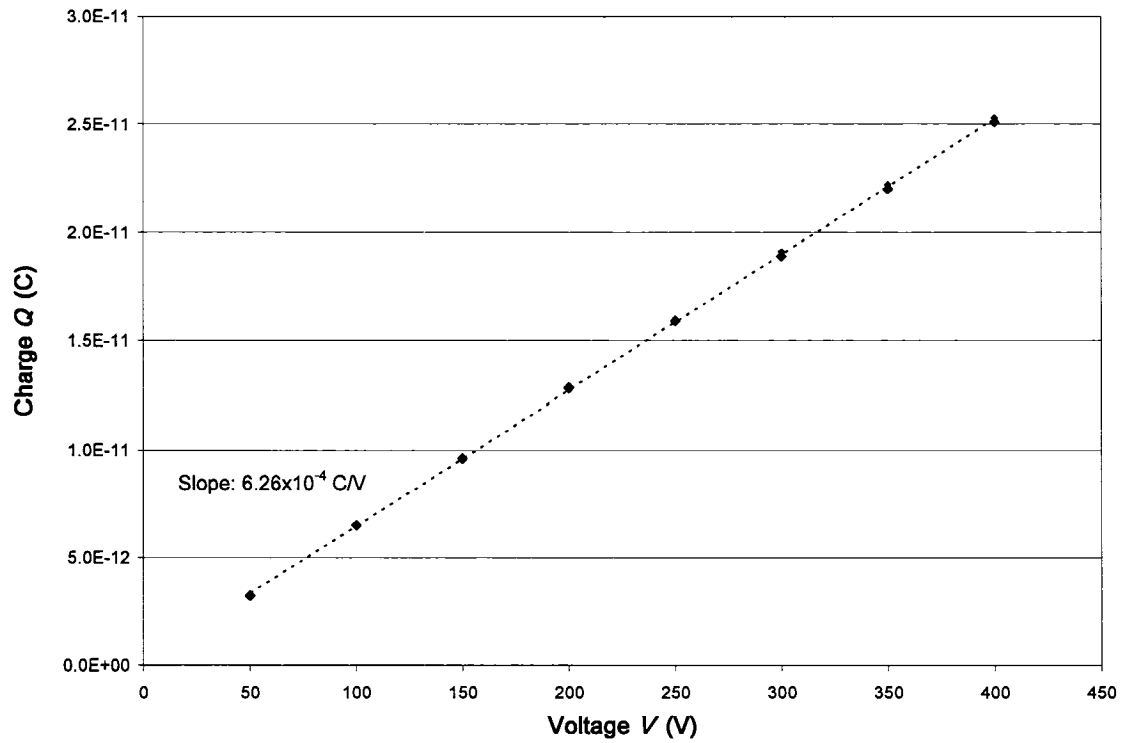


Figure 5-3. Charge collected by air-filled GLIC-03 after increments of 50 V up to 400 V for three separate trials (all overlap each other). The capacitance ($C = Q/V$) is determined in each trial by the slope of a line fit to the measured points.

From Gauss' law, the flux in the sensitive volume is given by:

$$EA = \frac{q_{\text{enclosed}}}{\epsilon_0}, \quad (5.6)$$

where \mathbf{E} is the electric field, A the cross sectional area of the sensitive volume, $q_{\text{enclosed}} = Q$ is the charge enclosed, and $\frac{1}{\epsilon_0}$ is the proportionality constant where $\epsilon_0 = 8.85 \times 10^{-12} \text{ C}^2/\text{N}\cdot\text{m}^2$ is the permittivity constant.² We can write the field strength as:

$$E = \frac{Q}{\epsilon_0 A}. \quad (5.7)$$

Substituting this expression into $V = Ed$, we have:

$$V = \frac{Qd}{\epsilon_0 A}. \quad (5.8)$$

Rearranging the equation and substituting $C = \frac{Q}{V}$ and $A = \frac{Vol}{d}$, where Vol is the volume, we have an expression for the separation of plates in terms of the volume and the capacitance:

$$d = \sqrt{\frac{\epsilon_0 Vol}{C}}. \quad (5.9)$$

Using the average of the two volumes calculated by the calibration, as well as the values of ϵ_0 and C given earlier, the plate separation is averaged to be $d = 5.625 \times 10^{-4}$ m, or approximately 0.563 mm. Thus the radius can be determined from the electrode area:

$$r = \sqrt{A/\pi}, \quad (5.10)$$

where

$$A = V/d. \quad (5.11)$$

The calculated radius is approximately 1.1 mm, and determined properties of the GLIC-03 are summarized in table 5-2.

$[N_{D,w}^Q]_{GLIC}$ (cGy/nC)	Volume (mm ³)	Electrode Separation (mm)	Electrode Radius (mm)
1392 (air-filled)	2.238 ± 0.025	0.563 ± 0.003	1.125 ± 0.005

Table 5-2. Summarized table of determined properties of GLIC-03.

5.2 Methods and Materials, and Results

For experiments involving radiation, we used the 18 MV beam of a Varian Clinac 21EX linear accelerator. The chamber was irradiated inside an RMI-475 Solid Water™ phantom at various depths and field sizes, as explained below for each experiment. A Keithley 6517A electrometer was used for all measurements and providing bias voltage for all chambers. All measurements were normalized to readings from a reference Exradin A12 (SN310) air-filled chamber, polarized at +300 V, to correct for any changes in machine output over time. This air chamber has an absorbed-dose-to-water calibration coefficient relative to ^{60}Co which is traceable to a national standards laboratory. It was placed in the Solid Water™ phantom at the same depth as the GLIC-03 for all experiments, as shown in the setup in Fig. 5-4. The air chamber readings were corrected for temperature and pressure according to the AAPM TG-51 protocol. A recent study has shown that the relative temperature dependence of a liquid ionization chamber filled with isoctane is less than 0.3% per degree, and that ambient humidity effects are negligible.³ The temperature remained within a degree throughout this research, thus no such corrections are applied in this thesis to the GLIC-03 measurements.

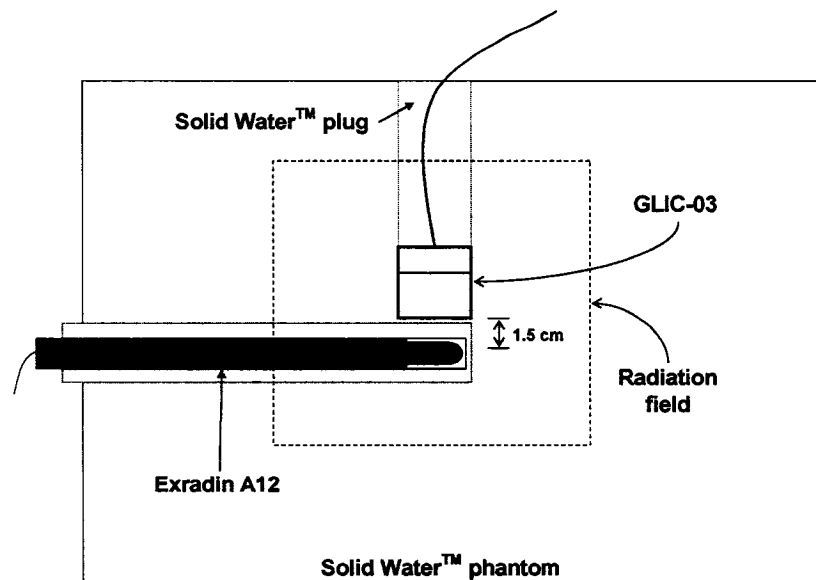


Figure 5-4. Side view of setup for stability, reproducibility, and recombination experiments involving the GLIC-03. The Exradin A12 air chamber sensitive volume is located within the radiation field (field size $10 \times 10 \text{ cm}^2$ at 100 cm SSD) in order to monitor linac output changes.

A pulse rate setting of 100 MU/min was used for each experiment. This is the lowest available setting, which is necessary in order to avoid incomplete collection of charge produced by one pulse before the arrival of the next. The lack of collection is illustrated in the recombination experiments.

5.2.1 GLIC-03 Inherent Leakage

Setup

For the leakage investigation, +500 V was applied across the sensitive volume of the GLIC-03. The current was measured over time after the voltage was applied. This experiment was performed five times.

Results and Discussion

Fig. 5-5 shows results of the five different trials of this experiment. It can be seen from the graph that the leakage current tends to settle down over time after a polarizing voltage is applied. With a current of approximately 0.0005 nC/s, the inherent charge collected by the chamber over a period of 60 seconds is about 0.03 nC.

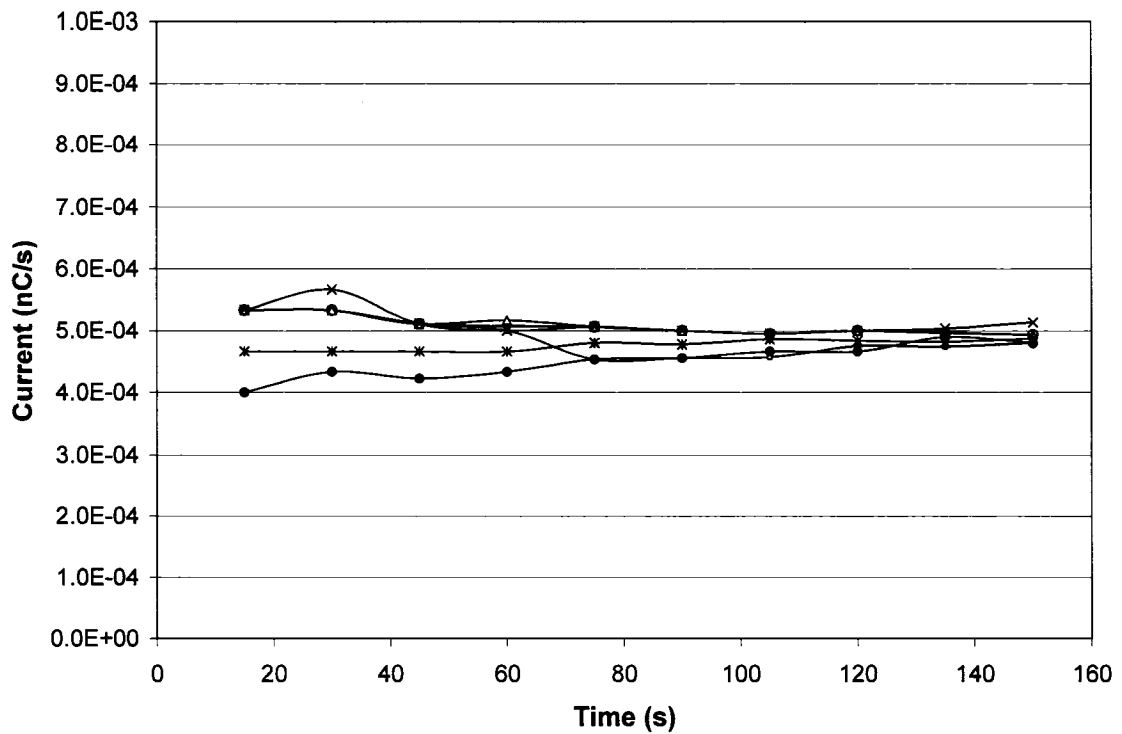


Figure 5-5. Inherent leakage current of the GLIC-03 over time while a polarizing voltage of 500 V is applied across the sensitive volume. 5 different trials are shown.

5.2.2 Stability of Response

Setup

For the stability investigation, measurements were taken with a polarizing voltage of 500 V and a dose setting of 250 MU. They were performed at 15 cm depth, 100 cm SSD, and with a field size of $10 \times 10 \text{ cm}^2$ at the phantom surface.

Results and Discussion

One difficulty with LICs is that chamber response can be unstable. Part of the reason for this is due to impurities that may exist in the liquid. These impurities may be inherent in the liquid or may diffuse into the liquid from the electrodes or the filling tubes. The leakage current can give a rough estimate of the amount of impurities in a dielectric liquid.⁴ Also, water and isooctane are immiscible and drops of water can interfere with leakage currents and measured signals. Radiation may trigger the effect of these impurities on the signal. Generally, radiation measurements are taken with the

GLIC-03 in a vertical position inside the phantom and the field of the beam at the side, as shown in Fig. 5-6a. If the chamber has not been sufficiently flushed, residue may exist and settle in or near the sensitive volume at the bottom.

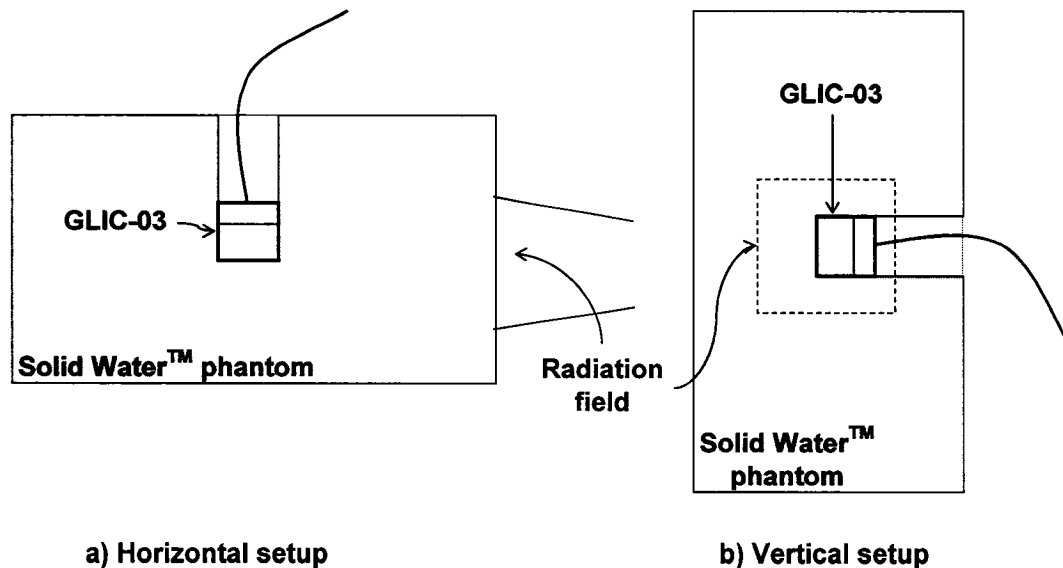


Figure 5-6. a) Horizontal GLIC-03 and Solid Water™ phantom setup, used for most experiments.
b) Vertical setup, used for stability experiment comparison.

On one occasion, effects of these impurities were clearly apparent. Readings were taken of one fill that showed a rapidly increasing response, as seen in “Fill 1 (horizontal)” of Fig. 5-7. A new fill was performed in hopes of flushing any impurities away. The resulting response was extremely erratic, as shown in “Fill 2 (horizontal)” of Fig. 5-7. The entire phantom was then turned on its side, as shown in Fig. 5-6b, and the chamber response immediately stabilized, as shown in “Fill 2 (vertical)” of Fig. 5-7. This shows that most likely an impurity was interfering with the signal in the horizontal case, and was removed from the sensitive volume in the vertical case.

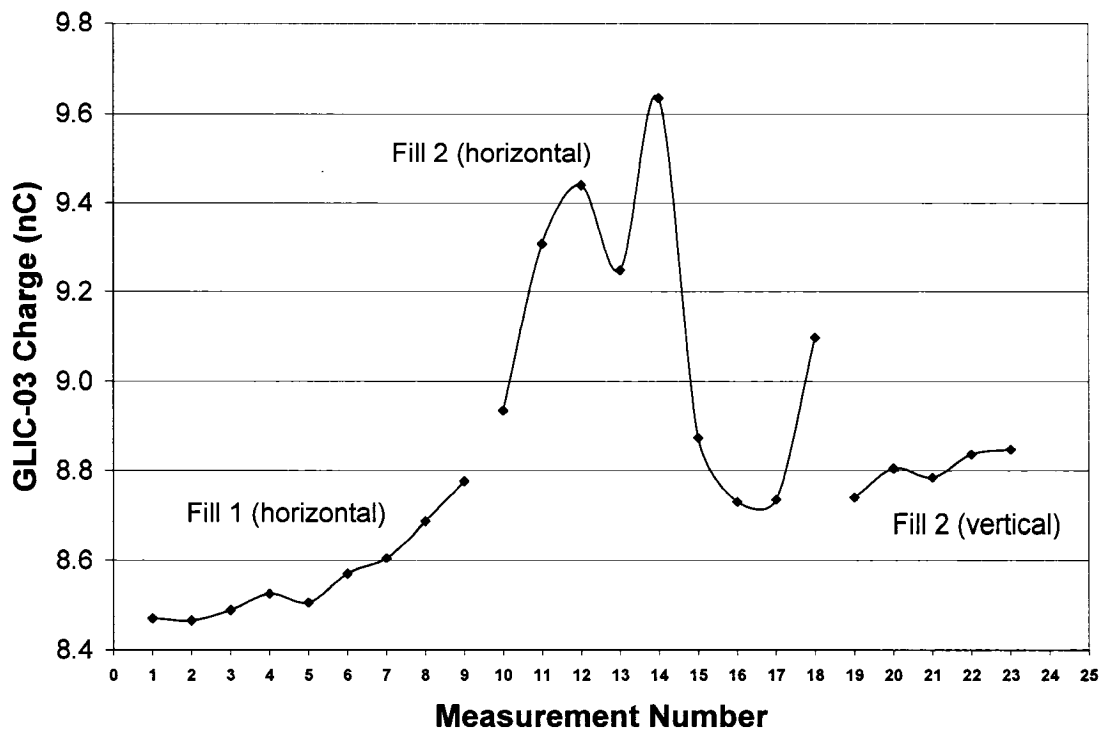


Figure 5-7. GLIC-03 response comparing two different fills and two different setup orientations of the same fill (Fill 2).

The chamber, once filled and assumed to be free of impurities, may take some time to settle down. This is illustrated in Fig 5-8, which shows the response of the GLIC-03 after the first 41 consecutive measurements were taken of a new fill. The five different sections (a-e) represent readings that were taken after a large dose was given (dose setting 2500 MU) to the chamber in order to force stability.

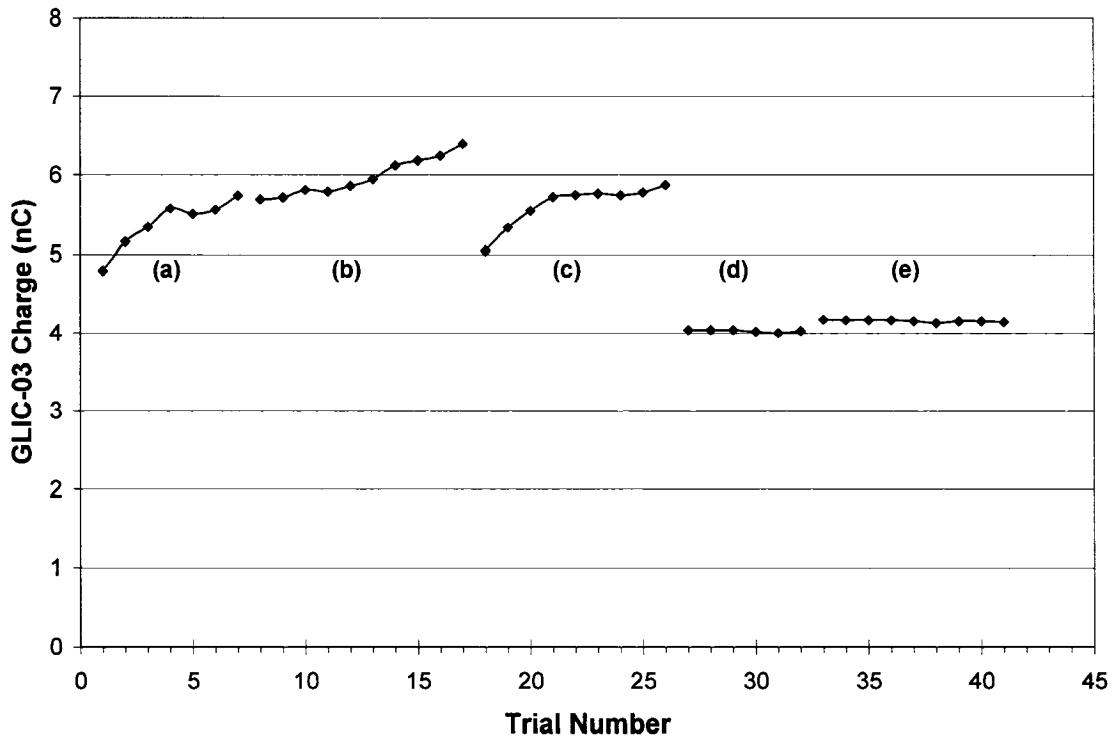


Figure 5-8. Changing response of the GLIC-03 after the first 41 measurements were taken. The five different sections (a-e) represent reading that were taken after a dose setting of 2500 MU was given.

Fig. 5-8 clearly shows the effect on the chamber after a large amount of dose has been given. The response initially increased in runs (a) through (c), though the overall response dropped between (b) and (c). Once the large dose was given after run (c), the response was stable in runs (d) and (e), remaining within 1%, and was then ready to use for other experiments.

Once the chamber has been sufficiently flushed and impurities are assumed to have been removed, and a sufficient dose has been given, the chamber response still changes over time. The first important experiment was to determine at what rate this change occurs, and how much time was available for other meaningful experiments to be performed. Fig. 5-9 shows the response of the chamber over time for three different trials, all compared to the initial reading of each trial.

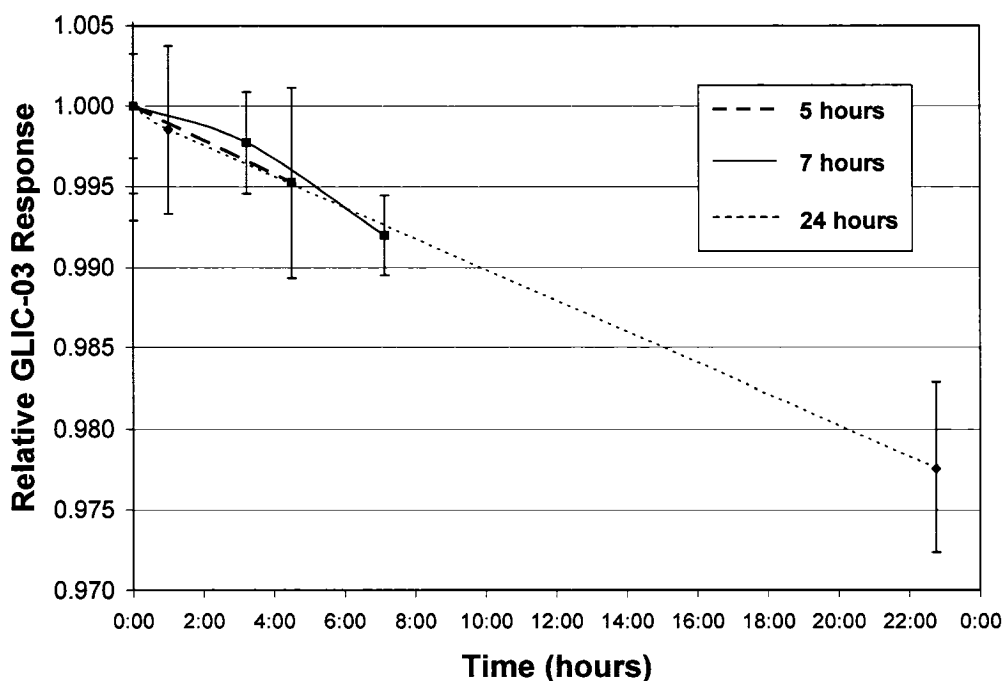


Figure 5-9. Response of the GLIC-03 over three trials of 5, 7, and 24 hours. The variation in response is less than 1% for up to 10 hours. A smoothed line fit was applied.

In the first and second trials, the response changed by less than 0.5% over 5 hours and less than 1% over 7 hours, respectively. In the third trial conducted over 24 hours, the response dropped by about 1% every ten hours. This small change in response over time suggests an acceptable stability for the duration of possible practical, relative dose measurements. This stability was verified throughout the duration of other experiments to ensure that change in chamber response was minimal.

5.2.3 Reproducibility

Setup

Measurements for reproducibility with different liquid fills were taken using the same physical setup as the stability investigation. These were performed after each new fill of isooctane in the chamber over a period of eight months. The first five fills were performed using older isooctane that may have had higher levels of impurities due to

atmospheric exposure. The remaining 13 fills were performed using a new bottle of isooctane.

Results and Discussion

Results of reproducibility as a function of fill are shown in Figure 5-10, where we see the response of the GLIC-03 after each fill over 18 different trials. As can be seen in the figure, the first five trials showed a large variation in response and leakage current. The rest of the trials show a smaller variation after the new bottle of liquid was used. After much rinsing of the chamber we can see the variation between the last eight trials to be less than 1.5% from the mean, showing good reproducibility. We can also see that the leakage current across the plate separation remained under 1% after a new batch of isooctane was used.

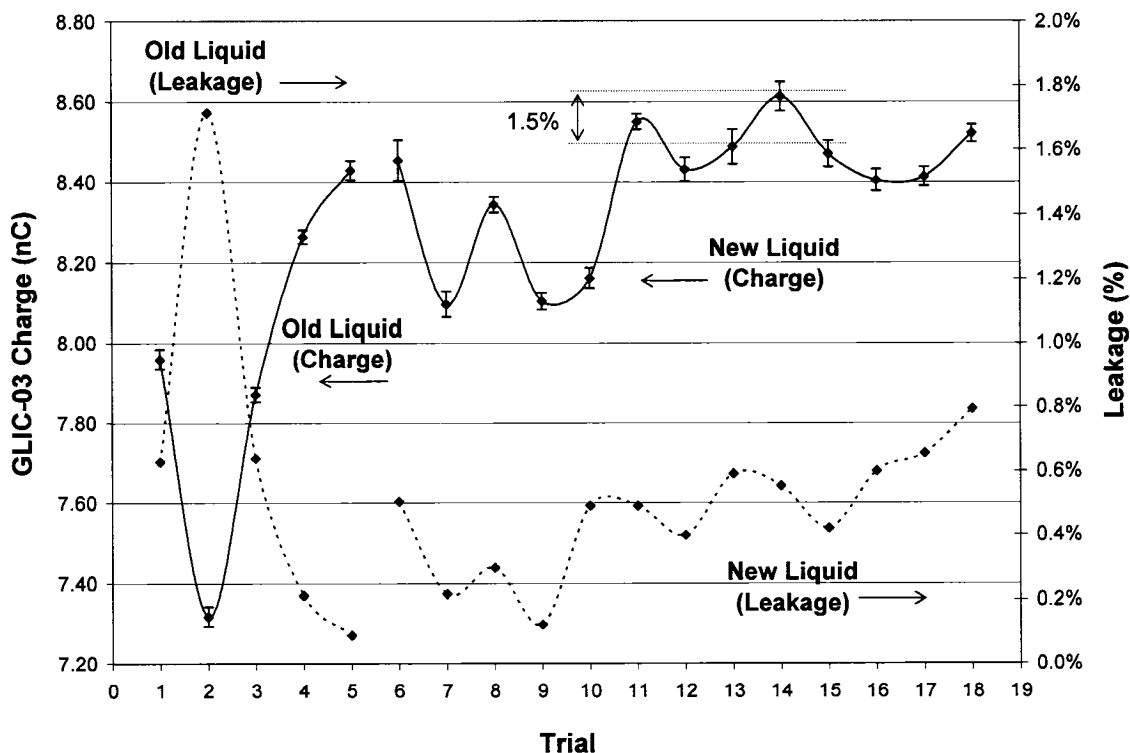


Figure 5-10. Response of GLIC-03 after each new fill. For trials 11-19, response was within 1.5% of the mean, as shown. Solid lines represent the chamber signal for a dose setting of 250 MU, referring to the left axis. Dashed lines represent the leakage signal as a percent of chamber reading, referring to the right axis.

5.2.4 Minimizing Recombination due to Pulse Overlap

Setup

Measurements were taken using the same physical setup as the stability investigation. In this experiment, two electron beam energies are used: 12 MeV and 16 MeV. For each electron beam, measurements were taken using dose rate settings of 100, 200, 300, and 600 MU/min. The dose setting for each measurement corresponded to a measurement time of 1 minute (e.g. 200 MU for 200 MU/min; 600 MU for 600 MU/min, etc.). The charge collected by the chamber was then normalized to the dose setting.

Results and Discussion

In Fig. 5-11, we can see that the GLIC-03 charge normalized to the dose setting decreases with increasing dose rate. This is due to the fact that the dose rate setting corresponds to the closeness in pulses delivered by the linear accelerator. 100 MU/min, for example, delivers 1 pulse in every 6 pulse cycle; 200 MU/min delivers 2 pulses; 300 MU/min delivers 3 pulses; and 600 MU/min delivers all 6 pulses in the cycle. 400 and 500 MU/min settings were not used in this experiment because the pulses are always only equally spaced in the other four settings.

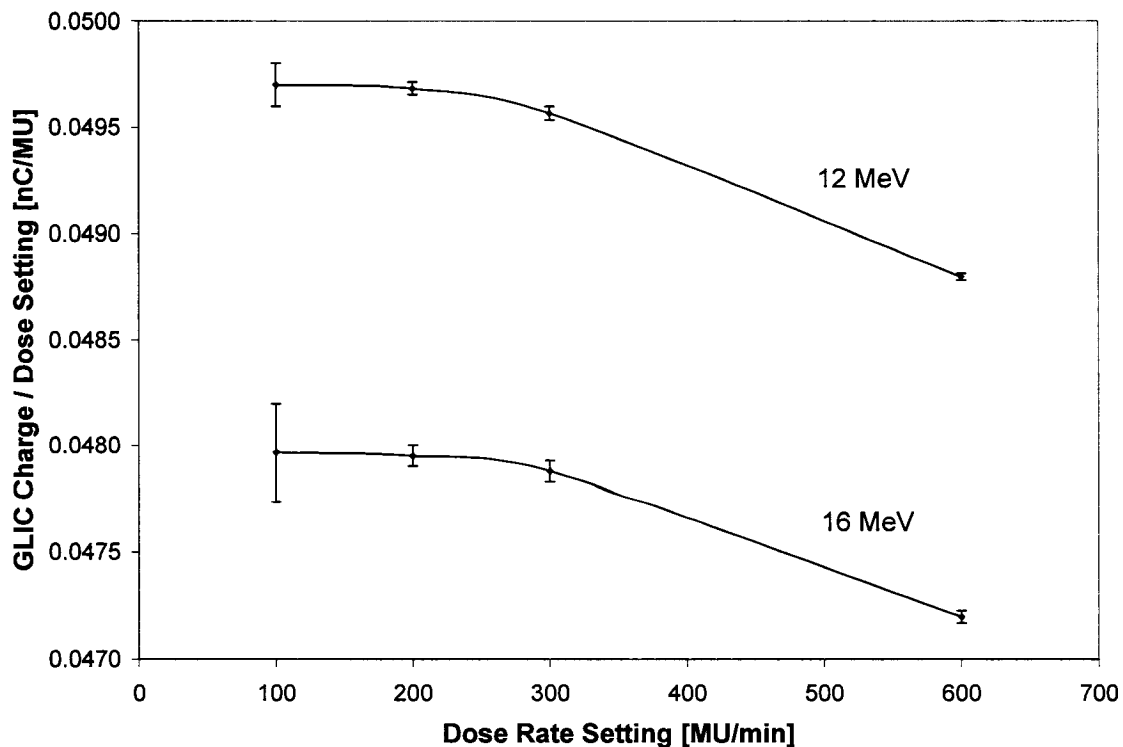


Figure 5-11. Response of GLIC-03 normalized to dose setting as a function of dose rate setting, for two different electron beam energies. A smoothed line fit was applied.

Each pulse results in a distribution of released ions in the chamber sensitive volume. Some time is necessary in order to collect all these ions. If some ions have not been collected when a second pulse occurs, they may recombine with the ions produced by the second pulse. As the pulses get closer and closer (or as the dose rate setting increases), more and more ions recombine and the collection signal decreases, as is shown in the figure. For this reason, to minimize incomplete charge collection before the arrival of a second pulse, the dose rate setting used in experiments with the GLIC-03 is generally 100 MU/min, unless indicated otherwise.

5.2.5 Recombination Corrections

Setup

The dose per pulse was reduced relative to reference conditions by increasing the SSD of the phantom holding the GLIC-03 and the Exradin A12 chambers. Measurements of ratios of GLIC-03 readings to Exradin A12 readings were performed at SSD intervals

of 50 cm in the range from 100 cm to 300 cm, while the field size was $10 \times 10 \text{ cm}^2$ at 100 cm from the source. Measurements were taken at each dose rate with various voltages (and thus electric field strengths) between 100 V and 700 V. A dose setting of 100 MU was used, with a dose rate setting of 100 MU/min.

Results and Discussion

Although the mechanisms for ion recombination in liquids are the same as in air, their effect is quite different in the two media. As mentioned in section 4.1.5, the ionization density of the dielectric liquids is about 300 times larger than air, allowing for a small sensitive volume. Also, presented in the same section is the fact that the mobility of ions is three to four orders magnitudes smaller than in air. Because of these two properties, ion recombination is very significant in liquids and correction factors must be determined and applied.

In section 3.2.3, the mechanisms of initial recombination and general recombination were explained. It was stated in section 3.2.3.1 that initial recombination is dependent on the ionization density as well as on the electric field strength normal to the particle track. It was also stated that in air chambers, initial recombination was generally negligible due to the relatively large distance between atoms. This distance is not conducive for recombination between ions formed along the same particle track. Initial recombination becomes negligible even at relatively low field strengths. Due to the high density in liquid chambers, however, initial recombination occurs much more readily. Fig. 5-12 shows a typical ionization curve for a liquid ionization chamber.

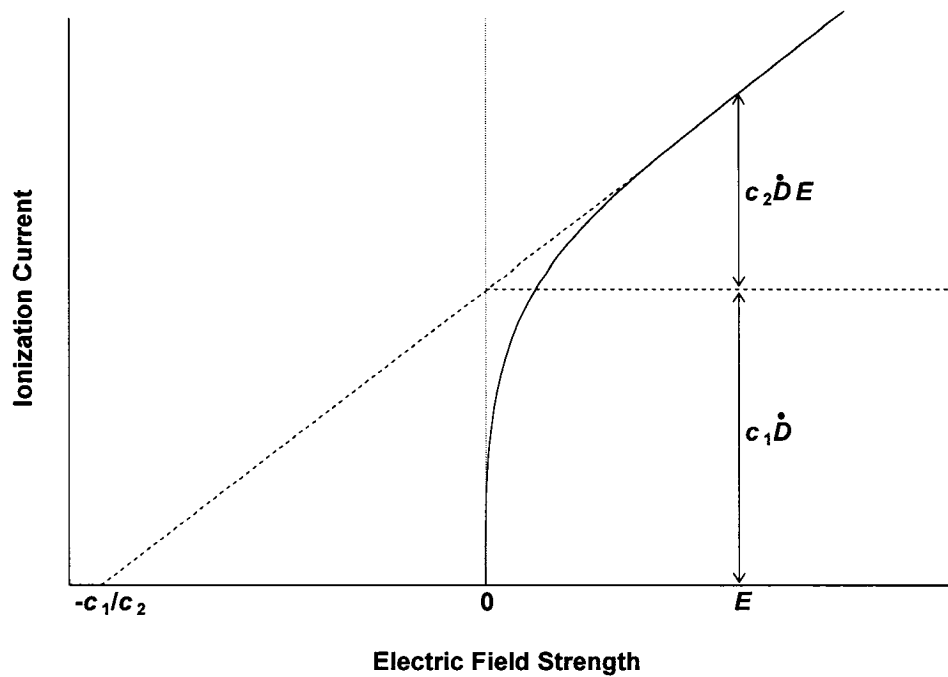


Figure 5-12. Typical liquid ionization chamber ionization curve (full line). A saturation region is never reached due to increased availability of free ions. A fit (dashed line) of the “linear region” is used in determining general collection efficiency.

Comparison to the air ionization curve in Fig. 3-3 shows some fundamental differences. Perhaps the biggest difference is that the saturation region, apparent in air chambers, is never achieved in liquid chambers. Even after general recombination effects are minimized by high field strengths, the current continues to increase. This is due to increased production of free ions as the electric field supplies more energy. As the electric field increases, free electrons released through ionization have more probability of escaping the field of their parent atom rather than immediately being attracted back to it. Because we are at the same dose rate, the number of tracks per unit time remains the same but the average concentrations of negative ions (formed with the electrons) and positive ions along the same track increase linearly. The ionization current in the linear region is defined by the components $c_1 D'$ and $c_2 D'E$, where E is the electric field strength, D' is the dose rate, and c_1 and c_2 are fit constants that represent the fraction of ions that escape initial recombination due to diffusion and the field strength, respectively.

Because of the lack of saturation, the two-voltage technique described in section 3.2.3.2 cannot be used for ion recombination corrections.

Fig. 5-13 shows the saturation curves of the GLIC-03 for different polarizing voltages. The different lines correspond to different dose per pulse values. These values were changed by increasing the SSD of the phantom containing the GLIC-03.

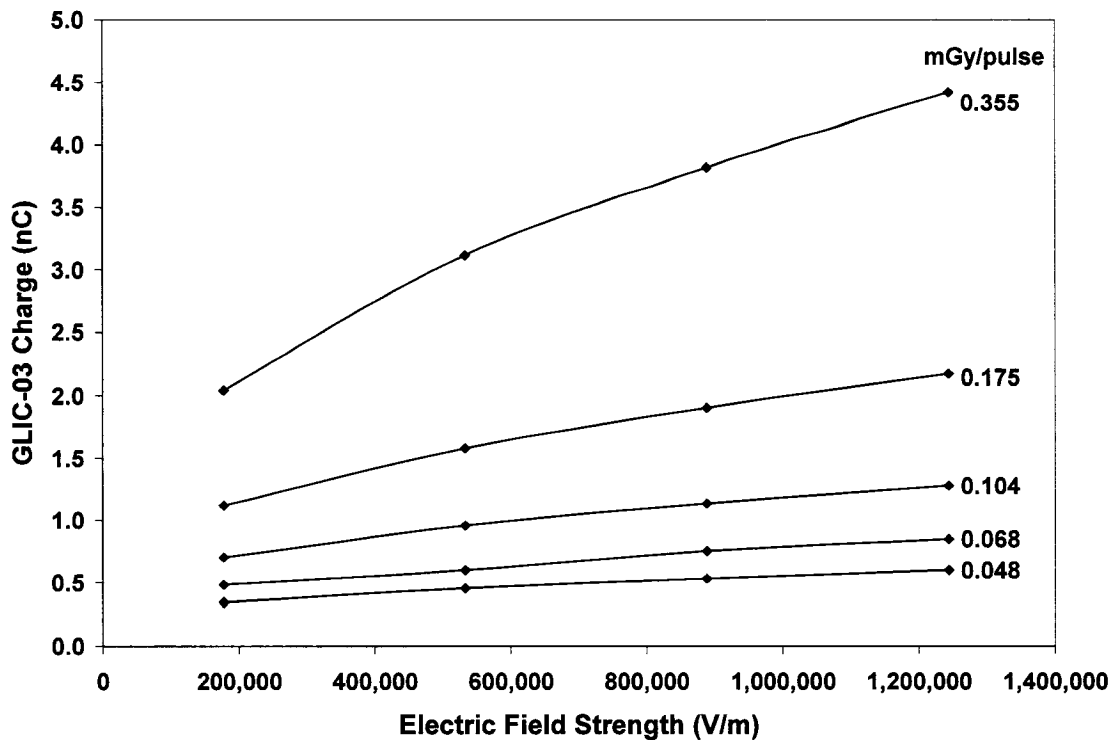


Figure 5-13. GLIC-03 ionization curve for various dose per pulse values. Standard deviations are included but are too small to be visible. A smoothed line fit was applied.

Two other possible methods for correcting for recombination are proposed in this thesis. The first method is to determine the collection efficiency of the ionization chamber using a theoretical model. The second method is to measure the change in collected charge as a function of dose rate and use these measurements to correct for the relative difference in recombination at different dose rates.

Theoretical General Collection Efficiency

Boag's theory for recombination in gas-filled ionization chambers was presented in section 3.2.3.2. In this first method of correcting for ion recombination, we follow the investigations of Johansson *et al.*⁵ in the determination of ion collection efficiency by modifying Boag's theory to liquids. In that paper, the theoretical general collection efficiency of a liquid chamber, f_{th} , was determined. An important difference in collection efficiency for liquid chambers is that initial recombination is always a significant component and therefore included. A saturation region is never reached due to increased production of free ions, even though general recombination is minimized at high field strengths. Instead, the current increases linearly with increasing field strength.

In order to determine the theoretical collection efficiency, i_{th} , the theoretical current in the absence of general recombination, must be determined. In order to do this, the current as a function of electric field must be measured for a low dose rate where general recombination is assumed to be negligible. The ionization current in the linear region at a specific electric field strength is divided into two components, as shown in Fig. 5-9:

$$i_{th} = c_1 D' + c_2 D'E, \quad (5.10)$$

where E is the electric field strength and D' is the dose rate. The parameters c_1 and c_2 are fit constraints described earlier. Fig. 5-14 shows the ionization curve of the GLIC-03 for a dose rate of 0.05 mGy per pulse, including the linear region extrapolation for determining fit parameters.

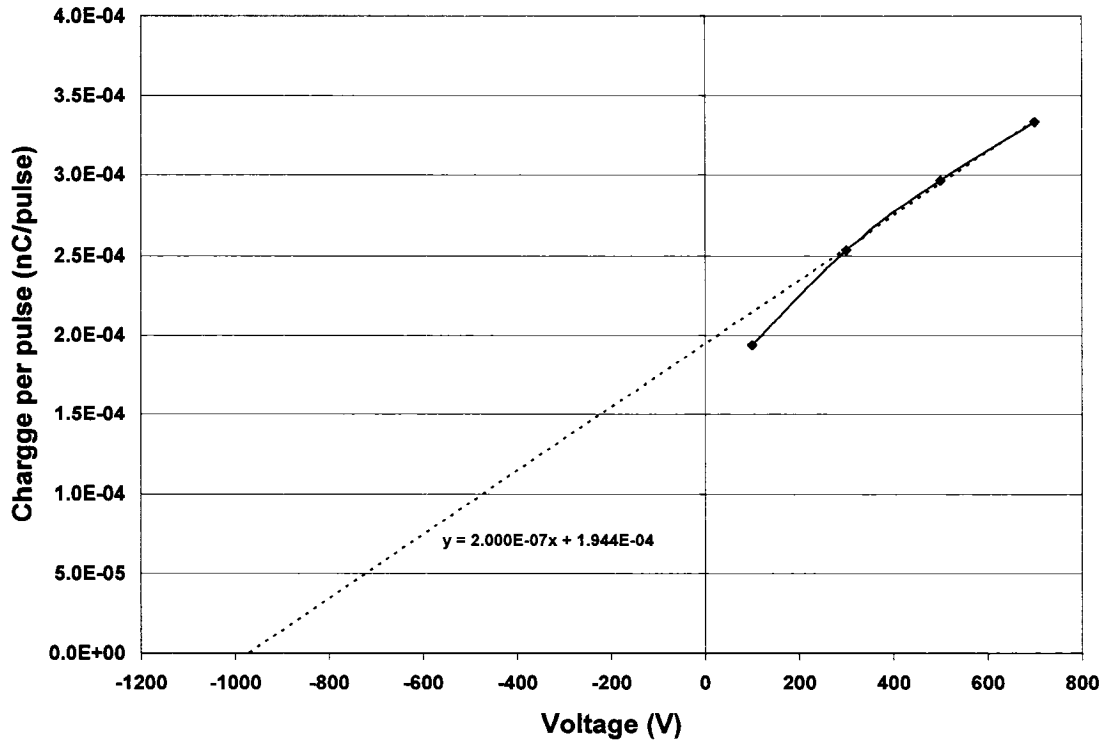


Figure 5-14. Extrapolation of one ionization curve of the GLIC-03, with a 0.05 mGy/pulse dose rate.

The theoretical collection efficiency was determined according to the following relationship⁵:

$$f_{th} = \frac{1}{u} \ln(1+u), \quad (5.11)$$

where, as we similarly saw in section 3.2.3.2 for air chambers,

$$u = \mu \frac{r}{U} d^2 \quad (5.12)$$

and

$$\mu = \frac{\alpha}{e(k_1 + k_2)}. \quad (5.13)$$

Again, k_1 and k_2 [$\text{m} \cdot \text{V}^{-1} \cdot \text{s}^{-1}$] are the positive and negative ion mobility, respectively, $e = 1.602 \times 10^{-19}$ C is the electron charge, d [cm] is the plate separation, U [V] is the applied potential, α is the recombination rate constant, and r is the amount of charge per

unit volume and radiation pulse liberated by radiation and escaping initial recombination. r is related to the experimental current by:

$$r = \frac{Q}{V\nu t}, \quad (5.14)$$

where Q is the charge that is produced during time t , ν is the radiation pulse frequency, and V is the sensitive volume. The recombination rate constant, α , is approximated⁶ for dielectric liquids with low permittivity, ε , to be:

$$\alpha = \frac{e(k_1 + k_2)}{\varepsilon_0 \varepsilon}, \quad (5.15)$$

where ε_0 is the permittivity of free space. Substituting this into equation 5.13, we see that μ simplifies for use in equation 5.12:

$$\mu = \frac{1}{\varepsilon_0 \varepsilon}. \quad (5.16)$$

Thus, the theoretical collection efficiency can be calculated using the following version of u after substituting equations 5.14 and 5.16 into equation 5.12:

$$u = \frac{1}{\varepsilon_0 \varepsilon} \frac{Qd^2}{UV\nu t}. \quad (5.17)$$

In our study, we determined the fit constraints using the charge per pulse at dose rate D_0 , and then calculated the theoretical charge per pulse from equation 5.10, which is scaled by the ratio of dose rates D/D_0 . The volume can also be expressed as $V = \pi r^2 d$, where r is the electrode radius and d is the plate separation. In addition, ν represents the number of pulses per unit time ($\nu = \# \text{ pulses/time}$), so νt is simply the number of pulses. Because of these relationships, equation 5.17 can be expressed as:

$$u = \frac{1}{\varepsilon_0 \varepsilon} \frac{i_{theor} d}{\pi r^2 U} \left(\frac{D}{D_0} \right). \quad (5.18)$$

Fig. 5-15 shows the theoretical general collection efficiency for the GLIC-03 over various electric field strengths and doses per pulse. For low doses per pulse and high field strengths, the efficiency was greater than 0.99, in agreement with Johansson *et al.*⁵ At low field strengths, efficiency decreases due to the fact that the electric field strength is not sufficient to overcome incomplete charge collection of one pulse before the arrival of the second pulse. General recombination occurs after initial track structure is destroyed, and occurs between positive and negative ions formed by different ionizing particles. Thus general recombination changes with dose rate – that is, with changing number of tracks per unit time – and electric field strength.⁷ We see in our results that efficiency decreases with increasing dose per pulse due to general recombination of ions from a larger numbers of ionizing particle tracks. Recombination corrections in liquids are thus especially important for high dose rates and low field strengths.

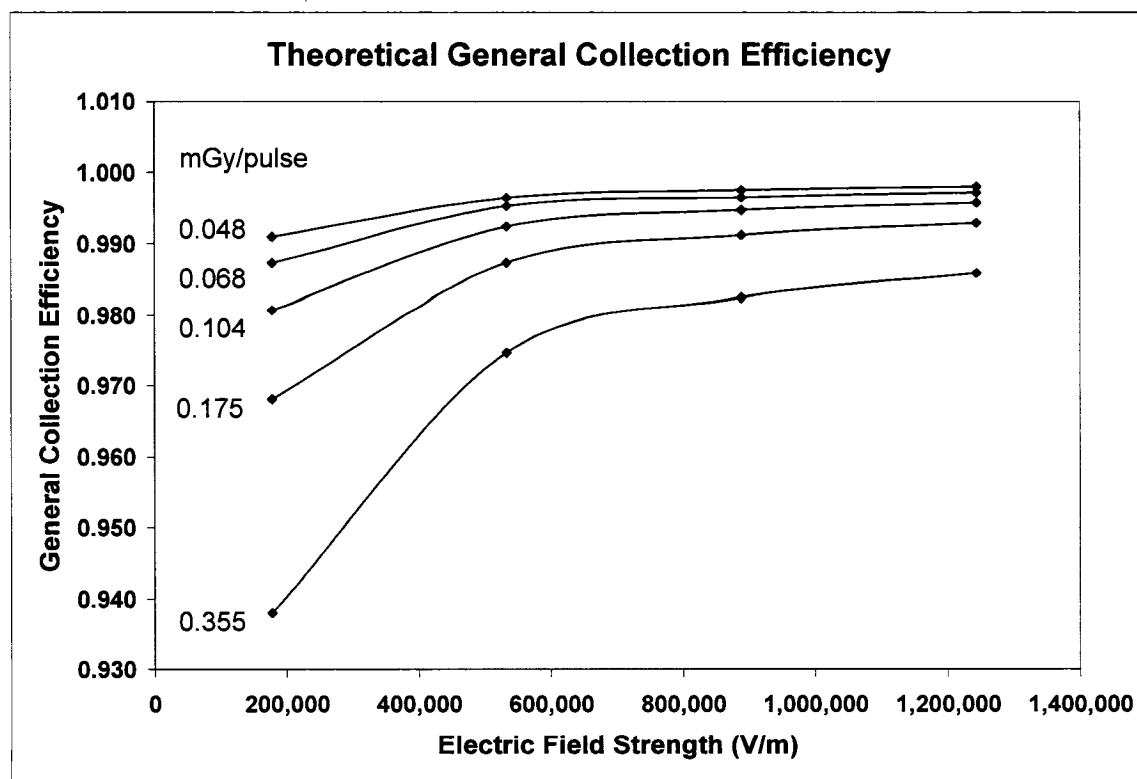


Figure 5-15. Theoretical general collection efficiency of the GLIC-03 for various doses per pulse, as a function of electric field strength. A smoothed line fit was applied.

Determining General Recombination as a Function of Dose Rate

In this method, we measured the change in collected charge as a function of dose rate and use these measurements to correct for the relative difference in recombination at different dose rates. It is important to emphasize here that this method is not an absolute calculation of the efficiency of the chamber, but rather determines a relative correction factor due to loss of signal by recombination at one dose per pulse compared to another dose per pulse.

In order to calculate the dose at different SSD positions, an air ionization chamber (Exradin A12) was used. Because recombination in the air chamber is small compared to recombination in the liquid chamber, and shows a much smaller variation with dose rate, recombination corrections were not applied to air chamber measurements. The ratio of their readings would be constant were it not for the difference in recombination of the two chambers.

In Fig. 5-16, two effects of recombination can be seen. The first is an increasing relative signal with a decreasing dose rate. As explained earlier, the number of ionizing particle tracks that pass through any volume depends on the dose rate. As the dose rate decreases, fewer tracks per unit time produce fewer ions per unit time, allowing more ions to be collected rather than recombining.

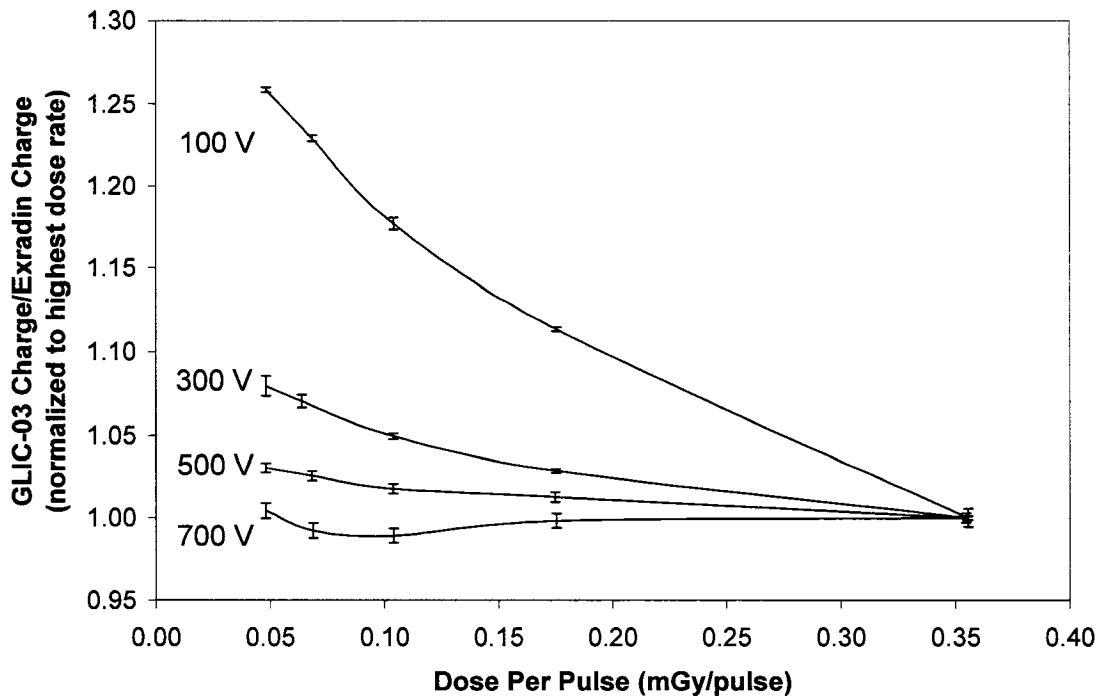


Figure 5-16. GLIC-03 response in an 18 MV beam as a function of dose per pulse in the phantom, for various voltages across the chamber sensitive volume. GLIC-03 signals are compared to corresponding air chamber signals and normalized to highest dose rate. A smoothed line fit was applied.

The effect of the electric field strength on recombination can also be seen by comparing measurements at different polarizing voltages. For low voltages the relative signal varies by 25% over the range of dose rates used, compared to a variance less than 3% for the highest voltages used. As the dose rate (and thus the number of tracks) increases, the lower voltages are not sufficient to overcome recombination of the large number of ions produced. Also, at 100 V there is pulse overlap, causing a large increase in the ion density and therefore much greater effects of recombination.

References

- ¹ Eberle, K., Engler, J., Hartmann, G. *et al.*, "First tests of a liquid ionization chamber to monitor intensity modulated radiation beams," *Phys. Med. Biol.* **48** (21), 3555-3564 (2003).
- ² Wolfson, R. and Pasachoff, J. M., *Physics for scientists and engineers*, 3rd ed. (Addison-Wesley, Reading, Mass., 1999).

- ³ Franco, L., Gomez, F., Iglesias, A. *et al.*, "Liquid-filled ionization chamber temperature dependence," *Nuclear Instruments and Methods in Physics Research* **560** (2), 584-588 (2006).
- ⁴ Wickman, G. and Nyström, H., "The use of liquids in ionization chambers for high precision radiotherapy dosimetry," *Phys. Med. Biol.* **37** (9), 1789-1812 (1992).
- ⁵ Johansson, B., Wickman, G., and Bahar-Gogani, J., "General collection efficiency for liquid isooctane and tetramethylsilane in pulsed radiation," *Phys. Med. Biol.* **42** (10), 1929-1938 (1997).
- ⁶ Debye, P., "Reaction rates in ionic solutions," *Trans. Electrochem. Soc.* **82**, 265-272 (1942).
- ⁷ Boag, J. W., "Ionization Chambers" in *The Dosimetry of Ionizing Radiation*, Vol. II, edited by K. R. Kase, B. E. Bjärngard, and F. H. Attix (Academic Press, San Diego, 1987), pp. 169-233.

Chapter 6

Measurements of the Photon Build-up Region

6.1 Introduction

Our investigations of stability and reproducibility of the GLIC-03, as well as the evaluation of methods for correction of recombination, now allow for measurements of a region with lack of charged particle equilibrium. The build-up region of a percent depth ionization or percent depth dose curve is one such region, and was described in section 2.7.1. The purpose of this study is to utilize the GLIC-03 for measurements of the build-up region, and to compare its measurements to another established, more traditional detector. A diamond detector, loaned to us by Dr. Stanislav Vatnitsky (Vienna), was used due to its small sensitive volume and tissue-equivalence, two characteristics similar to the liquid chamber. The liquid-filled GLIC-03 measurements were also compared to measurements made with the GLIC-03 filled with air, in order to determine any differences in measurements due to fluence perturbations.

6.2 Methods and Materials

In this experiment, the 18 MV photon beam of a Varian Clinac 21EX linear accelerator was used. The chamber measuring the build-up region was positioned in a Solid Water™ phantom with its entrance window side flush with the phantom surface. The centre of a $10 \times 10 \text{ cm}^2$ beam was positioned at the centre of the chamber sensitive volume at an SSD of 100 cm. The phantom and chamber were situated on a sturdy slide whose position could be changed with the aid of a digital caliper. Various thicknesses of Solid Water™ could then be placed in front of the chamber while moving the slide and maintaining a constant SSD of 100 cm. This allowed for measurements in the build-up region in a Solid Water™ phantom ranging from depths as shallow as the chamber wall to depths past the depth of maximum dose.

For measurements with the GLIC-03, a polarization of +500 V was applied across the GLIC-03 sensitive volume (+300 V for the air-filled GLIC-03). The point of measurement of the liquid-filled GLIC-03 was the centre of the sensitive volume, while the point of measurement of the air-filled GLIC-03 was the centre of the entrance window. As such, Solid Water™ was scaled by electron density and chamber components were scaled by mass density in order to determine equivalent depth in water. An Exradin A12 cylindrical air chamber was positioned in air, with a build-up cap, in front of the phantom in the corner of the radiation field in order to monitor fluctuations in linac output for the duration of the experiment. Exradin measurements were also corrected for pressure and temperature changes. Measurements made with the liquid-filled GLIC-03 were corrected for recombination using a linear fit of the efficiency of the chamber as a function of dose per pulse, as described in section 5.2.5, where the chamber has been polarized with 500 V, and measurements were taken in an 18 MV beam with a dose rate of 500 MU/min. For the air-filled GLIC-03, measurements were made at +300 V and -300 V in order to correct for polarity effects (see section 3.2.2). Recombination is negligible in the air-filled chamber, so no correction was necessary.

As mentioned, the measurements of the build-up region were compared to those made by a diamond detector, a dosimeter suitable for measuring relative dose distributions in high energy photon beams. The resistance of a diamond changes in the presence of radiation, so applying a bias voltage allows measurement of a current that is proportional to the radiation dose rate. A diamond detector is tissue equivalent and features a flat energy response and little directional dependence. It also has a very high sensitivity and is resistant to radiation damage.¹ The detector does have a dose rate dependency in pulsed radiation beams of about 2% in the range from 0.05 to 30 Gy/min.²

A schematic of the diamond detector used is shown in Fig. 6-1, including the following labels: “5” represents a polystyrene chassis, “7” is a metal holder, “2” and “3” are composite cables, “4” and “6” are hermetization (water-sealing) collars; and “1” represents the detector head. In the detector head, “8” indicates the diamond detecting structure, to which contacts and conductors “9” through “12” apply a bias voltage and return a signal (reference “characteristics of diamond detectors of ionizing radiation”).

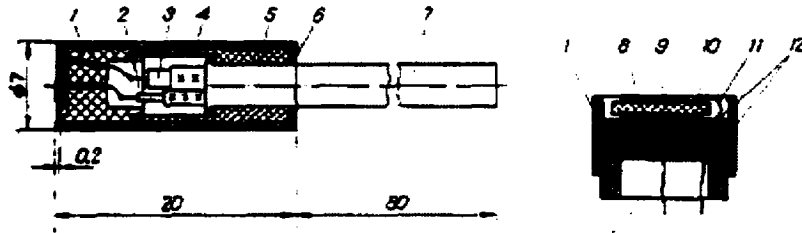


Figure 6-1. Schematic diagram of the entire diamond detector (left) and the detecting unit (right).³

The head of the detecting unit (shown on the right in Fig. 6-1) contains a diamond crystal with a sensitive volume of approximately 1.6 mm^3 , and a sensitive volume thickness of 0.3 mm. The operating bias voltage applied across the detector is +100 V, and a pre-irradiation dose of 5-10 Gy was required. The voltage was applied and the signal was read using a Keithley electrometer. The build-up measurements were taken in the same set-up as used with the GLIC-03 and beam output was again monitored by an Exradin A12 in the same manner. Measurements were made with the detectors in the small range from 0.4 to 1.0 Gy/min, so corrections of dose rate dependence of the diamond detector were small and not applied. A dose setting of 100 MU and a dose rate of 500 MU/min was used. Leakage measurements were also determined. The point of measurement of the diamond detector was the centre of the sensitive volume. Again, Solid Water™ was scaled by electron density and chamber components were scaled by mass density in order to determine equivalent depth in water.

6.3 Results and Discussion

Fig. 6-2 shows the result of the comparison of build-up region percent depth ionization measurements made by the GLIC-03 and the diamond detector. The data was normalized to d_{max} (approximately 3.3 cm), and a sixth-degree polynomial was applied to each curve in order to plot all three at the same depths.

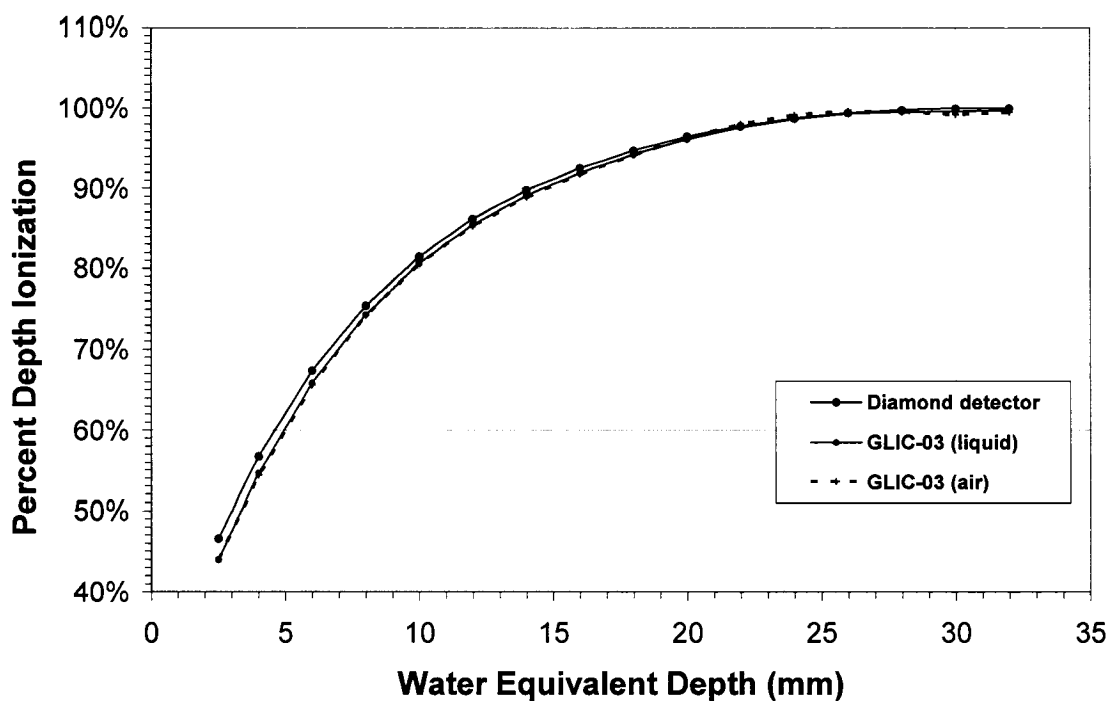


Figure 6-2. Build-up region measurements of GLIC-03 (air- and liquid-filled) and diamond detector.

The diamond detector curve is about 5-6% higher than the either GLIC-03 curves at the shallowest depths, likely an indication of the effects of dose rate on the diamond detector response, as mentioned in the previous section. Inclusion of corrections due to dose rate effects of the diamond detector would require a more detailed study. The liquid-filled and air-filled GLIC-03 build-up curves follow essentially the same paths, as can be seen in the Fig. 6-3. The two agree within 0.5% at the shallowest part of the build-up region and then within 1% for the remainder. Thus the liquid-filled GLIC-03 shows no advantage over the air-filled GLIC-03 in the build-up region except providing a higher signal. The close agreement, however, suggests that the method of applying dose rate-based recombination corrections to the liquid chamber response was appropriate.

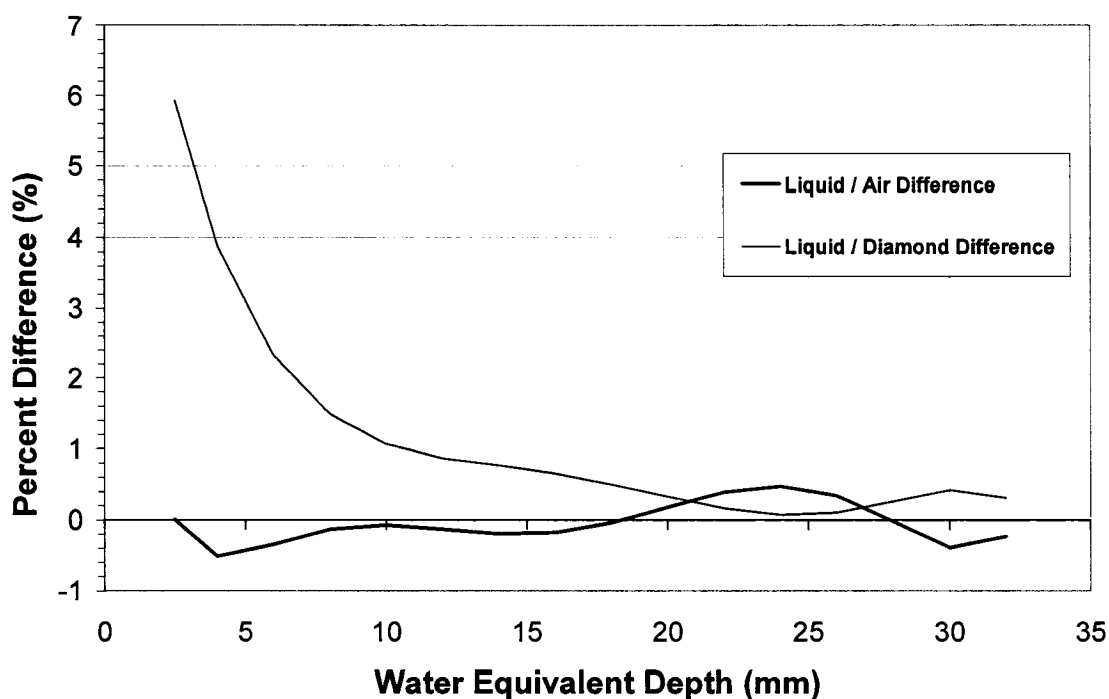


Figure 6-3. Comparison of linearly-interpolated PDI curve of the liquid-filled GLIC-03 with those of the diamond detector (lighter line) and the air-filled GLIC-03 (heavier line).

References

- ¹ Podgorsak, E. B., *Radiation Oncology Physics: A Handbook for Teachers and Students*. (International Atomic Energy Agency, Vienna, 2005).
- ² Khrunov, V. S., Martynov, S. S., Vatnitsky, S. M. *et al.*, "Diamond Detectors In Relative Dosimetry of Photon, Electron and Proton Radiation Fields," *Radiation Protection Dosimetry* **33** (1), 155-157 (1990).
- ³ Khrunov, V. S., Martynov, S. S., Vatnitsky, S. M. *et al.*, "Characteristics of Diamond Detectors of Ionizing Radiation," *Meditinskaya Tekhnika* **3**, 7-12 (1988).

Chapter 7

Conclusions and Future Work

7.1 Conclusions

The goal of this work was to investigate the properties of an ionization chamber that has the following possible advantages over traditional air ionization chambers: improving spatial resolution while not compromising the obtained signal; exhibiting a relatively flat energy response; and minimizing fluence perturbations. Such a chamber has the potential of improving radiation dosimetry, particularly in regions that lack charged particle equilibrium or in regions that exhibit high dose gradients.

Investigations of the chamber in this work, the GLIC-03, provided the following information: The GLIC-03 proved stable once a large pre-irradiation dose was given, as its response varied by less than 1% over ten hours. Measurements made with different fills of the chamber were also reproducible to within 1.5% of the mean. This allowed for further meaningful relative dosimetry experiments to be performed. Recombination is by far the leading disadvantage of liquid chambers, for which corrections must be applied. In this work, two methods of correcting for recombination were investigated: a theoretical model of general collection efficiency and a relative measurement of response as a function of dose rate. In both cases, high voltages and low dose rates aided in overcoming loss of ions due to recombination. The second method was chosen for application of recombination corrections to measurements made in a region with a lack of charged particle equilibrium: the build-up region of an 18 MV depth ionization curve. Measurements of this curve were compared to those made with a diamond detector, a solid-state detector which is also advantageous for its small-sensitive volume, its tissue equivalence, and its flat energy response. Comparisons between these detectors showed a 6% difference at the shallowest depths, which was likely due to dose rate effects of the diamond chamber. Also, the build-up curves of the liquid- and air-filled GLIC-03 were compared. The liquid chamber curve agreed within 0.5 - 1.0% of the air curve, indicating

an insignificant improvement in the liquid-filled chamber for measurements in the build-up region.

7.2 Future Work

Although the GLIC-03 stability and reproducibility were sufficient for relative experiments in determining the chamber's other properties, further work is needed in order to minimize or perhaps eliminate these issues. Because stability and reproducibility are affected by impurities that can be easily introduced into the chamber, a clean, sealed system would be ideal for a liquid chamber that does not diminish in stability over time. In this thesis, applying recombination corrections by comparing response as a function of dose rate was the simplest method. As the use of liquid chambers increases in the future, however, it will be necessary and more advantageous to apply absolute recombination corrections without outside reference. Thus more work needs to be placed in understanding and applying corrections by theory of collection efficiency in these dielectric liquids. For the present chamber, however, more work in this area also needs to be done. Also, further measurements in complex fields need to be performed, such as profile measurements of narrow fields or other regions that exhibit high dose gradient, in order to demonstrate the advantage of using liquid chambers. Experience may also lead to improvements in design and a cleaner, and more permanent and stable system.

Bibliography

- AAPM, TG-21, "A protocol for the determination of absorbed dose from high-energy photon and electron beams," *Med Phys* **10** (6), 741-771 (1983).
- Almond, P. R., Biggs, P. J., Coursey, B. M. *et al.*, "AAPM's TG-51 protocol for clinical reference dosimetry of high-energy photon and electron beams," *Med. Phys.* **26** (9), 1847-1870 (1999).
- Attix, F. H., *Introduction to radiological physics and radiation dosimetry*. (Wiley, New York, 1986).
- Bahar-Gogani, J., Wickman, G., Johansson, L. *et al.*, "Assessment of the relative dose distribution around an ¹⁹²Ir line source using a liquid ionization chamber," *Med. Phys.* **26** (9), 1932-1942 (1999).
- Bahar-Gogani, J., Grindborg, J. E., Johansson, B. E. *et al.*, "Long-term stability of liquid ionization chambers with regard to their qualification as local reference dosimeters for low dose-rate absorbed dose measurements in water," *Phys. Med. Biol.* **46** (3), 729-740 (2001).
- Berger, M.J., Coursey, J.S., Zucker, M.A. *et al.* (2005), *Stopping-Power and Range Tables for Electrons, Protons, and Helium Ions*, [Online] Available: <http://physics.nist.gov/Star> [May 1, 2006].
- Berger, M. J., Hubbell, J. H., Seltzer, S.M. *et al.* (2005), *XCOM: Photon Cross Sections Database*, [Online] Available: <http://physics.nist.gov/Xcom> [May 1, 2006].
- Berghöfer, T., Engler, J., Milke, J. M. *et al.*, "A Liquid Ionization Chamber As Monitor In Radiotherapy," Proceedings of the 9th Conference on Astroparticle, Particle, Space Physics, Detectors and Medical Physics Applications, Como, Italy, 2005 World Scientific.
- Boag, J. W., "Ionization Chambers" in *The Dosimetry of Ionizing Radiation*, Vol. II, edited by K. R. Kase, B. E. Bjärngard, and F. H. Attix (Academic Press, San Diego, 1987), pp. 169-233.
- Canada, National Cancer Institute of, "Canadian Cancer Statistics 2006," Toronto, 2006).
- Curry, T. S., Christensen, E. E., Murry, R. C. *et al.*, *Christensen's physics of diagnostic radiology*, 4th ed. (Lea & Febiger, Philadelphia, 1990).
- Dasu, A., Löfroth, P. O., and Wickman, G., "Liquid ionization chamber measurements of dose distributions in small 6 MV photon beams," *Phys. Med. Biol.* **43** (1), 21-36 (1998).

- Dempsey, J., Mutic, S., Low, D. *et al.*, "An Ideal Water-equivalent Cavity Theory Liquid Ionization Chamber," 2001 AAPM Annual Meeting, Salt Lake City, Utah, 2001 Med. Phys.
- Debye, P., "Reaction rates in ionic solutions," *Trans. Electrochem. Soc.* **82**, 265-272 (1942).
- Eberle, K., Engler, J., Hartmann, G. *et al.*, "First tests of a liquid ionization chamber to monitor intensity modulated radiation beams," *Phys. Med. Biol.* **48** (21), 3555-3564 (2003).
- Francescon, P., Cora, S., Cavedon, C. *et al.*, "Use of a new type of radiochromic film, a new parallel-plate micro-chamber, MOSFETs, and TLD 800 microcubes in the dosimetry of small beams," *Med. Phys.* **25** (4), 503-511 (1998).
- Franco, L., Gomez, F., Iglesias, A. *et al.*, "Liquid-filled ionization chamber temperature dependence," *Nuclear Instruments and Methods in Physics Research* **560** (2), 584-588 (2006).
- Gerbi, B. J. and Khan, F. M., "The polarity effect for commercially available plane-parallel ionization chambers," *Med. Phys.* **14** (2), 210-215 (1987).
- IAEA, "Absorbed Dose Determination in External Beam Radiotherapy : An International Code of Practice for Dosimetry Based on Standards of Absorbed Dose to Water," Report No. 398, International Atomic Energy Agency (Vienna, 2000).
- ICRU, "Radiation quantities and units," Report No. 33, International Commission on Radiation Units and Measurements (Bethesda, Maryland, 1980).
- ICRU, "Stopping powers for electrons and positrons," Report No. 37, International Commission on Radiation Units and Measurements (Bethesda, Md., U.S.A., 1984).
- ICRU, "Tissue substitutes in radiation dosimetry and measurement," Report No. 44, International Commission on Radiation Units and Measurements (Bethesda, Maryland, 1989).
- Johansson, B., Wickman, G., and Holmström, T., "Properties of liquid ionization chambers at LDR brachytherapy dose rates," *Phys. Med. Biol.* **40** (4), 575-587 (1995).
- Johansson, B. and Wickman, G., "General collection efficiency for liquid isooctane and tetramethylsilane used as sensitive media in a parallel-plate ionization chamber," *Phys. Med. Biol.* **42** (1), 133-145 (1997).

- Johansson, B., Wickman, G., and Bahar-Gogani, J., "General collection efficiency for liquid isooctane and tetramethylsilane in pulsed radiation," *Phys. Med. Biol.* **42** (10), 1929-1938 (1997).
- Johns, H. E. and Cunningham, J. R., *The Physics of Radiology*, 4th ed. (Thomas, Springfield, Ill., 1983).
- Kase, K. R., Bjärngard, B. E., and Attix, F. H., *The Dosimetry of ionizing radiation*. (Academic Press, San Diego, 1985).
- Khrunov, V. S., Martynov, S. S., Vatnitsky, S. M. *et al.*, "Characteristics of Diamond Detectors of Ionizing Radiation," *Meditinskaya Tekhnika* **3**, 7-12 (1988).
- Khrunov, V. S., Martynov, S. S., Vatnitsky, S. M. *et al.*, "Diamond Detectors In Relative Dosimetry of Photon, Electron and Proton Radiation Fields," *Radiation Protection Dosimetry* **33** (1), 155-157 (1990).
- Mattsson, O., Svensson, H., Wickman, G. *et al.*, "Absorbed dose in water. Comparison of several methods using a liquid ionization chamber," *Acta Oncologica* **29** (2), 235-240 (1990).
- Nahum, A. E., "Water/air mass stopping power ratios for megavoltage photon and electron beams," *Phys. Med. Biol.* **23** (1), 24-38 (1978).
- Pardo, J., Franco, L., Gomez, F. *et al.*, "Free ion yield observed in liquid isooctane irradiated by gamma rays. Comparison with the Onsager theory," *Phys. Med. Biol.* **49** (10), 1905-1914 (2004).
- Podgorsak, E. B., *Radiation Oncology Physics: A Handbook for Teachers and Students*. (International Atomic Energy Agency, Vienna, 2005).
- Podgorsak, E.B., *Radiation Physics for Medical Physicists*. (Springer-Verlag, Berlin Heidelberg, 2006).
- Rogers, D. W. and Ross, C. K., "The role of humidity and other correction factors in the AAPM TG-21 dosimetry protocol," *Med. Phys.* **15** (1), 40-48 (1988).
- Schmidt, W. F. and Allen, A. O., "Free-ion yields in sundry inadiated liquids," *J. Phys. C.; Solid State Phys.* **52**, 2345-2351 (1970).
- Schroeder, D. V., *An introduction to thermal physics*. (Addison Wesley, San Francisco, CA, 1999).
- Spencer, L. V. and Attix, F. H., "A theory of cavity ionization," *Radiat. Res.* **3** (3), 239-254 (1955).

- Stewart, K.J., *Accurate Radiation Dosimetry Using Liquid- or Air-filled Plane-parallel Ionization Chambers*, M.Sc. Thesis, (McGill University, Montreal, 2001).
- Thomson, J. J., "The Röntgen Rays," *Nature (London)* **53**, 391-392 (1896).
- Wickman, G., "A liquid ionization chamber with high spatial resolution," *Phys. Med. Biol.* **19** (1), 66-72 (1974).
- Wickman, G., "Liquid Ionization Chambers: On their design, physical properties and practical applications," Report No. 314, Umeå, Sweden, 1991).
- Wickman, G. and Holmström, T., "Polarity effect in plane-parallel ionization chambers using air or a dielectric liquid as ionization medium," *Med. Phys.* **19** (3), 637-640 (1992).
- Wickman, G. and Nyström, H., "The use of liquids in ionization chambers for high precision radiotherapy dosimetry," *Phys. Med. Biol.* **37** (9), 1789-1812 (1992).
- Wickman, G., Johansson, B., Bahar-Gogani, J. *et al.*, "Liquid ionization chambers for absorbed dose measurements in water at low dose rates and intermediate photon energies," *Med. Phys.* **25** (6), 900-907 (1998).
- Wolfson, R. and Pasachoff, J. M., *Physics for scientists and engineers*, 3rd ed. (Addison-Wesley, Reading, Mass., 1999).